UNIQUE TWO-WAY FIELD PROBE CONCEPT UTILIZING A GEODESIC SPHERE AND QUAD-ROTOR

THESIS
MARCH 2015

Travis A. Albee, Captain, USAF

AFIT-ENG-MS-15-M-007

**DEPARTMENT OF THE AIR FORCE
AIR UNIVERSITY**

AIR FORCE INSTITUTE OF TECHNOLOGY

Wright-Patterson Air Force Base, Ohio

AFIT-ENG-MS-15-M-007

UNIQUE TWO-WAY FIELD PROBE CONCEPT UTILIZING A GEODESIC SPHERE
AND QUAD-ROTOR

THESIS

Presented to the Faculty

Department of Electrical and Computer Engineering

Graduate School of Engineering and Management

Air Force Institute of Technology

Air University

Air Education and Training Command

In Partial Fulfillment of the Requirements for the

Degree of Master of Science in Electrical and Computer Engineering

Travis A. Albee, B.S.E.E

Captain, USAF

March 2015

DISTRIBUTION STATEMENT A.
APPROVED FOR PUBLIC RELEASE; DISTRIBUTION UNLIMITED.

AFIT-ENG-MS-15-M-007

UNIQUE TWO-WAY FIELD PROBE CONCEPT UTILIZING A GEODESIC SPHERE
AND QUAD-ROTOR

THESIS

Travis A. Albee, B.S.E.E
Captain, USAF

Committee Membership:

Dr. Peter J. Collins
Chair

Dr. Richard G. Cobb
Member

Maj Brian G. Woolley, PhD
Member

AFIT-ENG-MS-15-M-007

Abstract

Surveying the test volume of a radar range normally involves utilizing antenna field probes, which measure the electromagnetic EM field in that volume of space. Today, field probes vary in size and shape and can be difficult and time consuming to setup. They also have a limited range of motion due to their support structure and translational mechanism, which also has scattering mechanisms that can perturb the field they are measuring. Field probes are useful, but because of these issues they can provide limited characterization of the field illuminating the measurement area. Leveraging quad-rotor technology, coupled with a two-way probe concept, will provide the flexibility and maneuverability to easily transverse the test volume without the interfering supporting structures or translational mechanisms. The two-way probe concept characterizes the illuminated field indirectly, by utilizing a geodesic sphere to encompass a quad-rotor and shield its many scatterers, which in-turn provides a much simpler scattering mechanism whose scattering statistics can provide an accurate measure of the illuminated field at the position of the quad-rotor. This new two-way flying field probe concept will provide valuable magnitude and phase information to the radar engineer.

Acknowledgments

I would like to express my sincere appreciation to my faculty advisor, Dr. Peter Collins, for his tremendous patience, guidance and support throughout the course of this thesis effort. The insight and experience was certainly appreciated. I would, also, like to thank my sponsor, Dr. Tim Conn, from the National Radar Test Facility for both the support he provided in this effort and giving me the opportunity to participate in this unique endeavor. I would also like to express my sincere gratitude to Mr. Scott Goodman and his team at the Advanced Compact Range for the invaluable support they provided. And finally, I would like to thank my wife and kids for putting up with the weird hours and my daily despair.

Travis A. Albee

Table of Contents

List of Figures

List of Tables

UNIQUE TWO-WAY FIELD PROBE CONCEPT UTILIZING A

GEODESIC SPHERE AND QUAD-ROTOR

I. Introduction

1.1 General Issue

The test volume is a volume of space encompassing the object being measured. When an electromagnetic field is illuminating the test volume, the magnitude and phase of this volume is unknown. Antenna field probes are tools used by radar engineers to survey the EM field traversing through the test volume and illuminating the test item being measured. Existing probes have limitations in physical size, motion, and scattering phenomenology due to their support structures and translational mechanisms, which in- turn perturb the measured field in the test volume preventing an accurate characterization of the illuminated field.

1.2 Problem Statement

Antenna field probes are used by engineers to measure the near field and far field of an EM source [1]. Specifically, radar engineers use field probes to survey the characteristic behavior of an electromagnetic field in a volume of space surrounding an object of interest. This volume of space is known as the test volume and is located in the far field region.

Accurate measurements of an EM fields can be difficult with standard field probes, errors can occur from orienting the field probe incorrectly with respect to the field vector of the EM wave [1]. Some other possible sources of errors in standard probes can arise from cable connections, measurement distance, and sensor size [1]. Figure 1 is a picture of a field probe used in an indoor compact range [2]. It is approximately 133 inches in length and 20 inches in width. It weighs approximately 33 lbs [2]. The DJI Phantom II weighs approximately 2.2 lbs

and has a maximum diagonal length of 1.1 ft [3]. The geodesic sphere built for this thesis weighs approximately 2 oz and its diameter is 19 inches. The 4608-1S field probe is stationary and limited in motion by its translational mechanisms. The two-way field probe concept will have the potential to traverse to any position in the test volume.
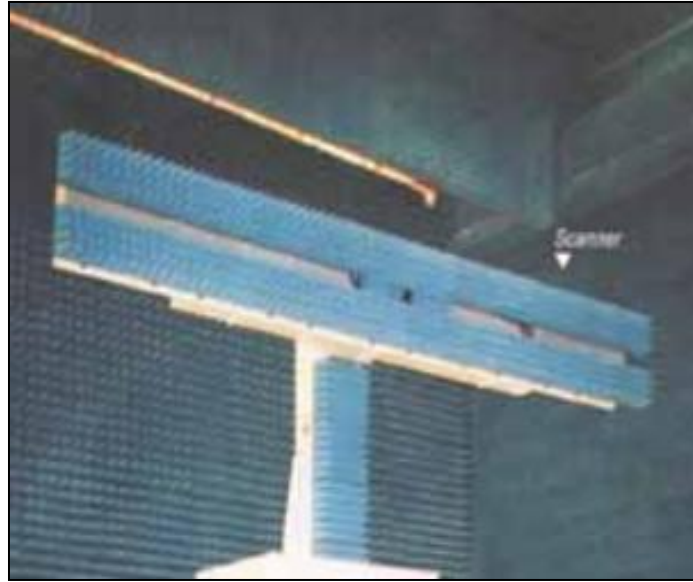
Figure 1: AL4608-1S Special High Accuracy Field Probe

Field probes are useful tools, but utilizing standard probes means having to work within the confines of their limitations. Some standard probes are structurally robust making them cumbersome and time-consuming to setup. Another factor is there mobility, their ability to transverse and measure the entire test volume is limited by their translational mechanisms. Field probes used for radar range measurements are generally fixed in position and their range of motion is further limited by their translational mechanisms. Finally, their structure and translational mechanisms can cause unwanted perturbations in the electromagnetic field, possibly

2

leading to erroneous measurements and to improper understanding of the EM field passing through the test volume.

Characterizing the behavior of an EM field occurring in the test volume will give a radar engineer a more thorough understanding of the objects they are measuring, which is especially true for outdoor radar ranges, such as the National Radar Test Facility NRTF, that have to contend with a number of environmental factors such as wind, temperature, rain, humidity, animals, and insects affecting the EM field illuminating their test volume.

Since today's antenna probes possess the limitations previously discussed, this thesis will investigate the development of a unique two-way field probe concept. As previously mentioned, existing field probes have inherent limitations with their size, geometric design, and mobility. The two-way antenna probe will be designed using quad-rotor technology and a shielding geodesic scattering geometry. First, typically quad-rotors are small so their EM back scatter will be minimal. However, without a shielding structure of some kind encompassing it, when bombarded with an EM wave the quad-rotor's structural geometry will have a position and angle dependent radar cross section RCS that will make it difficult to properly characterize the behavior of the EM field occurring inside the test volume. Second, because the quad-rotor's structural geometry is a cause for concern, a geodesic cage, in the shape of a sphere, will be built to encompass the quad-rotor. This cage will behave like a faraday cage of sorts, shielding the quad-rotor's RCS phenomenology from the radar's antenna receiver. Finally, the mobility and speed of a quad-rotor will allow it to easily transverse a volume of space, giving it the flexibility and maneuverability to navigate to any location inside the test volume and measure the EM wave.

1.3 Research Focus

The primary goal of this research will be the development of the geodesic cage that will encompass the quad-rotor along with an analysis of its scattering statistics as function of the quad-rotor's position and pose. There are two aspects of geodesic design that are important to this thesis. First, since the scattering and shielding properties of the geodesic cage as a function of frequency, pose, and polarization are unknown, it is necessary to determine the best RCS prediction tool for use in the RCS characterization of the geodesic sphere. The validation of code as a design tool requires comparison with RCS measurements or predictions of a known uncertainty. RCS experimental measurements can either be taken from actual measurements on an indoor or outdoor radar range. The Air Force Institute of Technology AFIT provides a variety of computer based tools for predictive measurements and each of these tools will be evaluated to determine which tool is most efficient.

A critical component of the overall probe concept is an understanding of how uncertainties in the quad-rotor's position and pose translate to an uncertainty in the measured field. Therefore, the second goal of this thesis is to analyze the positional uncertainties associated with the differential global positioning system DGPS system and inertial measurement unit IMU utilized by the quad-rotor in order to determine in a statistical sense, how the probe's position and pose uncertainties impact the measured probe RCS magnitude and phase uncertainties which in turn determine the probed field uncertainties.

1.4 Investigative Questions

The research focus of this thesis presupposes three questions:

1. Is there a commercially available tool that can sufficiently predict the RCS of the geodesic sphere?

2. Can the geodesic sphere shield the RCS mechanisms of the quad-rotor?

3. How will positional and axial uncertainties caused by the DGPS system and quad-rotor IMU affect the RCS magnitude and phase measurements taken by the radar?

1.5 Methodology

To answer these questions, this thesis will first investigate the RCS phenomenology of a geodesic sphere. It will look at structural design and use varying computer based tools to develop predictive models of the RCS characterization of the geodesic sphere. This thesis will also leverage resources, such as the Air Force Research Laboratory's Advanced Compact Range ACR, to provide experimental measurements of the structural design to assess if the geodesic sphere is a sufficient barrier to shield the inner object as well as determine the sphere's RCS as a function of frequency, polarization, and pose to use in developing the probe uncertainty analysis.

The final question will involve the investigation of positional truth. There are two aspects of positional truth that will need to be investigated: the actual physical position and the axial position. Physical position involves looking at the position of an object in the XYZ-coordinate system. A quad-rotor, specifically ones used outside, utilizes different tools to measure its exact position. One of these tools is the DGPS. However, there are uncertainties or margins of error associated with DGPS position. Axial position will involve investigating roll, pitch, and yaw RPY uncertainties, which are associated with the quad-rotor itself. In both cases, the question will be to look at how these uncertainties affect RCS measurements. As the quad-

rotor transverses the test volume, what are the magnitude and phase errors associated with these uncertainties?

1.6 Assumptions

For this research, the following assumptions were made to limit the scope of the project:

- An outdoor radar range is not available at Wright Patterson AFB. However, there are two indoor radar ranges where measurements can be taken. An indoor range will suffice to provide effective data that can be related to an outdoor range

- This thesis will not integrate a geodesic sphere with a quad-rotor. However, for theoretical and real world measurements, canonical objects (such as a flat plate and dihedral) will be mounted in the center of the sphere in place of a quad-rotor. The canonical objects will provide effective data for analyzing object/sphere scattering interactions

- The AFIT Advanced Compact Electromagnetic Range ACER was inoperable due to maintenance issues during the duration of this research and the ACR was a limited use (one time only) resource. However, the measured data from the ACR and theoretical measurements acquired during the duration of this thesis will be sufficient to accomplish the research objectives

1.7 Implications

The two-way field probe concept will potentially provide a radar engineer a more thorough understanding of the magnitude and phase behavior of the EM wave illuminating the test volume. The two-way probe concept is centered on utilizing a geodesic sphere, where its

own scattering phenomenology will provide the necessary magnitude and phase information for understanding the behavior of the illuminated test volume; thus, orientation of geodesic sphere to the EM field vector will not matter. For some standard field probes, orientation of probe is important to avoiding erroneous measurements [1]. Integrating the sphere with a quad-rotor will provide the mobility and range of motion necessary to traverse to any location within the test volume, which is not normally provided for by standard field probes; therefore, potentially any location within the test volume can be measured. Finally, when compared to standard field probes quad-rotors are considerably more lightweight so setup and disassemble will potentially be easier.

1.8 Preview

In this thesis, *Chapter II* provides the background and theory needed to understand the concepts in this research. *Chapter III* will be focused on RCS characterization of the geodesic sphere through simulation and real measurements. Furthermore, it will encompass the mathematical modeling involved to undertake the various uncertainty analysis's associated with the DGPS and quad-rotor systems. *Chapter IV* details the results and provides an analysis from the testing conducted in *Chapter III*. Lastly, *Chapter V* gives a summary of the research, provides conclusions on the thesis and offers opportunities for future work to expand this effort. This chapter describes the problem to be addressed by this research, the goals of this project and previous related efforts. Additionally, the assumptions used in this research on the system and its data are examined in order to limit the scope of the problem. Lastly, an outline for the organization of this thesis is given.

II. Literature Review

2.1 Chapter Overview

The two-way probe concept, as described in chapter one, will provide magnitude and phase information of the EM wave illuminating the test volume. In order to accomplish this goal, a wide range of concepts have to be brought together and understood. This chapter will provide the necessary understanding of the concepts involved in this research.

First, this thesis is centered on RCS measurements; therefore, a basic understanding of how radar works and what the properties of a uniform plane wave are is necessary to facilitate a conceptual grasp of RCS. Second, the two-way probe will be built from a geodesic sphere design; therefore, a brief description of geodesic spheres will be given. Third, the geodesic sphere will be illuminated by an EM plane wave. Its characteristic RCS magnitude and phase will be a function of the sphere's position and pose within the EM wave. A quad-rotor's differential global positioning system DGPS collects and relays positional data to the observer. And the onboard inertial measurement unit IMU controls axial movements of the quad-rotor. Axial movements control the orientation or pose of the sphere with respect to the radar. A brief description of both DGPS and IMU components will be given. Both the DGPS and IMU have associated levels of uncertainties, which could affect the accuracy of any RCS measurements that are made. Therefore, a description of the uncertainties associated with each component will be included in this chapter. Finally, modeling and prediction analysis of the geodesic sphere will be conducted; however, in order to accomplish this goal a determination of the best computer modeling and prediction tools will have to be done. A brief description of each of these tools will be given.

2.2 Basic RADAR System Model

Radio detection and ranging, RADAR, is an electrical system that transmits EM wave towards an area of interest [2]. The radar is able to detect objects when the propagated EM waves come in contact with an object, then the EM wave incident on the object is scattered or reflected. Those scattered EM waves are received by the radar's receiver telling it that an object is present. Although radars may have varying subsystem components, all have the major components: transmitter, antenna, receiver, and signal processor [2]. The basic radar system description is illustrated in Figure 2.
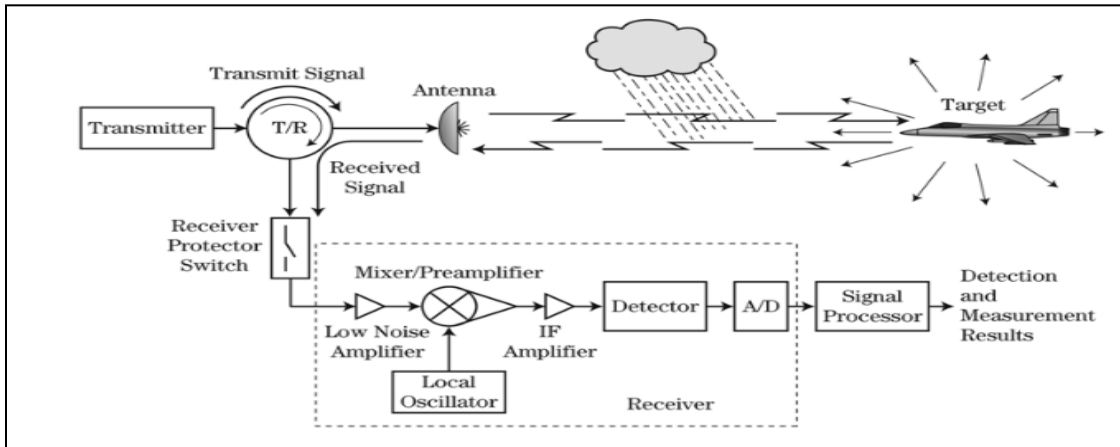
Figure 2: Basic Radar System Model

The Radar Range Equation RRE,

$$R_{max} = \sqrt[4]{\frac{P_t G^2 \lambda^2 \sigma}{(4\pi)^3 P_{min}}} \tag{1}$$

is a mathematical description of how radar detects objects of interest. For the purposes of this thesis, transmitted power, P_t, the wavelength, λ, and the RCS, σ, are components of the RRE that are also related to the power density equation, Equation 3, and the RCS equation, Equation 4.

The strength of the EM wave transmitted from the radar is controlled by the power utilized to transmit that EM wave. According to the RRE, equation 1, the higher the transmitted power, P_t, the greater the return signal from the object being detected; therefore, increasing the radar's transmitted power increases its ability to detect.

Wavelength is a function of frequency and the speed of light (3 x 10^8 m/s). The smaller the frequency becomes the longer the wavelengths of the EM wave. A higher transmitted frequency will equate to shorter wavelengths. For instance, a 2 GHz frequency has a wavelength of 0.15 meters (λ = c/f = 3 x 10^8 m/s/2 x 10^9 s); whereas, a 10 GHz transmitted frequency will have a wavelength of 0.03 meters. The significance of longer wavelengths is that the transmitted EM wave gives the radar more time to detect finer or smaller objects of interest. Shorter wavelengths give the radar less time to detect objects of interest that are geometrically small [2]. In regards to the RRE, wavelength is directly related to the radar's ability to detect an object of interest; therefore, a larger wavelength will aid in enhanced detection.

According to the RRE, the magnitude of an object's RCS, σ, is also directly related to the radar's ability to detect an object of interest. Simply stated, the larger the RCS of an object the greater the probability of detecting that object.

Theoretically, the two-way field probe will possess the ability to translate to any position within the test volume. The radar's ability to detect scattered EM waves emanating from the two-way field probe at any position within the test volume will be dependent on the three components from the RRE discussed previously (transmitted power, wavelength, and RCS). The relationship between the RRE and RCS will be developed further in a later section of this thesis.

The final variable in the RRE is the minimum detectable signal loss, P_{min}. This variable encompasses multiple components, such as losses related to system noises such as temperature,

receiver noise, the signal to noise ratio SNR, and various other losses due to either the system transmitting the EM wave or the environment in which the EM wave is transmitted. However, for the purposes of this thesis an idealized RRE is presented in which losses to the system are ignored [2].

2.3 Basic Outdoor RADAR Range Model

The traditional purpose of radar is to search, detect, and track an object [2]. However, outdoor and indoor radar ranges use radar to investigate the scattering phenomena associated with an object of interest. For this research, all RCS measurements were taken at the ACR, an indoor radar range, located at Wright Patterson AFB, OH.

The RCS measurements performed as part of this thesis were for the purpose of determining the sphere's RCS as a function of frequency, polarization, and pose. A key assumption of this thesis is that the uncertainty of the measurements is negligible in determining the uncertainty of the probe measurements through Monte Carlo simulation. The uncertainty analysis conducted in this research is modeled after the NRTF's outdoor radar range. The basic physical model of the NRTF is illustrated in Figure 3. Figure 3 serves two purposes; first, it illustrates the basic relationship between the object of interest and the radar. Second, all calculations involved in the solving of angular measurements is based on the distance between the NRTF's radar and target pylon. This distance is approximately 8500ft or 2590m [3]. The second image in the figure illustrates a volume of space called the test volume. The test volume is a volume of space (LxWxH = 100x100x40ft) surrounding the object under test where the illumination is assumed to be approximately planar. This volume of space will be the focus of this research's uncertainty analysis.
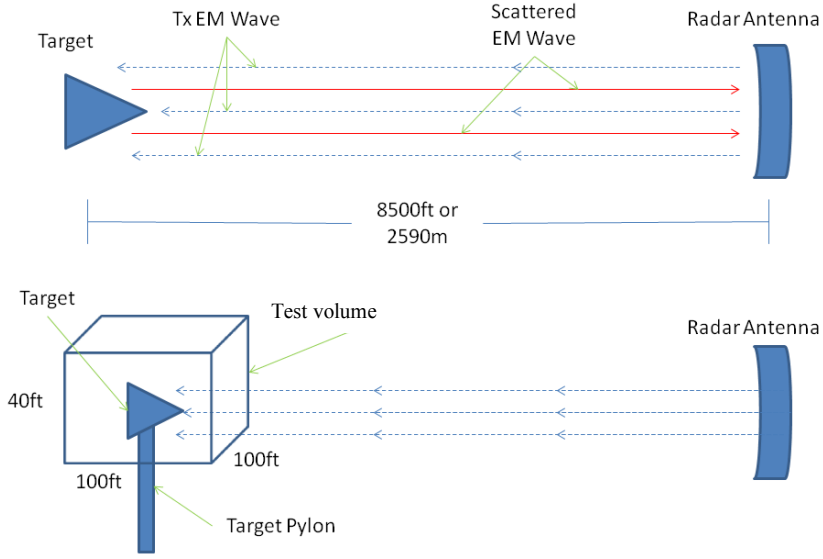
Figure 3: Basic NRTF Range Model

2.4 Radar Cross Section

It is stated in chapter one that this thesis is centered on measuring the RCS of a geodesic sphere. The RCS of the geodesic sphere will provide magnitude and phase phenomenology over the sphere's geometric structure, which will provide more insight into the behavior of the illuminated test volume. This section will briefly discuss various concepts related to RCS measurements.

RCS is defined as

$$\sigma = \lim_{r\to\infty} 4\pi r^2 \frac{|E^{scat}|^2}{|E^{inc}|^2}, \qquad (2)$$

where RCS is represented by the symbol sigma, σ, and it is the measure of the strength of reflective energy from an object [3]. In fact, its field strength is 4π times the ratio of the

12

scattered electric field over the incident electric field as the limit of 'r', distance from the scatterer to the radar antenna receiver location, approaches infinity [2]. Since RCS is a measure of reflected field strength, it can also be defined in terms of power and subsequently a definition of RCS can be derived from the following power density equation [3],

$$P_s = \frac{\sigma P_i}{4\pi R^2}.$$

(3)

Equation 3 indicates that power, P_s, falls off as $1/R^2$, which means that the further an object is from the transmitting radar antenna the less power is received at the receiving antenna. In a previous section it is eluded that a relationship exists between the RRE, Equation 1, and RCS. Comparing equations 1 and 3 illustrates that $P_i \propto P_t$, where P_i is the power incident on an object and P_t is the power transmitted from the radar. Equation 3 further indicates that the power of the scattered EM wave, P_s, is directly related to strength of the power incident on the object, which means that the stronger the transmitted power from the radar, the stronger the scattered power returning to the radar; therefore, a stronger detection and RCS is likely. Thus, rearranging the power density equation, Equation 3, gives the following definition of RCS in terms power,

$$\sigma = 4\pi R^2 \frac{P_s}{P_i}.$$

(4)

Comparing Equations 2 and 4 illustrates that $E_s{}^2 \propto P_s$ and that a direct relationship exists between the electric field strength and power [3]. Looking at just Equation 2, and concerning

13

oneself with just the scattered electric field, $E_s{}^2$, it can be seen that the square root of the RCS is also proportional to the scattered electric field where

$$|\sqrt{\sigma}| \propto |E_s|. \tag{5}$$

The relationship developed in Equation 5 will be important in the subsequent chapters when the discussion of the effects of positional uncertainty on RCS come into question.

As previously discussed, when an electromagnetic wave becomes incident on an object it will scatter in multiple directions, some of those scattered waves will return to the radar's antenna receiver. The returning energy is an EM field unique to the object that is illuminated. To visualize this process, consider the 6.5in x 4.75in metal flat plate in Figure 4.   The flat plate is modeled in Computer Simulation Technology Microwave Studio CST, where the RCS of the flat plate is simulated and calculated. The flat plate is modeled to be a perfect electric conductor PEC; meaning, it will easily reflect EM energy.
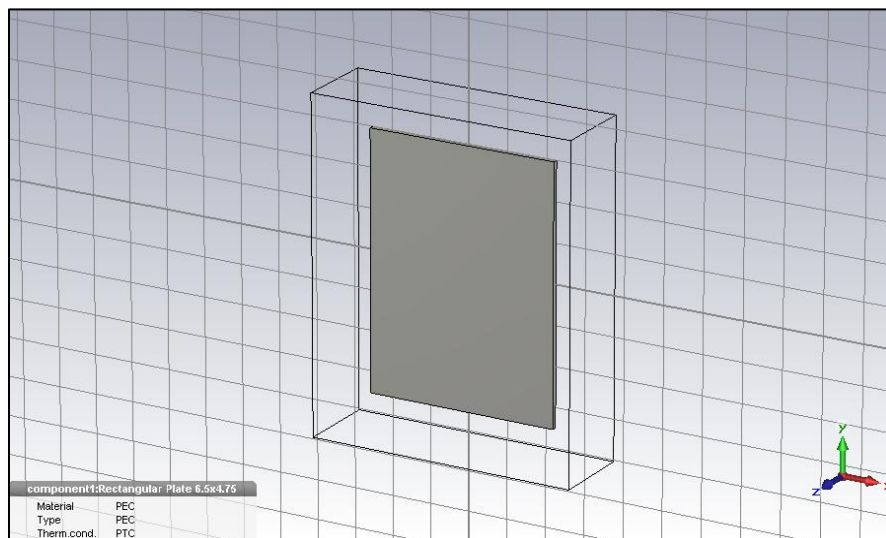
Figure 4: Flat Plate 6.5in x 4.75in

14

An example of RCS is illustrated in Figure 5. Figure 5 is a three dimensional plot which shows the scattering behavior of an EM wave as it becomes incident on the flat plate depicted in Figure 4. A resulting scattered field is created, which can be seen in Figure 5. It displays the lobing behavior of the scattered EM field. The main lobes occur at 0° and 180°. At these positions the RCS magnitude of the main lobe is measured to be 3.76 dBsm. The side lobes, the areas of smallest RCS magnitudes, which are located in the regions at 90° and 270°, are calculated to be -13.4 dBsm. It is evident that the main lobe RCS is quite a bit larger than the side lobe RCS and this is due to the main lobe reflections bouncing off of the largest areas of the flat plate and the side lobes are bouncing off the smallest areas of the flat plate, mainly the thin edges. Thus, the scattered EM field from the flat plate is the radar cross section [4]. And it can be inferred that the size of the surface area reflecting the EM wave directly relates to the magnitude of the object's RCS.
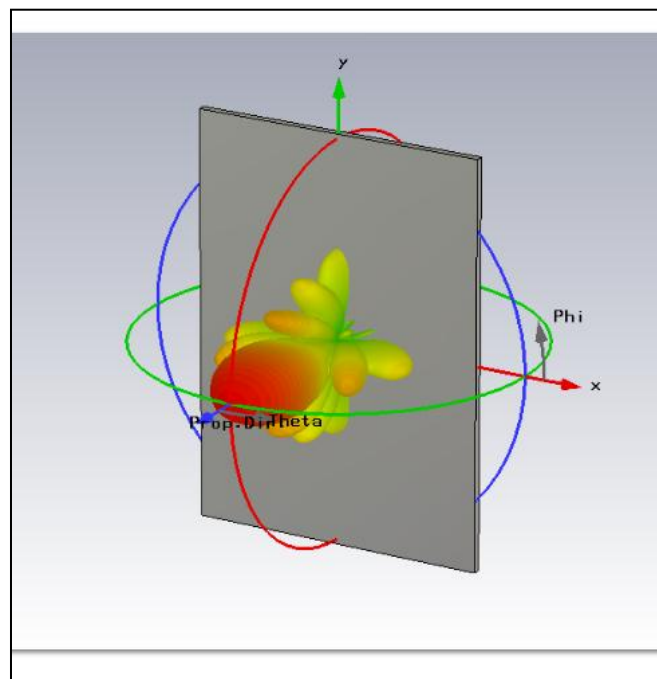
Figure 5: Bistatic Plot - Flat Plate 6.5in x 4.75in, 6GHz

2.5 Uniform Plane Waves

The definition of a uniform plane wave is when the electric field, magnetic field, and the direction of propagation are all mutually orthogonal to each other [4]. Figure 6 illustrates the orthogonal nature of the uniform plane wave [5]. Typically, EM waves propagate in a spherical manner. At a far enough distance the wave front of the spherically transmitted wave becomes large enough to be considered planar over the object's dimensions. Furthermore, the phase change of the EM wave is insignificant due to the curvature of the spherically transmitted wave being so small at large enough distances [2, p. 213].
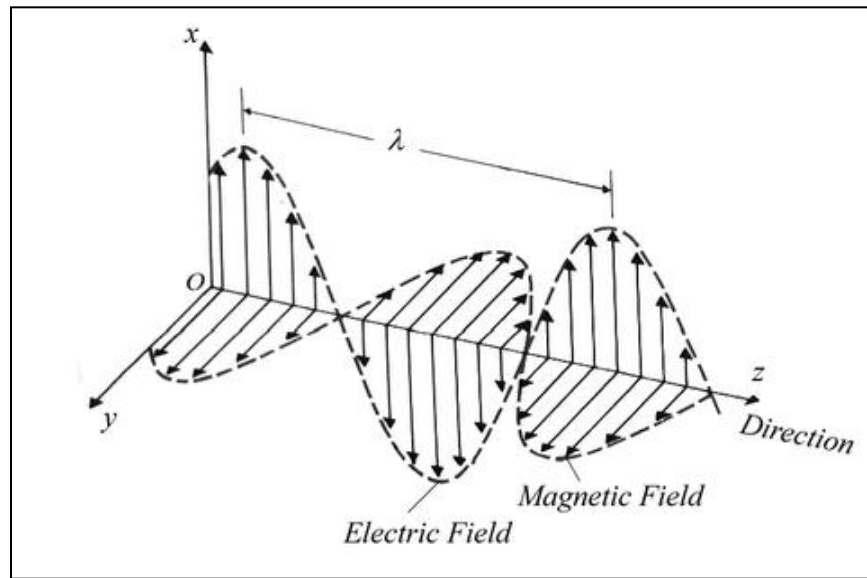
Figure 6: Uniform Plane Wave [5]

As previously discussed, Equation 2 is the mathematical definition of RCS, which relates the RCS to the scattered and incident electric fields. However, a uniform plane wave, as depicted in Figure 6, also has a magnetic field component. Equation 4 though, states that RCS is

ratio scattered power and incident power, thus "the power of an EM wave is proportional to the square of its electric or magnetic field magnitudes, so RCS can be expressed as

$$\sigma = \lim_{r \to \infty} 4\pi r^2 \frac{|E^{scat}|^2}{|E^{inc}|^2} = \lim_{r \to \infty} 4\pi r^2 \frac{|H^{scat}|^2}{|H^{inc}|^2},$$ (6)

because the electric field and magnetic field are both in the far field and related to each other by the impedance of free space." [2, p. 220]. Therefore, for the purposes of this thesis, only the electric field, E, of the uniform plane wave is of interest. The magnetic field can be ignored.

Equation 7 is a mathematical representation of the electric field of a uniform plane wave with unit amplitude and direction of propagation [6],

$$E(r) = \hat{e}e^{-jk\hat{s}\cdot r}$$ (7)

The 'r' variable is the position vector [6],

$$r = x\hat{x} + y\hat{y} + z\hat{z}.$$ (8)

The polarization vector is $\hat{e}$ [6] and can be seen expressed in Equation 9 as

$$\hat{e} = \hat{x}\cos\theta_i\sin\varphi_i + \hat{y}\cos\theta_i\sin\varphi_i - \hat{z}\sin\theta_i.$$ (9)

And $\hat{s}$ is a unit vector pointing towards the origin [6], and seen expressed in Equation 10 as

$$\hat{s} = -(\hat{x}\sin\theta_i\cos\varphi_i + \hat{y}\sin\theta_i\sin\varphi_i + \hat{z}\cos\theta_i)$$ (10)

An alternate form of Equation 7 for the electric field [2] can be written as

$$E = E_o \cos(kr + \omega t - \varphi) \tag{11}$$

$E_o =$ Electric Field Amplitude
$k = wave\ number = 2\pi/\lambda$
$\omega = angular\ frequency = 2\pi f$
$\varphi = phase$
$t = time\ is\ secs$
$r = direction\ of\ propagation$

In regards to this thesis, Equation 11 will be used to calculate the magnitude of the electric field of a point scatterer in the test volume. The relationship developed in Equation 5 will then provide the RCS of the point scatterer as a function of position. The point scatterer will be the ideal model used to provide a pseudo set of measured data points that will be used as part of an uncertainty analysis conducted later on in this thesis.

2.6 Relevant Research

The two-way probe concept is not new; however, the use of a geodesic sphere as a two-way probe is. Traditionally, and instead of using a geodesic sphere, radar ranges will use a known scatterer such as a sphere, plate, or trihedral [5]. To contrast, a one-way probe will use a receiving antenna to scan the quiet zone where the EM field's amplitude and phase incident on the probe is analogous to the field incident on a test item at that point. Two-way probes, utilizing their backscatter to relay information about the incident EM field, will display twice the amplitude and phase of a one-way probe [5]. In the case of both probes, the pattern of the reflected field will modify the EM field and provide a structure to the field within the test volume that can be analyzed [5].

The geodesic sphere will be used in the same manner as traditional two-way probes. Since the geodesic sphere is not a known scatterer the focus of this thesis will be to statistically characterize its RCS phenomenology. It is made unique by its potential to translate to any position in the test volume. In order to realize the two-probe concept, research into various disciplines will be necessary to successfully realize the goals of this research.

2.6.1 Geodesic Sphere

One of the primary focuses of this thesis is the development of a geodesic sphere which will encompass the quad-rotor. In regards to the two-way field probe concept, a key design parameter is centered on discovering a scattering geometry that would shield the scattering mechanisms of the quad-rotor from the radar. Furthermore, this scattering geometry needed to be an angle and polarization independent scatterer to the measurement radar allowing the direct measurement of the illuminated field.

2.6.2 Geodesic Dome/Sphere Construction

Construction of a geodesic sphere required that four main questions be answered:

1. Will the material used be light enough not to weigh down a quad-rotor?

2. Will the sphere's structure restrict air lift, thereby preventing the quad-rotor from flying?

3. Will the geodesic sphere be difficult to build?

4. Reflectivity, will the material used to construct the sphere reflect incoming EM waves?

A geodesic sphere can be constructed with a wide variety of materials, making it as light as one wants and as reflective, and the sphere could be built to any diameter. The diameter of the sphere determines the length of each strut comprising the sphere [7].

Geodesic spheres are classified by frequency. The frequency refers to the amount of inner struts needed to construct the sphere [8]. Figure 7 is an illustration of a 2v geodesic dome [7]. The 2v geodesic dome is made up of pentagons joined together at their vertices.
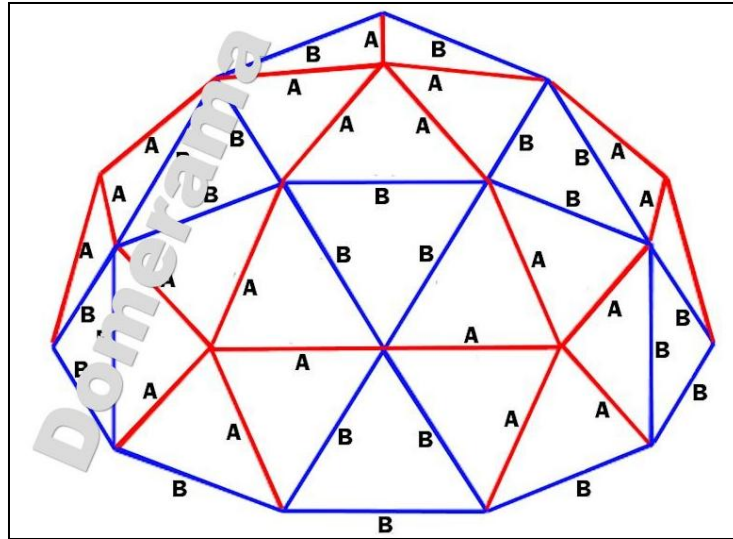
Figure 7: 2v Geodesic Dome [7]

Figure 8 is an illustration of the frequency classifications of geodesic spheres [9]. It can be seen that the higher frequency equates to a greater number of struts or triangles. Each increase in frequency leads to another truncation of the sphere; thus, higher frequency structures translate into a smoother, rounder sphere. It also results in a stronger structure capable of supporting greater weight [7], which would possibly allow the geodesic sphere to support heavier weight and it could act as a protective structure for the quad-rotor should it crash during flight.
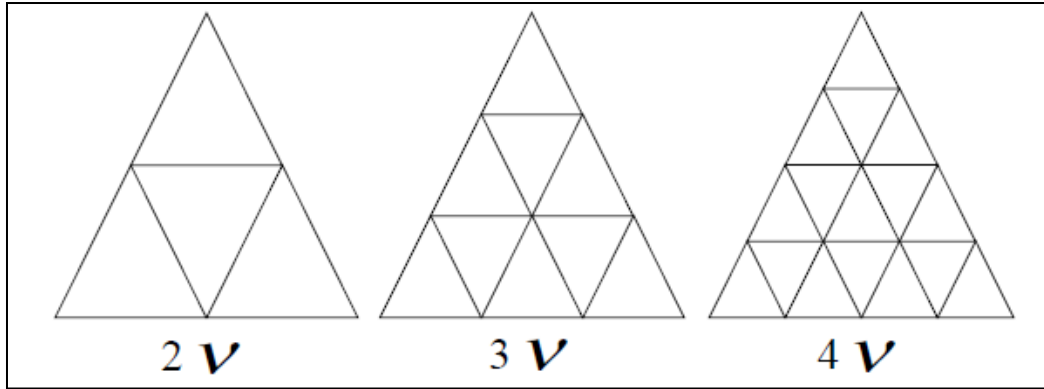
Figure 8: Frequency Classification for Geodesic Domes [9]

For this thesis, a 2v and a 3v sphere were constructed; however, only the 2v sphere was used for RCS measurements. Figure 9 is a picture of the sphere that was constructed for this thesis by Dr. Peter Collins. The physical dimensions of the strut lengths and number struts were determined using an online geodesic dome calculator [7]. The struts were constructed from stir straws. The joints were designed in FreeCAD and fabricated in a 3D printer. The struts and joints were glued together to form the geodesic sphere. The sphere was then painted with conductive copper paint making it reflective.

Figure 9: 2v Geodesic Sphere

To construct a geodesic dome/sphere is relatively simple. There are a number of online websites that provide sufficient aid in the task. However, the best website to use is Domerama. It not only provides an abundance of literature on geodesic structures, it also provides the variety of tools to aid in the construction of them. One such tool is a geodesic calculator. Figure 10 shows the geodesic calculator where the dimensions of a desired sphere are entered. Figure 11 shows the calculated strut lengths, angles, and quantity of struts needed to build the sphere based on the dimensions entered. To make things easier, the website provides a blueprint, Figure 7, of how to construct a desired geodesic dome. To build a complete sphere, it is only necessary to double the amount struts needed, build two domes, and then connect them. Table 10 list all the structural requirements that were needed to build a 2v geodesic sphere, Figure 9.

	Clear Values	
Spherical radius	9.500	Calculate
Spherical diameter	19.000	Calculate
Height	9.500	Calculate
Floor area	265.238	Calculate
Perimeter	59.690	Calculate

Figure 10: Domerama's Online Calculator, Dimension Inputs

Figure 11: Domerama's Online Calculator, Calculated Strut Lengths & Angles

Table 1: 2v Geodesic Sphere Dimensions

Sphere Diameter	19in
Strut A Length	5.192in
Strut B Length	5.871in
Strut A Angle	15.86˚
Strut B Angle	18˚
# of Strut A	30
# of Strut B	35
Stir Straw Diameter	0.157in

2.6.3 Differential GPS and XYZ Frame of Reference

Another major goal of this research is to determine the degree of which positional uncertainties affect the RCS magnitude and phase measurement. Once the quad-rotor and geodesic sphere are integrated and operational, the DGPS system will provide positional truth to the accuracy of the RCS measurement.

23

DGPS measures the position of an object in the XYZ-coordinate system. For the purposes of the thesis it is important to provide a frame of reference. Figure 12 indicates that the XY coordinates are related to the horizontal positional directions of left (-X) and right (+X) and forward (+Y) and backward (-Y). Finally, the Z coordinate corresponds to up (+Z) and down (-Z).
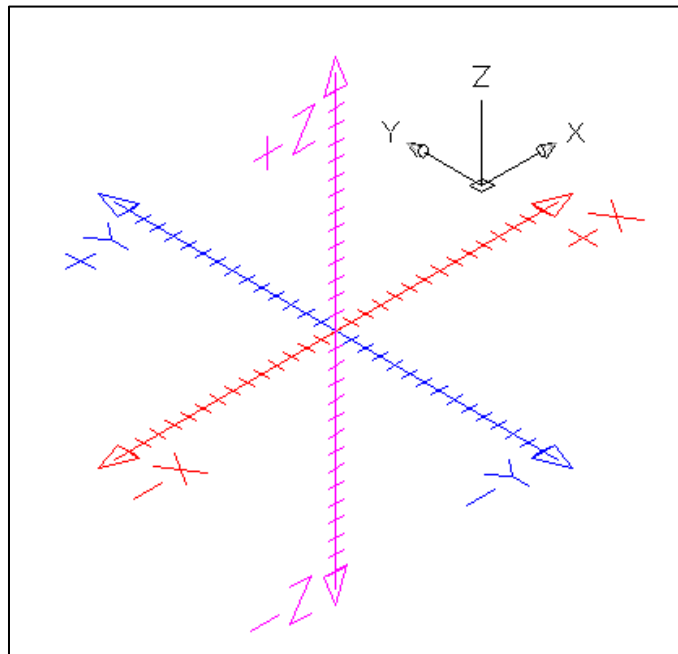
Figure 12: Spatial Reference Frame XYZ Coordinate System

Standard GPS has a positional accuracy to be within 3 to 15 meters along the horizontal planes of the Earth [11]. DGPS is an enhancement to standard GPS. It improves accuracy by using a reference receiver with a known point. It then compares this known point to the reported errors between multiple satellites real-time and each satellite then adjusts its error. These error corrections can then be communicated to other satellites to correct their measurements real-time [12]. DGPS can be configured in multiple ways to improve its accuracies. Table 2 shows the

level of accuracies of each of these configurations [11]. For the purposes of this thesis the standard DGPS accuracy of 5m will be used since it represents the worst case scenario.

Table 2: DGPS Accuracies

Standard DGPS	5 m
2nd Generation	75 cm
PPS DGPS	35 cm
Narrow Correlators	10 cm
Kinematic (Phase)	4 cm

In the future, there are plans to integrate the geodesic sphere with a quad-rotor. Because integration of the quad-rotor and geodesic sphere in inevitable one of the goals of this research endeavor was to acquire an appropriate quad-rotor. The quad-rotor decided upon and eventually purchased is the DJI Phantom II. Table 3 shows the horizontal and vertical positional accuracies claimed by DJI [13]. The standalone DGPS accuracy and those of the DJI Phantom II will be used for uncertainty analysis.

Table 3: DJI Phantom II Reported Accuracies

Horizontal (XY)	2.5 m
Vertical (Z)	0.8 m
Tilt (Roll/Pitch)	35°
Yaw Rotation	200°/s

2.6.4 IMU and RPY Frame of Reference

An inertial measurement unit IMU utilizes gyroscopes and accelerometers to estimate the relative position and pose of a vehicle. The IMU can estimate position in regards to the XYZ coordinates system and it can estimate pose in regards to roll, pitch and yaw RPY of the vehicle, in this case a quad-rotor. IMUs are strongly susceptible to drift errors in the XYZ coordinate system and must be augmented with a DGPS system or another system, such as a camera, to help correct for these errors [13]. For the purposes of this thesis, the assumption made is that hypothetically the two-way probe concept will be augmented with a DGPS system to correct for positional errors; therefore, positional errors associated with DGPS will suffice for uncertainty analysis conducted. In the case of pose errors, the IMU accuracies for RPY will be used since the IMU controls them.

Figure 13 is an illustration of the frame of reference in regards to RPY [14]. RPY is related to pose of the vehicle. Roll movements occur when the vehicle is moving left or right. Pitch movements occur when the vehicle moves forward or backward. And yaw movements occur when the vehicle is rotating about its center axis either right to left or left to right [14].
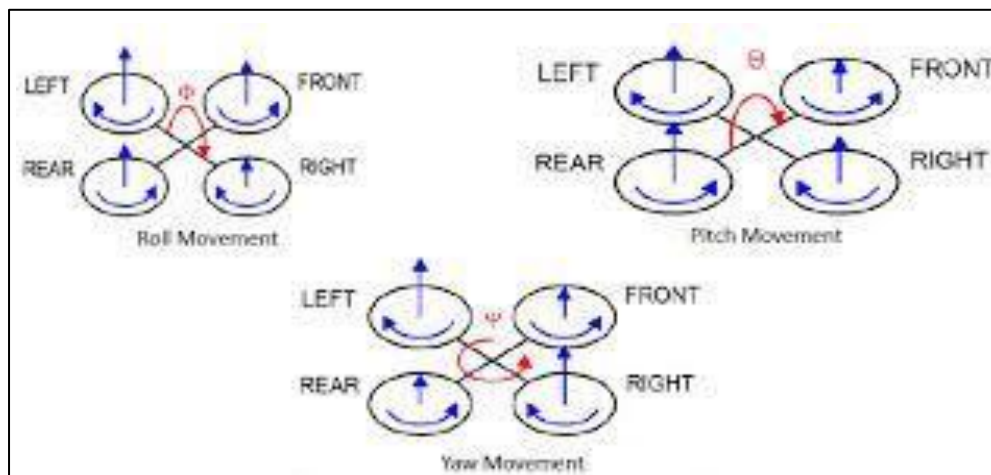
Figure 13: RPY Roll, Pitch, and Yaw Frame of Reference

Table 4 indicates the RPY root mean square error RMSE associated with a specific IMU. DJI specifications resource did not provide a specific brand of IMU nor did it provide any pose errors associated with RPY [12]. In addition, it is very difficult to find literature on accuracy errors associated with the IMU, so for the purpose of this thesis, the use of the RMSE developed by another researcher, Pradana [14], was utilized. Pradana was not clear on the meaning of the two numbers located next to each pose component. For the basis of this research, it was assumed that the first number represented the RMSE associated with that pose component and the second number represents the standard range of motion of that pose component. For instance, roll indicates 0 RMSE associated with it and the range of motion of the IMU and flight controls; with respect to roll is 0-45°.

Table 4: RPY Root Mean Square Error (RMSE)

APM 2.5	RMS Error
Roll (R)	0, 45°
Pitch (P)	0, 52°
Yaw (Y)	3, 34°

2.6.5 Computer Based Tool Background

One of the main goals of this thesis is the determination of a proper predictive and modeling tool for future RCS analysis of icosahedrons spheres. During the course of this research several tools were assessed. This section will provide a brief overview of the tools that considered.

27

Computer Simulation Technology Microwave Studio CST – CST is a powerful tool that provides both a robust modeling framework and equally robust simulation package. It offers the ability to conduct time domain, frequency domain, and integral solving packages. It also allows for modeling and simulation in wide-variety of scientific and engineering disciplines other than RCS measurements. AFIT's LOREnet provides the product for its students to use and holds the licenses. It can only be accessed through a LOREnet computer at AFIT.

In regards to this thesis, CST's integral solver was used for RCS analysis. The integral solver is specifically designed for conducting RCS measurements. It utilizes the computational electromagnetic CEM methods to integrate over each individual mesh cell to acquire the RCS of the object. Meshing is basically a method of enabling the computer to electrically and computationally 'see' the object of interest. CEM, like all computational methods, is an approximation of the RCS utilizing Maxwell's equations. Some advantageous of CEM over moment methods or finite element methods is that in CST boundary conditions are inherently represented which gives a closer approximation of Maxwell's equations [13].

A disadvantage of using CST is that it is computationally intensive and simulations can take a long time based on the complexity of the object geometry. Large objects of interest require finer meshing which can lead to more intensive calculations. [13].

4nec2 – 4nec2 or Numerical Electromagnetic Code is a modeling and analysis tool mainly specializing in the EM response of antennas [14]. It is unique in that its platform is based on wire moment methods for analyses of simulations and all modeling is constructed with wires. Numerical solutions to integral equations for induced currents over the surface of the model are used for determining the EM response of the object under test [14]. It is free to download straight from the internet and simple to install. Since it is free to acquire, AFIT does not provide

28

this tool. An advantage of using 4nec2 is that it is computationally fast. A disadvantage to using is the modeling tools can be difficult to use.

Matlab – ALPINE—ALPINE is specifically designed for RCS simulation and analysis. It provides a wide array of tools to aid in RCS analysis. It has a GUI interface that is easy to navigate and use. It also provides a relatively basic modeling package. ALPINE was developed by Dr. Peter Collins, head of the LORE group at AFIT.

For this thesis, the RCS pattern cut tool was primarily used to plot the RCS at a specific frequency and angle. This ALPINE tool allows for polar plot, line plot, and phase plot representations of the RCS data.

Matlab POFACET – POFACETS is another Matlab based tool that utilizes a form of RCS analysis called Physical Optics PO. The PO method "assumes that the induced current density on some scatterer of antenna surface is given by the geometrical optics current density…over those portions of the surface directly illuminated by the incident field, and zero over shadowed sections of the surface" [6, p. 118]. POFACETS is free to download and use. It provides a GUI interface.

Mercury MoM – Mercury MoM is a simulation tool based on the method of moments MoM. Since most simulation packages are memory intensive they can sap the speed of the computer's processor. MoM operates on being able to able to sample induced currents and charges on bodies approaching 10 wavelengths in size [3]. It is ideally suited for wire based models because it can computationally handle the complexity of intricate geometric models. MoM is available to use on AFIT's LOREnet computers.

FreeCAD-- FreeCAD is modeling platform that is free to download. It provides multiple options for modeling and allows for its models to be exported into other programs such as CST

and MoM. For this thesis, FreeCAD was the initial modeling platform used to attempt construction of a geodesic sphere.

ACAD – ACAD is a modeling tool that is provided by AFIT. One of its main features is its meshing tools, which provides multiple options for controlling a variety of aspects of the mesh which affects the prediction accuracy. Its models can be exported into a wide variety of programs such as MoM, CST, and FreeCAD. It can also import models from other programs and reconfigure their mesh for export into other file formats for other programs.

Specifically for this thesis, ACAD was used to remesh models imported from CST and then take those models and change their file format to that of a .facet file so that it can be exported into MoM. However, before MoM can read the file, the .facet file must be converted into a .geo file where it can then be used in MoM.

SketchUP – SketchUP is a free, downloadable CAD tool. One of its main advantageous is that there is a large database of CAD models contributed to by other users. These models are free to download for personal use.

2.7 Summary

This chapter provided background and technical information into the multiple disciplines required for this thesis. Understanding basic radar principles is paramount to understanding the role of RCS, what it is, and the methods by which it is obtained. RCS measurements can be made on either an indoor or an outdoor range. The RCS measurements taken for this thesis were done in an indoor range, the ACR. However, the uncertainty analysis will be based on the physical dimensions of the NRTF, Figure 2, which is an outdoor range. The test item designed for the RCS measurements is a 2v truncated icosahedrons sphere. Determining its back scatter or RCS characteristics, through both theoretical and measured methods, will aid in determining a

proper predictive tool to use for theoretical measurements and whether or not the sphere can shield an internal object's RCS from the radar antenna. As stated earlier, uncertainty measurements, specifically positional and axial uncertainty analysis, are a major part of this thesis's goals; that is why an understanding into DGPS is pivotal to thesis, because it is one of the means by which position is tracked.

III. Methodology

3.1 Chapter Overview

This thesis has two goals. First, construct a geodesic sphere and then determine a proper prediction tool for RCS measurement by validating the prediction results to the experimental results obtained on an indoor radar range. Parallel to determining a proper prediction tool, this thesis will determine whether or not a geodesic sphere can sufficiently shield the RCS of an inner object from the radar antenna. Construction of the geodesic sphere has already been discussed in chapter 2 of this thesis; therefore, this chapter will outline the measurement process that is carried out to characterize the RCS behavior of the sphere and the predictive techniques that were utilized to validate this process.

The second goal of this thesis is to analyze whether or not position and pose uncertainties have an impact on the RCS measurement taken. The proposed approach is to use Monte Carlo techniques to randomly generate numbers and determine the RCS magnitude and phase uncertainties associated with the position and pose. This chapter will outline the Monte Carlo process used.

3.2 RCS Measurement

RCS measurements were taken at the ACR, which is an indoor radar range located at Wright Patterson AFB, OH. Because the range was not an AFIT owned asset there was limited opportunity with operating the radar firsthand. However, the ACR did an excellent job with catering to the needs of the experiment.

Intuitively, it would make sense to develop a computer model of the sphere and run prediction models first. However, since the AFIT radar range is inoperable for an indeterminate

amount of time it made it impossible to pass up the offer from the ACR to measure the sphere.

Figure A.1, in Appendix A, is the measurement log used by the ACR to chronicle the measurement process.

3.3 Radar Calibration Process

Before the start of any RCS measurement it is necessary to take background and calibrated measurements with the radar. The reason for this is to calibrate the radar and ensure that the measurements of the objects are as precise as possible. On any radar range, whether it is outdoor or indoor, radar engineers must contend with and account for the reflections coming from the ground plane, target pylons, foam mounts, and even the string systems used for suspending objects [3, p. 483]. To accomplish the calibration, the method in which this is done is by subtracting the background and calibrated measurements from the actual object measurements. Equation 15 is the standard equation used to calculate these background measurements and is the equation used by ACR to conduct their calibration process [13]. The below equation and accompanying definitions were provided in the ACR report for the measurement of sphere [13].

$$\sigma_{TAR}(\omega, \alpha) = \left[\frac{E_{TAR(\omega,\alpha)} - E_{bkg}(\omega, \alpha)}{E_{cal}(\omega) - E_{cbk}(\omega)} \right] * \sigma_{exact}(\omega) \tag{13}$$

E_{TAR} = reference object frequency response
E_{bkg} = background frequency response
E_{cal} = canonical object (squat cylinders 15"/18") frequency response
E_{cbk} = object background frequency response
σ_{exact} = calculated RCS of the reference object

The ACR report indicates that they were not able calibrate the radar system to the level of precision that they are accustomed to and because of time restraints a solution would have to found at another time. As indicated in the report, the ACR calibration performance must fall within ± 1 dB of error [14, p. 18]. Vertical (VV) polarization measurements fell within these bounds; however, horizontal (HH) polarization fell outside this allowable error, Figure 14.
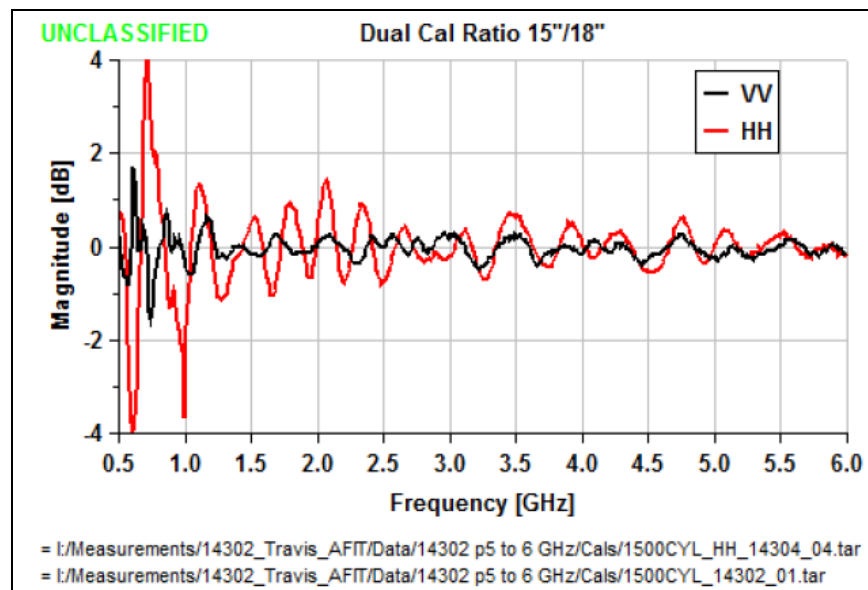
Figure 14: VV & HH Dual Calibration Ratio 15in/18in [14]

The remainder of the calibration results can be found in Appendix B of this thesis. Essentially, prior to making actual experimental measurements it is necessary to ensure that the radar system is calibrated and functioning properly. To avoid erroneous measurements, calibration and background subtraction are the first step of the process in ensuring this occurs. Even though the HH polarization in Figure 14 indicated a source of possible error, it will be shown later that this error had minimal impact on the overall measurements taken.

3.4 RCS Characterization

Once calibration has been accomplished, then RCS measurements of the object commence. Figure A.1, located in Appendix A, is the measurement log that indicates the order in which object were measured. Table 5 is a abbreviated version of Figure A.1.

Table 5: Abbreviated Target Measurement Log

Object	HH Pol Only	VV Pol Only	HH Pol Pentagon Down	VV Pol Pentagon Down	HH Pol Hexagon Down	VV Pol Pentagon Down
Flat Plate	x	x	-	-	-	-
Dihedral	x	x	-	-	-	-
Sphere	-	-	x	x	x	x
Sphere w/ Flat Plate	-	-	x	x	x	x
Sphere w/ Dihedral	-	-	x	x	x	x

The two internal objects chosen to be integrated with the sphere and measured are the flat plate and dihedral. These shapes are classified as canonical shape because they have known RCS patterns. The dihedral represents a more complicated object than the flat plate and will provide an alternate scattering source with known RCS patterns. All object configurations are measured in both horizontal and vertical polarization to determine the effects. For all sphere measurements and combinations thereof, the sphere is measured in two configurations: pentagon down, Figure 15 and hexagon down, Figure 16. The sphere positioned with the pentagon down horizontally aligns the central ring across the sphere's equator. The sphere positioned with hexagon down vertically aligns the central ring. The hypothesis here is that the change in pose of the sphere will affect the RCS measurements taken.

The main purpose of the RCS measurements is to provide the RCS frequency, angle, and polarization dependencies for use in uncertainty analysis. In addition, it is also necessary to determine the upper frequency where the sphere cage allows the illuminating field to interact significantly with the internal structure.
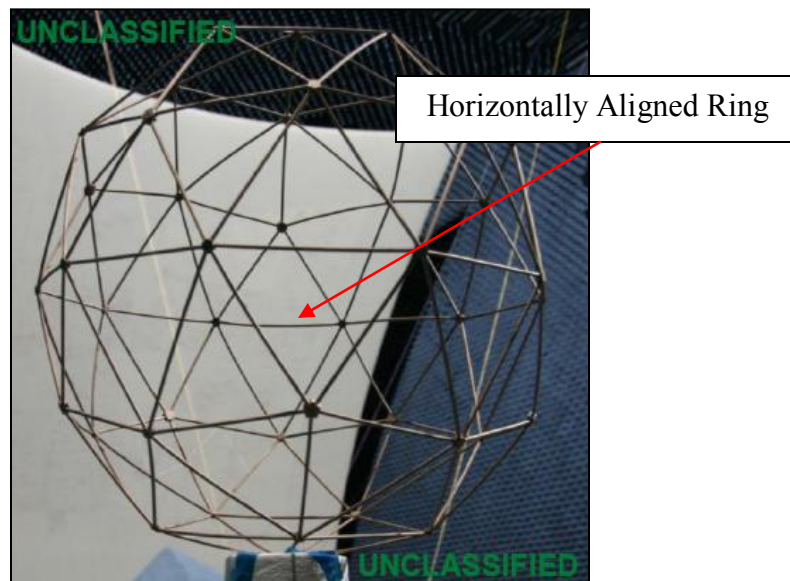
Figure 15: Pentagon Down, Horizontally Aligned Ring
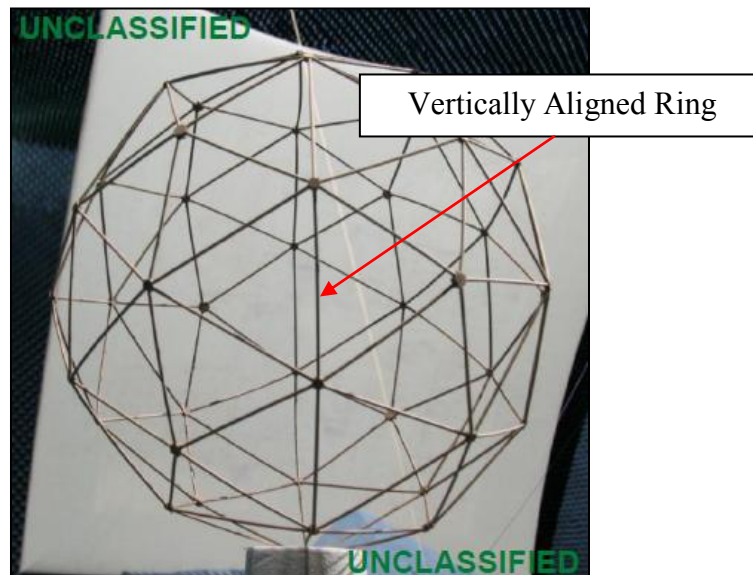
Figure 16: Hexagon Down, Vertically Aligned Ring

After the calibration and background process is completed, test item setup was conducted. Prior to mounting and measuring the sphere it was necessary to measure the RCS of the internal objects by themselves. The flat plate and dihedral are mounted and measured alone. Following those measurements, the sphere is measured by itself. The solo measurements of the sphere and objects provide a baseline for comparing and contrasting to internally mounted test item/sphere measurements.

The geometry and structure of the sphere makes it difficult to set on the test item mount without it falling off. In order to secure it to the mount it was necessary to notch out grooves in the top of the mount so that the struts of the sphere can sit in the notched out grooves of the mount without rolling off. To further secure the sphere to the foam mount, the sphere was taped down to it Figure 17.
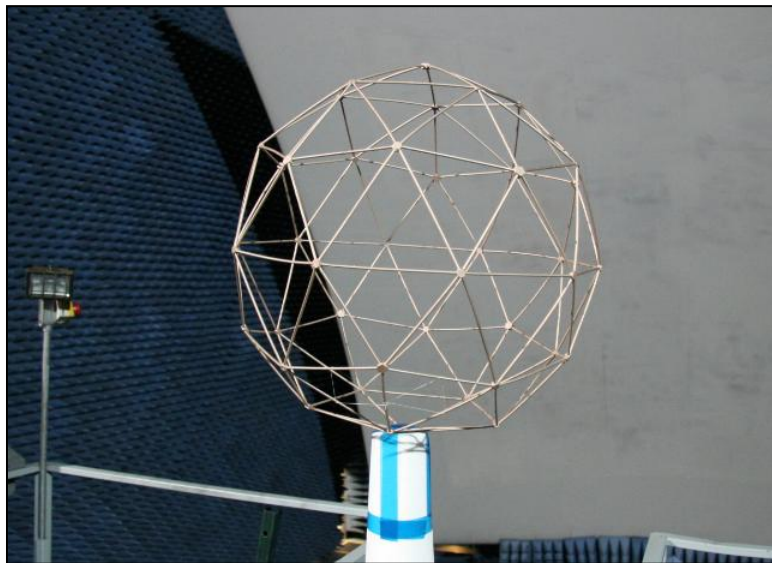
Figure 17: Geodesic Sphere Mounted to Foam Mount [14]

After the sphere was mounted RCS measurements were taken with no internal objects mounted inside. The reason for this is simply to have a 'before' image of the sphere to compare to measurements of the objects mounted in the sphere. Figure 18 and Figure 19 show the mounted flat plate and dihedral respectively. As indicated in Table 5, each test item was measured with the sphere's hexagon down and pentagon down, meaning the sphere was mounted the hexagon sitting on the mount and then the pentagon sitting on the mount. Additionally, horizontal polarization and vertical polarization measurements were taken for each position the sphere was mounted in. Results and analysis of the measurements will be discussed in chapter four.
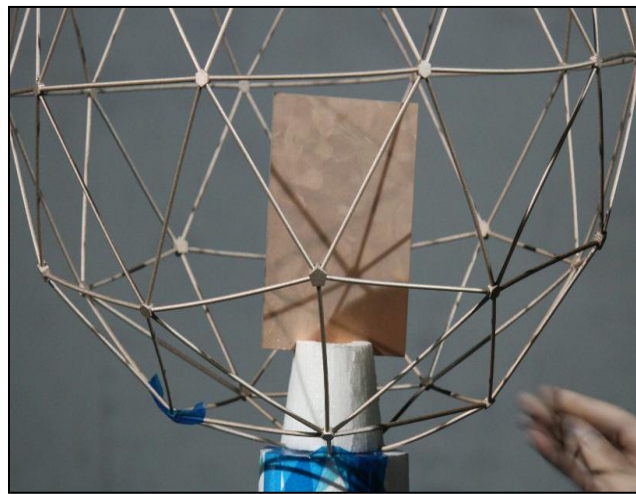
Figure 18: Flat Plate Mounted in Geodesic Sphere [14]
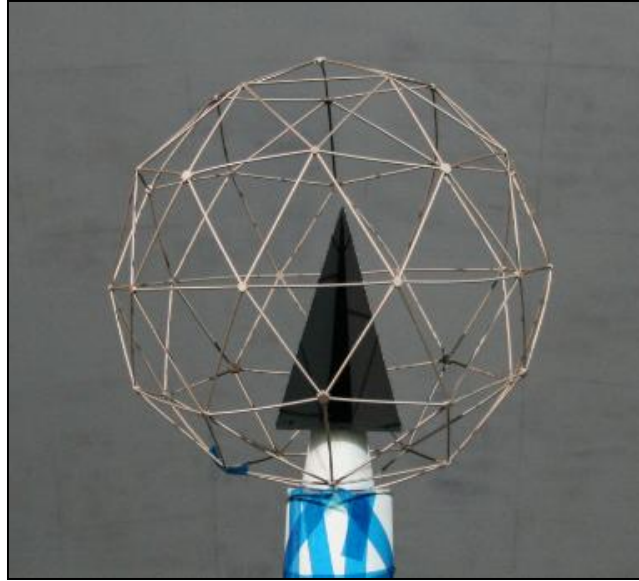
Figure 19: Dihedral Mounted in Geodesic Sphere [14]

3.5 Predictive Tool Determination

Another important avenue of research was the determination of a computer based tool that provided the most efficient and best predicative measurements. In order to determine if a tool was sufficient enough several questions need to be answered:

1. Modeling: Determine which computer based tool provides easiest method of modeling a geodesic sphere?

2. Simulation: Determine which computer based tool provides predictive RCS results and has good agreement to the experimental results?

3. Time: Determine which modeling/predictive tool, or combination thereof, is easy to use and provided timely results?

3.6 Uncertainty Analysis and the Monte Carlo Approach

The final step in this thesis will be to investigate the positional and axial uncertainty associated with the DGPS and the quad-rotor's IMU. In chapter two, it was shown in Equation 4 that the square root of the RCS was proportional to scattered electric field, E_s. This relationship is taken a step further in Equation 14,

$$\sqrt{\sigma}(\bar{r},\hat{e},f,\theta,\varphi) \propto \bar{E}_s(\bar{r},\hat{e},f,\theta,\varphi) \tag{14}$$

this illustrates the relationship between the RCS and the scattered electric field. It shows that each is a function of $\bar{r}$ = position, $\hat{e}$ = polarization, f = frequency, θ = theta, and φ = phi, since both are proportional to each other it makes sense that this would be the case.

3.6.1 Uncertainty Analysis

The uncertainties associated with the DJI Phantom II quad-rotor will be the model and basis for this uncertainty analysis because it was purchased for sole intent of being the chosen platform for the two-way antenna.

Positional uncertainty will be related to the horizontal and vertical uncertainties reported by the DJI Phantom II, Table 4 [13]. This uncertainty is related to the position vector, $\bar{r}$. A Monte Carlo simulation will be used to determine the degree of position error that can be expected by the DJI and the question answered as to whether or not that position error will affect RCS measurements. Angular uncertainties can be related to the DJI's roll, pitch and yaw errors. In regards to Equation 14, roll $\propto \hat{e}$ or polarization, $\theta \propto$ pitch, and $\varphi \propto$ yaw are the three random variables which will be investigated for error, thus, $RPY = \hat{e}, \theta, \varphi$. Uncertainty analysis for this

thesis will focus on the following random variables, XYZ and RPY which constitute the six degrees of freedom or 6DOF analysis.

3.6.2 The Monte Carlo Approach

For the Monte Carlo process, this thesis will follow the steps of executing a Monte Carlo simulation as presented by Dr. Byron Welsh [15]. Figure 20 is a flow chart depicting the Monte Carlo process that is used for this thesis.
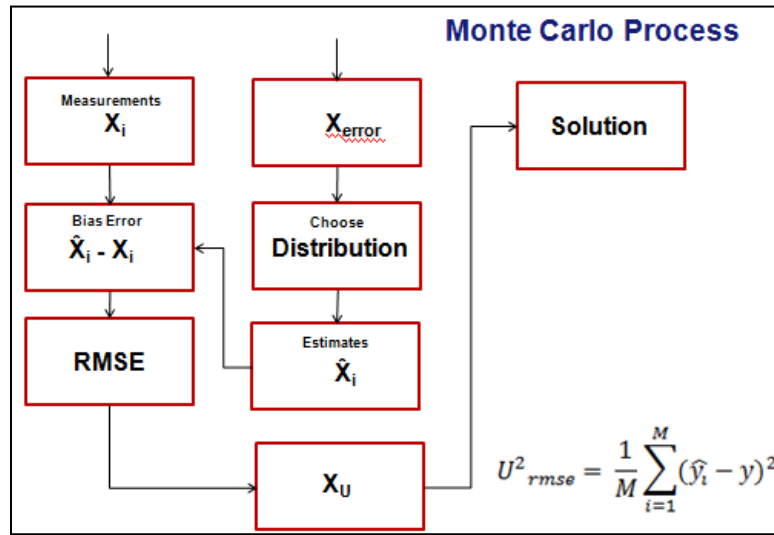
Figure 20: Flow Chart Dr. Welsh's Monte Carlo Process

The first step in the process is to decide what the random variable will be. The random variables associated with thesis are the components errors, X_{error}, of the DGPS and IMU systems, which are the XYZ position errors and RPY pose errors.

The next step is to decide upon an appropriate distribution, which can be a probability distribution function PDF or a continuous distribution function CDF, that best describes behavior of the component errors. This distribution will be used to randomly generate estimated values of the model [15]. For this thesis, it is assumed that all component errors fall into a normal Gaussian distribution,

$$\Delta x_i = N(\mu_i, \sigma_i) \tag{15}$$

It is then necessary to establish actual measurement data that represent the system. This measurement data can either come from actual measurements taken, which is the best case scenario for accurate uncertainty analysis or it can be estimated. This estimation is normally based on previous experience of the system's behavior or an idealized measurement model can be declared [19]. In regards to this thesis, an idealized point scatterer will be modeled to estimate measurement data.

Following the establishment of estimated or real measurement and random generation of predicted estimates based on the component errors it is necessary to use Equation 16,

$$\Delta x = \hat{x}_i - x \tag{16}$$

to calculate the bias error each measured and corresponding estimated value. Bias error is the difference between the measured value and estimated value.

Finally, the RMSE is calculated using Equation 17,

$$U^2{}_{rmse} = \frac{1}{M}\sum_{i=1}^{M}(\hat{x}_i - x)^2 \tag{17}$$

Equation 17 is the root mean square error RMSE and is a measure of the uncertainty between predicted values and measured values [15]. More specifically, the RMSE is a measure

of the spread of the y-values around the average, since a normal distribution is assumed, where 68% of the x-values fall within one RMSE of the predicted values and 95% of the y-values fall within two RMSE of the predicted values [17].

3.7 Summary

For this research endeavor it will be necessary to first evaluate the RCS measurements of the sphere to provide an empirical model of the angular and polarization dependencies of the sphere and to determine the upper frequency where sphere is no longer able to shield the quad-rotor. After determining these characteristics, a proper predictive tool will be established by comparing measured values to predictive values. Along with accuracy of prediction, it will also be necessary, in the search for a good predictive tool, to determine the speed of which predictions are made. Having a good prediction tool presupposes having a good computer generated model as to which one would make a prediction. Thus, part of this thesis will be determining which computer aided design program is easy and efficient to use. Finally, using Welsh's five steps, uncertainty analysis will be conducted along the 6DOF. This analysis will aid in establishing error tolerances and confidence in measurements.

IV. Analysis and Results

4.1 Chapter Overview

This chapter provides detailed analysis and results of the goals of this thesis. First, an analysis of the results for the RCS measurements taken at the ACR will be evaluated. The results will be used to determine which frequencies, polarizations, and poses are ideal for RCS shielding and illumination. Following the evaluation of the measured RCS, there will be a comparison of the various computer based tools used for both modeling and simulation. Finally, a comprehensive review of the results of the uncertainty analysis will be conducted.

4.2 Geodesic Sphere RCS Measurements

Evaluating the backscatter field from the sphere is the first step of this thesis. As stated in chapter three, the process for evaluation followed the following process:

1. Measure and evaluate sphere and internal test item separately in both polarizations and both poses (hexagon down and pentagon down) if applicable

2. Measure and evaluate the test items mounted in the sphere in both polarizations and both poses (hexagon down and pentagon down)

The ACR's experimental results can be found in Appendix C. The experimental results used in this chapter were generated from the raw values of the experimental data supplied by the ACR. The RCS data was processed in Pioneer, the same platform the ACR uses to process its measurements.

4.3 Solo Test Item and Solo Sphere Measurement Results

4.3.1 Flat Plate Solo

Figure 21 is a graphical depiction of the RCS scattering results from measurements taken of the flat plate mounted alone on the test item mount. Figure 21 was measured with horizontal polarization, at frequencies between 1-6 GHz. Specular reflections of the flat plate are indicated in the figure, which are the areas of highest RCS returns because the flat plate's normal is facing the radar. As the flat plate rotates, edge diffractions at approximately 90° are indicated in the figure, which illustrates that the flat plate's orientation to the radar is of its thinnest edge facing it. The edge diffractions are of the lowest RCS magnitude and are due to the polarization chosen to measure.
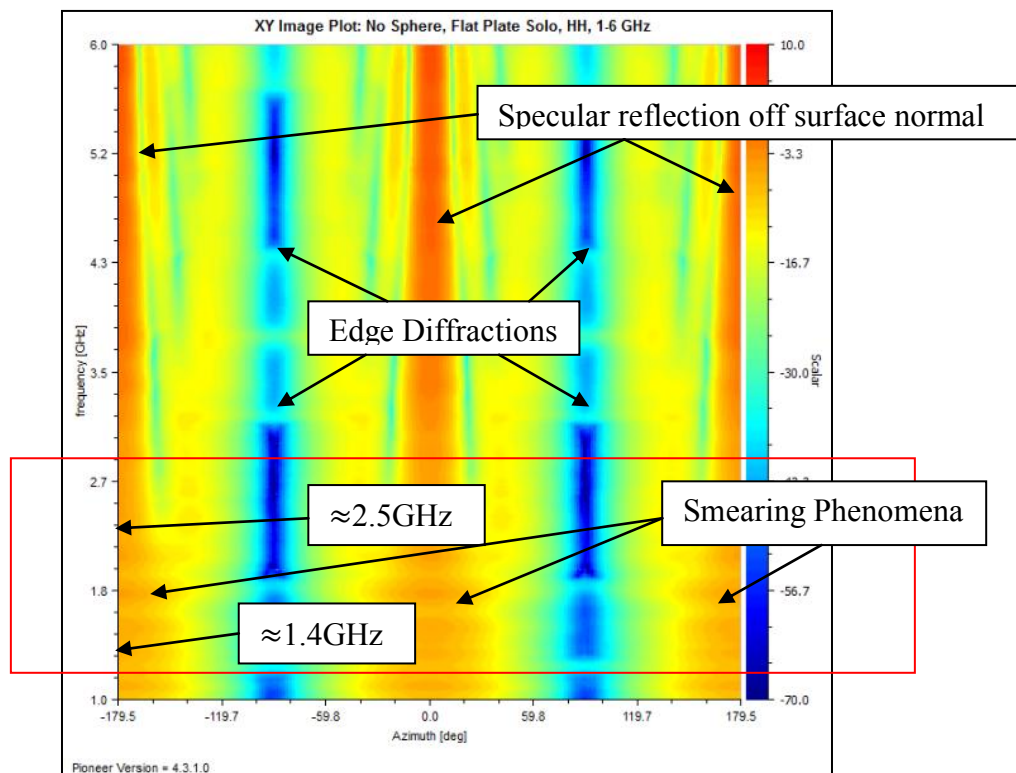
Figure 21: GFP - Flat Plate HH, 1-6 GHz

Figure 22 is the vertical polarization measurement of the flat plate. Clearly there are no weak edge diffractions occurring at 90°. Specular response is strong when the flat plate is oriented with its surface normal facing the radar. In both Figure 21 and 22, a smearing phenomena is occurring between approximately 1.4-2.5 GHz. This smearing appears to be strongest in the horizontal polarization, Figure 21. The difference in the level of smearing can possibly be attributed back to the ACR's calibration issues with horizontal polarization. Smearing aside, Figure 22 indicates that as the frequencies become smaller, the longer wavelengths are having more difficulty measuring the specular regions of the flat plate.
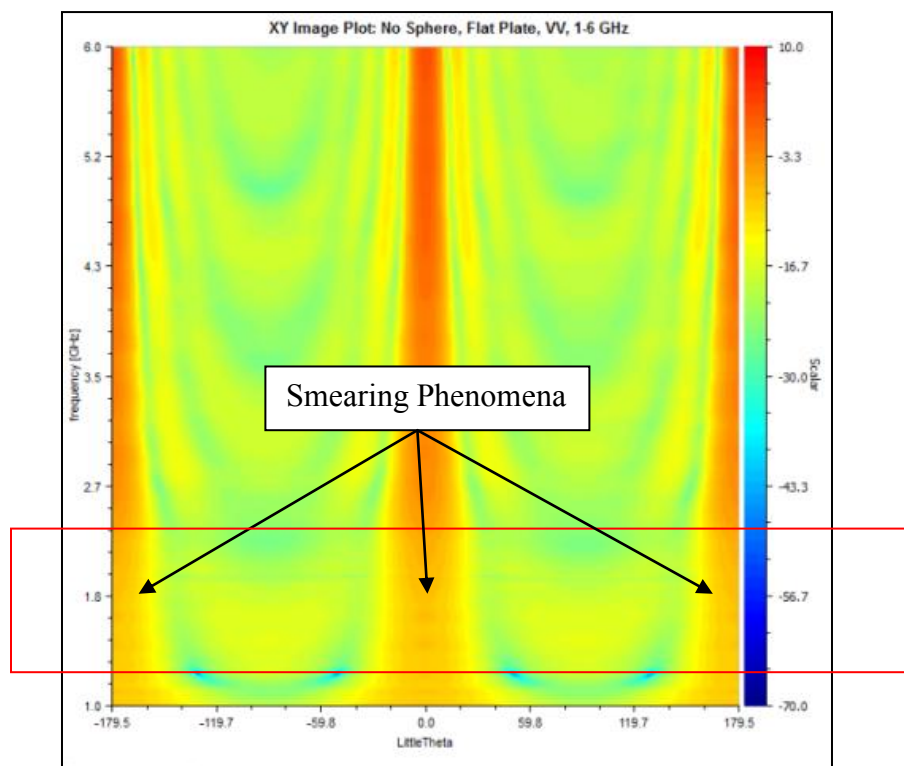
Figure 22: GFP - Flat Plate VV, 1-6 GHz

4.3.2 Dihedral Solo

Figures 23 and 24 are global frequency plots of the dihedral measurements. Figure 23 was measured in vertical polarization. Its strongest specular response occurs at approximately 120° for both vertical and horizontal polarizations. Between 0° and 60° the orientation of the dihedral is with its opened end facing the radar. The RCS pattern between those angles indicates reflections bouncing off the inner faces of the dihedral as it rotate.
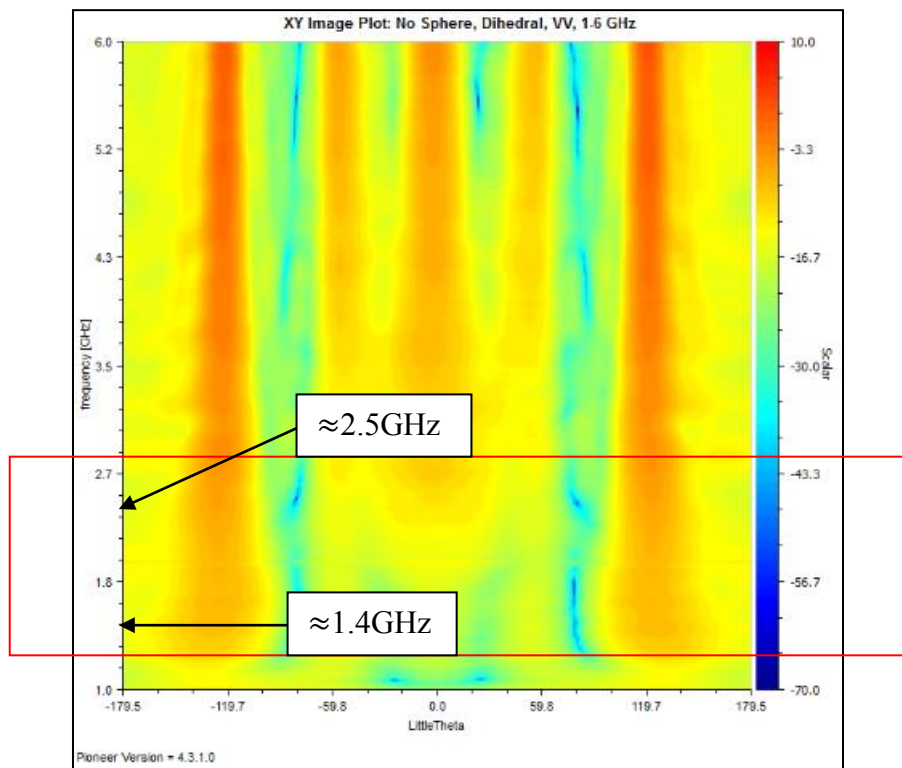
Figure 23: GFP - Dihedral VV, 1-6 GHz

In both Figures 23 and 24, between 1.4-2.5 GHz there appears to be the same smearing phenomena happening again that occurred in the flat plate measurements. These early indications point to a possible low and high frequency of interest, which might be an ideal operating frequency band for the geodesic sphere in regards to shielding and illumination.
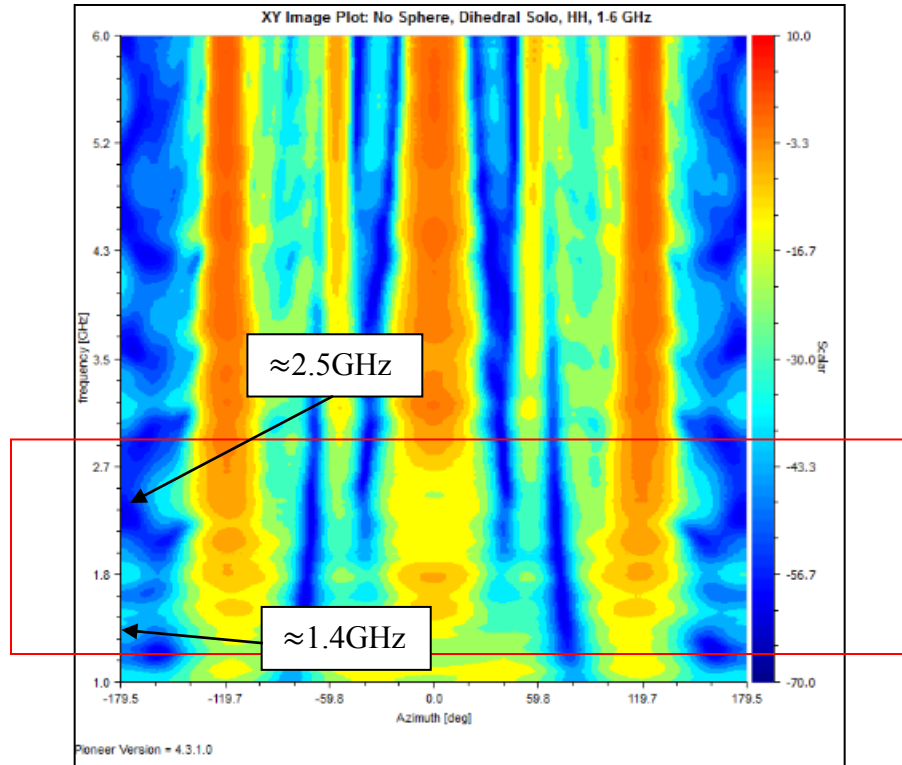
Figure 24: GFP - Dihedral HH, 1-6 GHz

4.3.3 Sphere Solo Hexagon & Pentagon Down, HH

Figures 25 and 26 are global frequency plots of the sphere, by itself, oriented with the hexagon facing down and the pentagon facing down respectively. Both measurements are taken with horizontal polarization. It is important to remember, that in Figure 15, from chapter 2, the sphere is oriented on its pentagon causing the center ring of the sphere to be aligned horizontally to the radar. In Figure 16, the sphere is oriented on its hexagon, causing the center ring to be oriented vertically with respect to the radar.

In Figure 25, the red rectangle approximately represents the frequency band of interest, 1.4-2.5 GHz. The sphere is oriented with its hexagon down, which would indicate its center ring is vertically aligned. Between 2.7-6.0 GHz, it appears the radar is illuminating portions of the

48

spheres structure. However, at these frequencies the wavelengths are shortening to the point where the radar has difficulty illuminating the sphere. Again, between 1.4-2.5 GHz, the strongest RCS reflections are occurring. At approximately 1.4 GHz there appears to be a significant backscatter occurring across periods of theta. For instance, between approximately 30° and 40° the RCS is approximately -8 dBsm. Then there is a period of low RCS return between 60° and 65° until the pattern repeats again starting at approximately 70°.
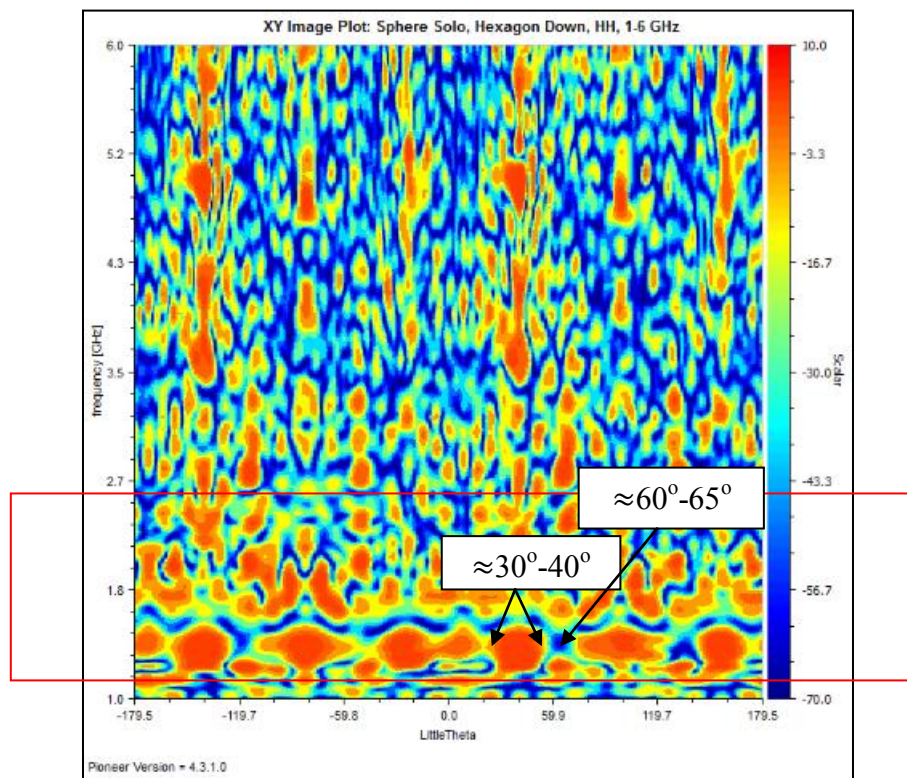
Figure 25: GFP - Sphere, Hexagon Down, HH, 1-6 GHz [13]

Figure 26 is the frequency plot taken with the sphere's pentagon oriented down. With the pentagon facing down, the center ring is now horizontally aligned. Again the red box indicates the frequency band of interest, 1.4-2.5 GHz. This plot indicates that with the pentagon facing down, there is a stronger RCS backscatter occurring at approximately 1.4 GHz than there is with

the hexagon oriented down. In addition, between approximately 2.5-3 GHz there appears to be clear a region of transition, indicated by the black box, where the sphere structure goes from being visible at 2.5 GHz to not being visible at 3.0 GHz.
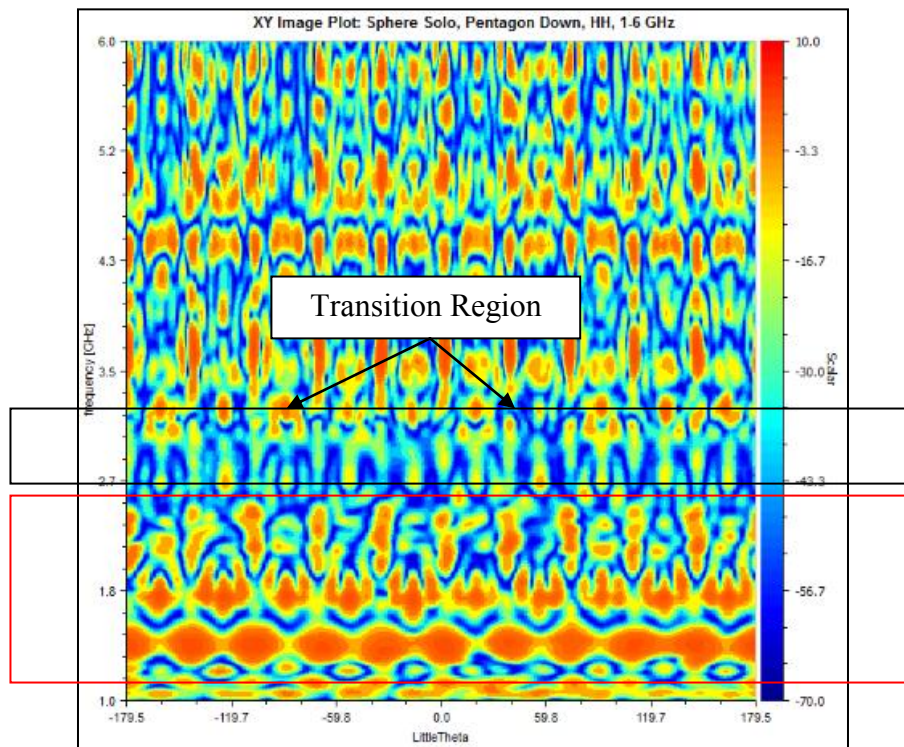
Figure 26: GFP - Sphere, Pentagon Down, HH, 1-6 GHz [13]

4.3.4 Solo Sphere Hexagon and Pentagon Down, VV

Figures 27 and 28 are global frequency plots of the sphere oriented with both hexagon down and pentagon down, repectively. The measurements are taken with vertical polarization. Remember, with the hexagon is oriented down so the center ring of the sphere is vertically aligned, which explains why there is significant structurural RCS returns, indicated by the black boxes, occurring between -60°-0° and 120°-175°. In Figure 27, the red box is highlighting a transistion occuring between 2.5-3.0 GHz where the sphere's structure is becoming more difficult to see.
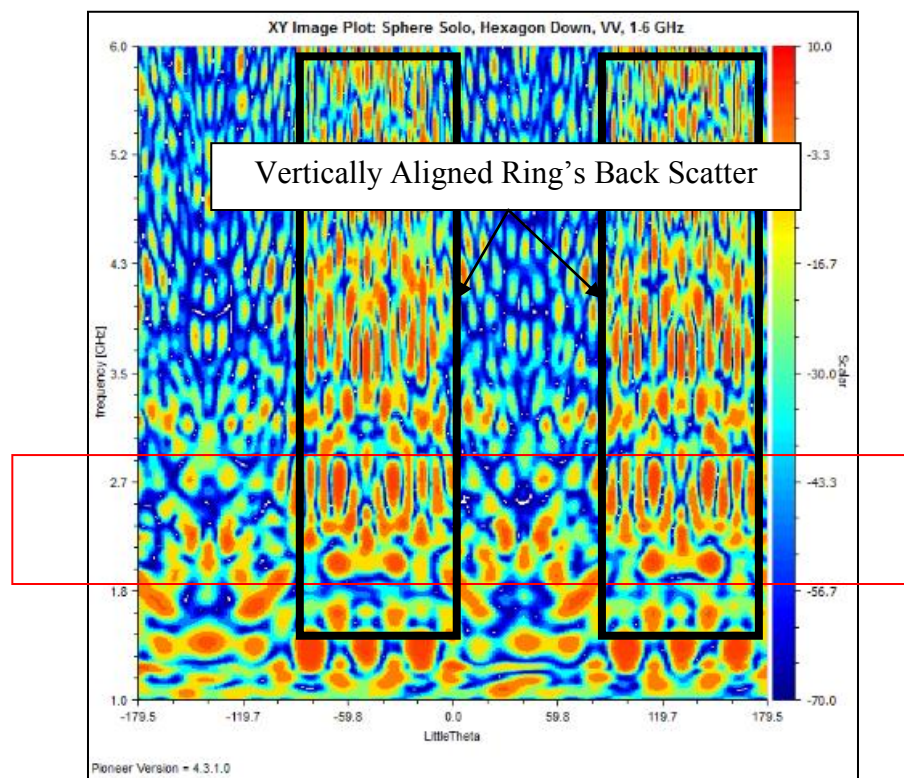
Figure 27: GFP - Sphere, Hexagon Down, VV, 1-6 GHz [13]

Figure 28 depicts the sphere with its pentagon now facing down. Again, the center ring of the sphere, in this pose, is horizontally aligned. Again the red box indicates a frequency band of interest, 1.4-1.8 GHz, where the sphere's structure is causing significant returns. The black indicates another frequency band of interest, where there appears to be a transition occurring between 2.5-3.0 GHz, where the sphere's structure is not as readily observed.
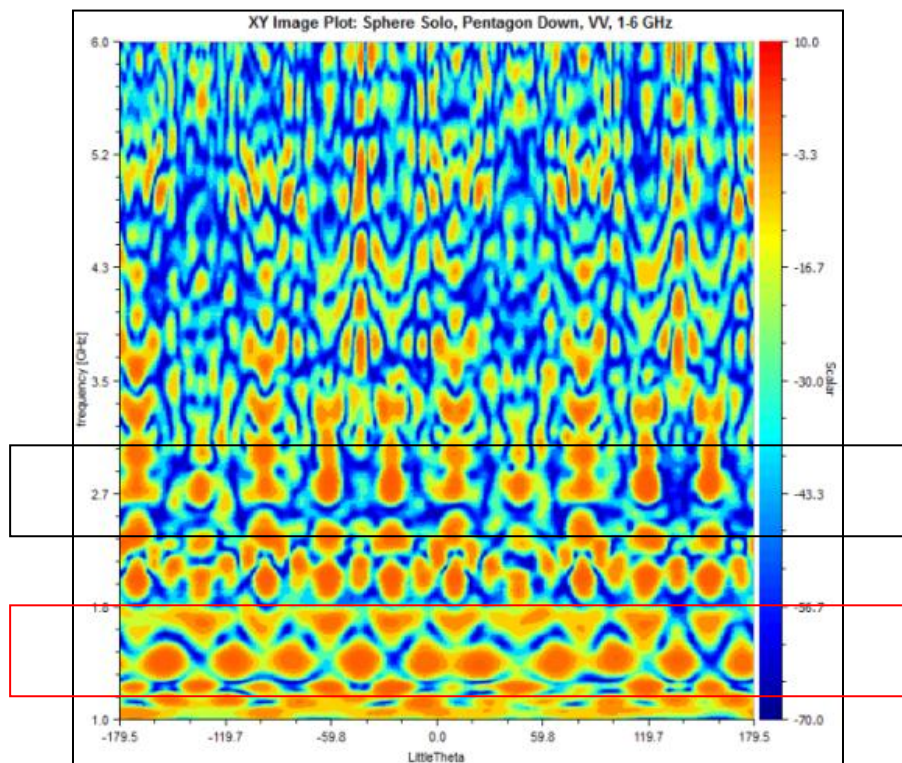
Figure 28: GFP - Sphere, Pentagon Down, VV, 1-6 GHz [13]

Figures 21, 22, 23, and 24, which are the measurements of the flat plate and dihedral by themselves, indicates a notional frequency band of 1.4-2.5 GHz where the radar is having more difficulty clearly seeing the test items. According to Figures 25, 26, 27, and 28 it also notionally appears that measurements taken with horizontal polarization, pentagon down, and between the frequency band of 1.4-2.5 GHz will produce the ideal conditions to first shield an inner target (1.4 GHz) and act as a two-way field probe (2.5 GHz). Table 6 is a summary of the results for the solo test items, which supports the claim that the sphere, oriented with pentagon down, produces the highest RCS return in either polarization.

4.4 Sphere with Internal Test Item

The results from the solo measurements of the flat plate, dihedral, and sphere point to an optimal shielding frequency of 1.4 GHz and a possible two-way probe illumination frequency of 2.5 GHz. At these frequencies the wavelengths become longer making it difficult for the radar to detect the flat plate and dihedral. At the same time though, the longer wavelengths allow the radar to see the illumination of the geometry of the sphere's struts; thus allowing it to act as a two-way probe. Knott explains in his book, Radar Cross Section [2], that there is an inverse relationship between the affected area, A, of the object being illuminated and the wavelength (λ) of the frequency being transmitted, where $\sigma \propto A/\lambda^2$. Thus, for a large surface area higher frequencies will produce better backscatter returns. However, for a smaller surface area, such as an area the size of the struts used to construct the sphere (which are only 0.157in in diameter), a smaller frequency with a large enough wavelength is needed to see their backscatter ($\lambda = c/f$, where c in the speed of light) [2].

This section will validate the results of the previous section which indicate the ideal polarization to be horizontal, the ideal orientation to be pentagon down, and the ideal frequency band to be 1.4-2.5 GHz.

4.4.1 Sphere w/Flat Plate

Figures 29 and 30 are global frequency plots of the sphere with a flat plate mounted inside. In both figures, the sphere is oriented with the hexagon down. Figure 29, the sphere is measured in horizontal polarization. The specular return from the flat plate can be seen. The flat plate's specular response appears to weaken as it approaches 2.5 GHz. After 2.5 GHz, the sphere's structure becomes the dominant scatterer where, at 1.4 GHz the strongest returns are occurring.
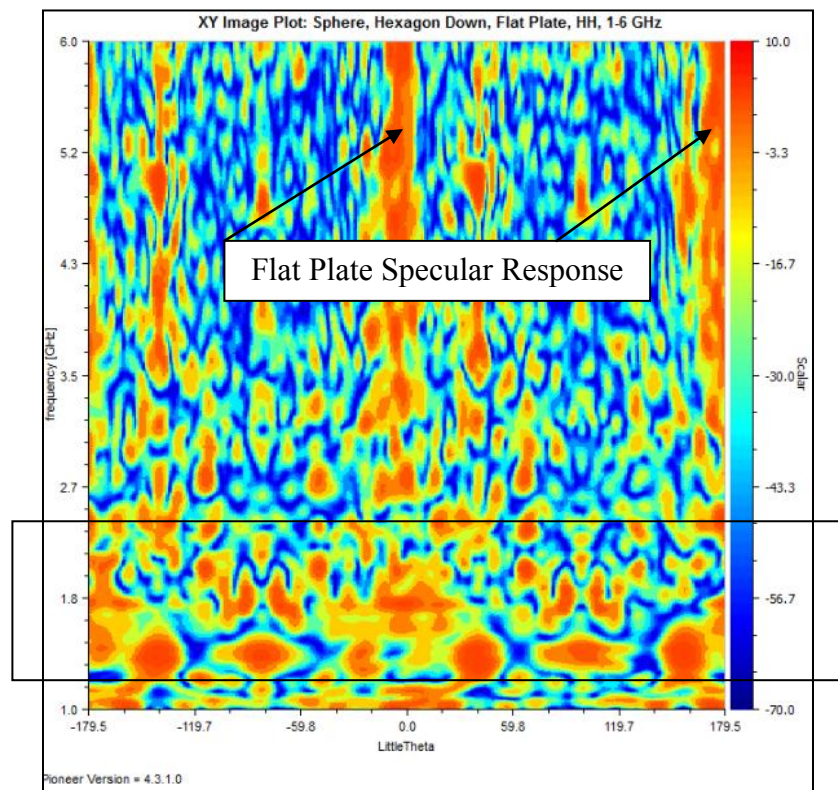
Figure 29: Sphere w/Flat Plate, Hexagon Down, HH

Figure 30 is a global frequency plot with the same test item setup as Figure 29. However, this measurement was taken with vertical polarization. The flat plate specular response can clearly observed. With hexagon down, the sphere's center ring is vertically aligned and can be observed. Comparing Figure 30 to Figure 29 it can clearly be observed that the vertical polarization is not producing a consistent RCS response across the frequency band of interest, 1.4-2.5 GHz, as indicated by the black box. There are large areas of insignificant RCS response as indicated areas colored blue.
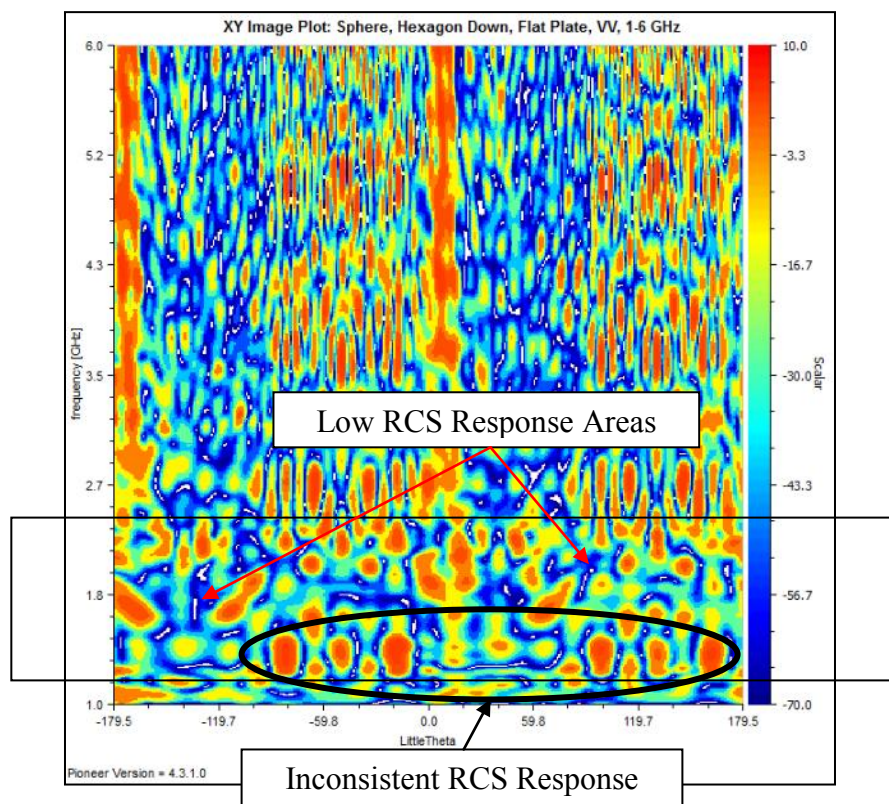
Figure 30: Sphere w/Flat Plate, Hexagon Down, VV

Figure 31 and 32 shows the frequency response of the sphere, mounted with the flat plate inside, pentagon down, and measured in both horizontal and vertical polarizations respectively. When compared to Figures 29 and 30, both plots indicate that the sphere oriented with pentagon

down produces strong and consistent (across all angles) RCS backscatter from the sphere in the frequency band of interest, 1.4-2.5 GHz (as indicated by the black box overlaid on the plot). When comparing Figures 31 to 32, it is clear that horizontal polarization produces the stronger and more consistent (across all angles) RCS response from the sphere. Figure 31 shows the specular response of the sphere beginning to weaken as it approaches approximately 2.5 GHz. And again at 1.4 GHz, there is a very strong RCS response occurring.
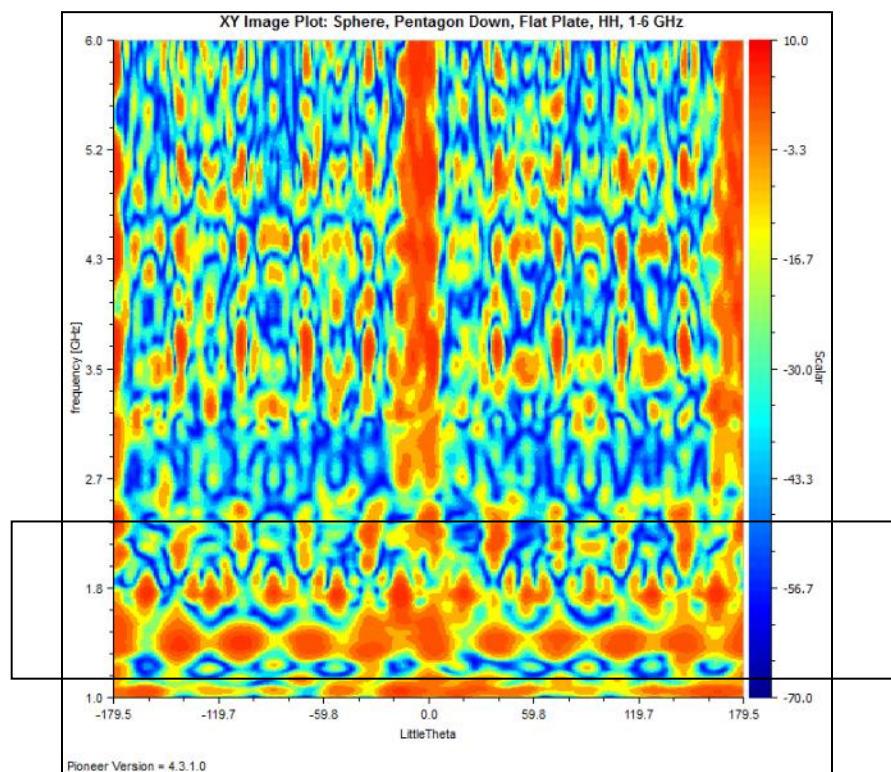
Figure 31: Sphere w/Flat Plate, Pentagon Down, HH
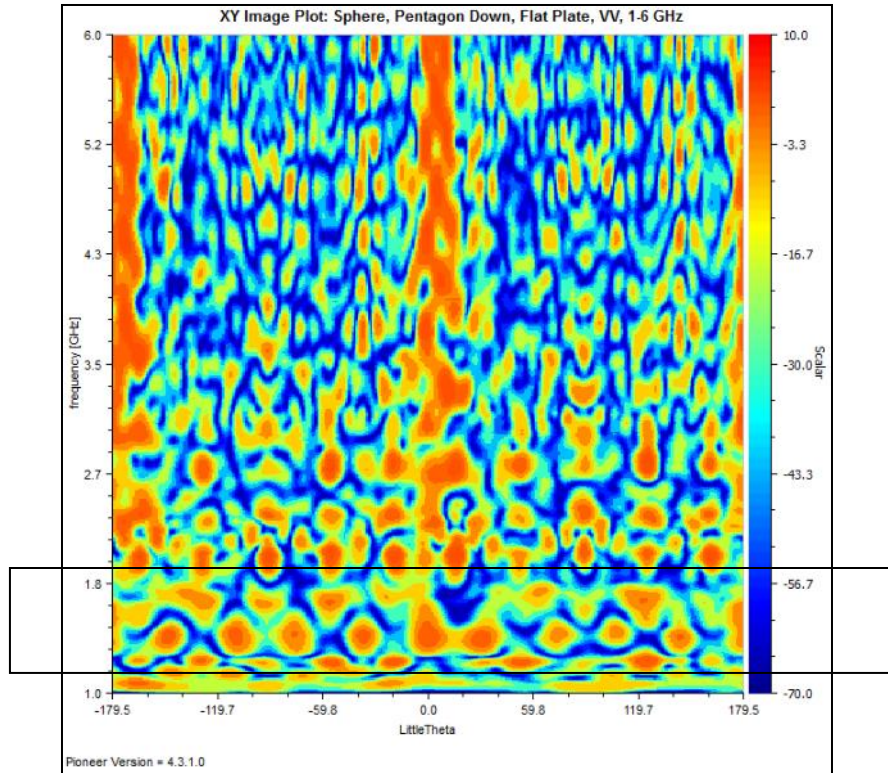
Figure 32: Sphere w/Flat Plate, Pentagon Down, VV

4.4.2 Sphere w/Dihedral

Figures 33, 34, 35, and 36 are the results of the measurements taken with the dihedral mounted in the center of the sphere. The RCS behavior pattern for the dihedral and sphere interactions is consistent with that of the flat plate. The results reiterate that measurements taken with horizontal polarization, with the sphere oriented with the pentagon down, and measurements taken within the frequency band of interest, 1.4-2.5 GHz, produces the ideal shielding and scattering two-way probe.
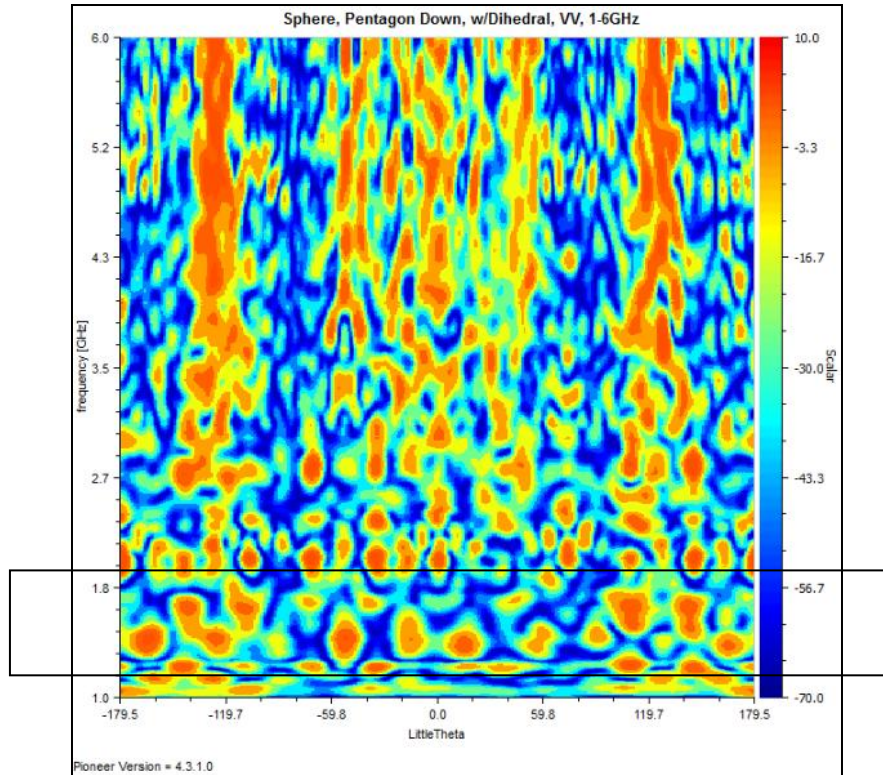
Figure 33: Sphere w/Dihedral, Pentagon Down, VV

Figure 33 illustrates again that vertical polarization produces weaker scattering from the sphere within the frequency band of interest, yet the dihedral's backscatter response is clearly weaker in that region to. However, the weaker backscatter response would probably not be ideal for the two-way probe.
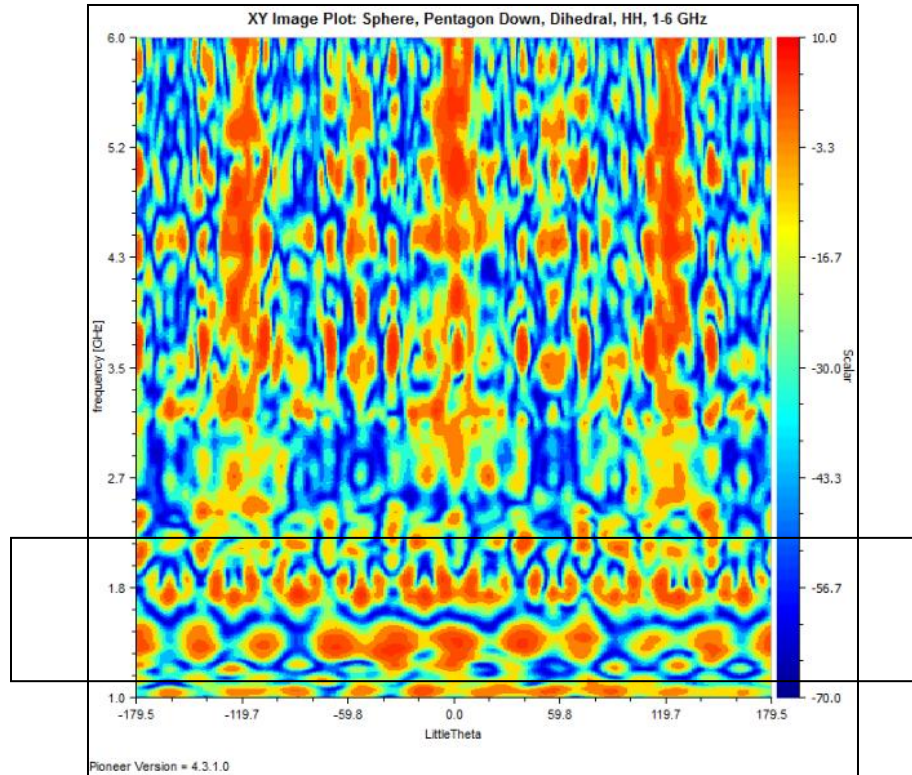
Figure 34: Sphere w/Dihedral, Pentagon Down, HH

Figure 34 illustrates that with horizontal polarization there is a more consistent backscatter response occurring within the frequency band of interest, as indicated by the black box overlaid on the plot.
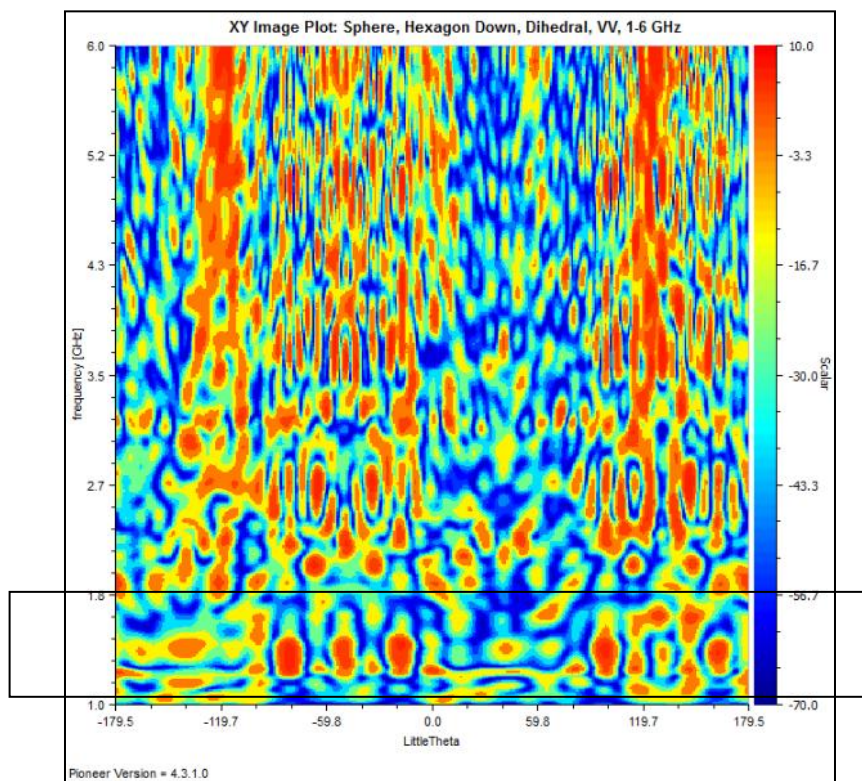
Figure 35: Sphere w/Dihedral, Hexagon Down, VV
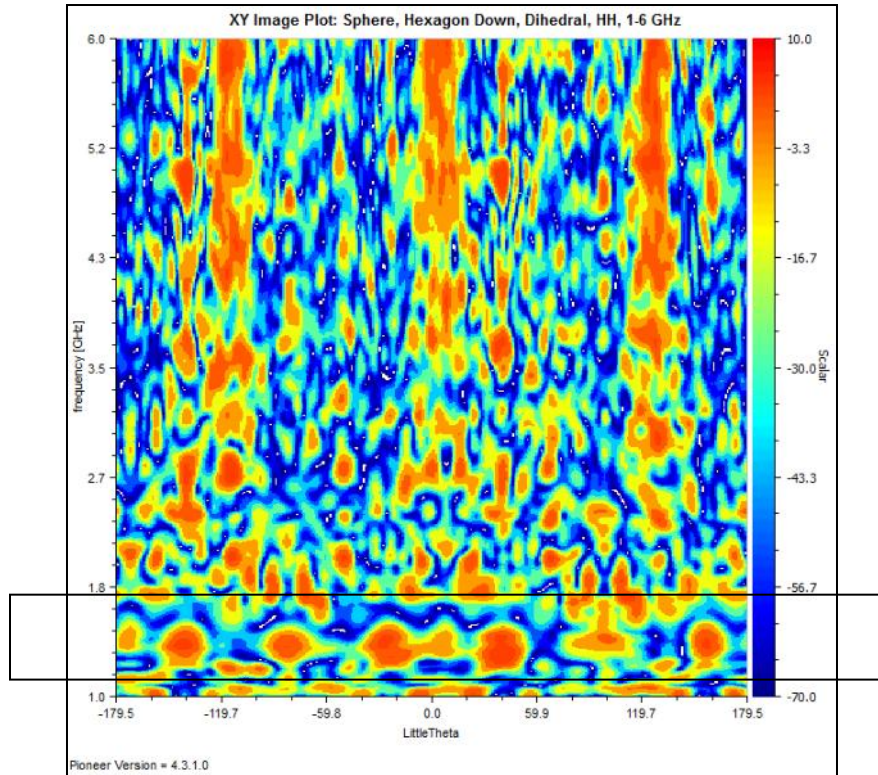
Figure 36: Sphere w/Dihedral, Hexagon Down, HH

It was discussed earlier that the longer wavelengths of the lower frequencies, specifically between 1.4-2.5GHz, allows for the sphere's RCS phenomenology to be the dominant scatterer. Furthermore, the 2v geodesic sphere's orientation also affects the efficacy of the sphere to act as a shield and dominant scatterer. The results indicated by the global frequency plots clearly indicate that the sphere, oriented with pentagon down, and measured with horizontal polarization produces the ideal shielding and scattering body. To validate the results, Table 6 is a summary of the main lobe RCS results of each test item configuration. The results indicate again that the sphere, oriented with the pentagon down, and measured in horizontal polarization produces the highest RCS return at -0.32 dBsm.

Table 6: Solo Test Item RCS Summary

Test Item	Pose	Pol		RCS (dBsm)		Azimuth (θ°)
Flat Plate	-	VV	HH	-8.6	-6.8	0
Dihedral	-	VV	HH	-17.6	-11.6	0
Sphere	Pd	VV	HH	-3.8	-0.32	0
Sphere	Hd	VV	HH	-8.8	-4.7	0

4.5 Modeling and Predictive Tool Analysis

For this research effort, multiple tools for modeling and prediction were used to determine which tool, or combination of tools, would work best to generate a coherent set of theoretical data. Predictive or theoretical measurements require a well developed computer model to measure. Therefore, the first step in this process is to determine the best computer modeling platform for designing geodesic spheres and then design the sphere. Once a suitable computer model is designed, it is then necessary to determine which computer software package produces theoretical results that have good agreement with the experimental results. The software platform, for modeling and prediction, that produces the best results will be tools recommended by thesis effort.

4.5.1 Computer Based Design Tool Results

Determining a computer based design tool for modeling a geodesic sphere is purely a qualitative assessment based on personal experience, ability, and knowledge. Therefore, this section will be a brief summary of the results.

Three main computer design tools were utilized to design a geodesic sphere: FreeCAD, 4nec2, and CST.

4.5.1.1 FreeCAD Modeling Results

FreeCAD offers a robust modeling platform with multiple tools to use in the design process. The most difficult issue with FreeCAD was the inability to translate it global or working coordinate system. Not being able to translate its coordinate system made it difficult to use its transformation tool. The transformation tool allows for rotation, reflection, and translation of parts, which made it difficult to align the parts together, Figure 36 and 37 illustrate the alignment issues that occurred with using FreeCAD. If the parts cannot be properly aligned in FreeCAD, FreeCAD will not mesh the completed model. The parts of the model that are not properly aligned will simply disappear, which is FreeCAD's way of telling the user something is wrong with that part of the model, when meshing is attempted.
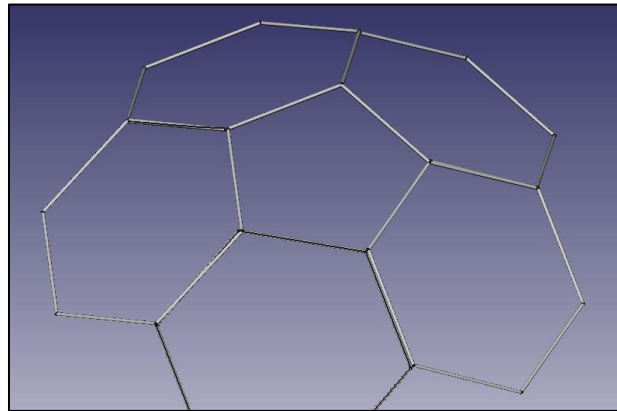
Figure 37: FreeCAD Geodesic Sphere Construction
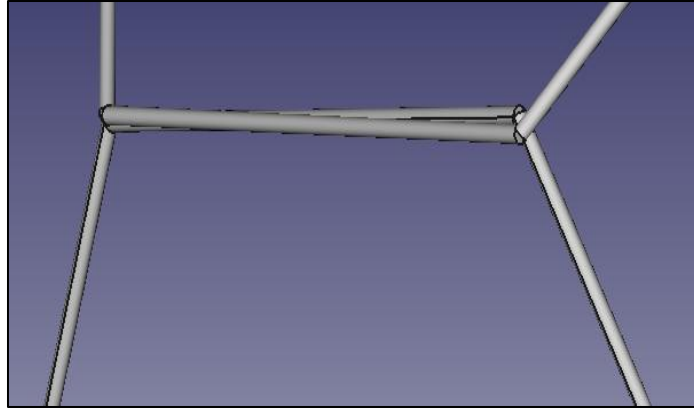
Figure 38: FreeCAD Example of Alignment Issues

4.5.1.2 4nec2 Modeling Results

4nec2 is a simulation tools that also provides a design platform for modeling. 4nec2's main issue is it does not have a way to globally manipulate a large number of parts from a model; for instance, if it is desired to change the diameter of all or some of the wires in the model, then all the wires that require the change have to be changed one-by-one. Depending on the size of the model, such as the flat rectangular grids created for the 4nec2 simulations, a single model can contain over 300 individual wires. Figure 38 is an example of a flat grid created in 4nec2. This particular model is constructed of 310 individual wires.

An attempt was also made to construct a 2v geodesic sphere, but it proved too difficult and time consuming for the same reasons as FreeCAD. The transformation tools were difficult to use and it did not possess the ability to translate its working coordinate axis, which would make it easier to manipulate parts of the model.
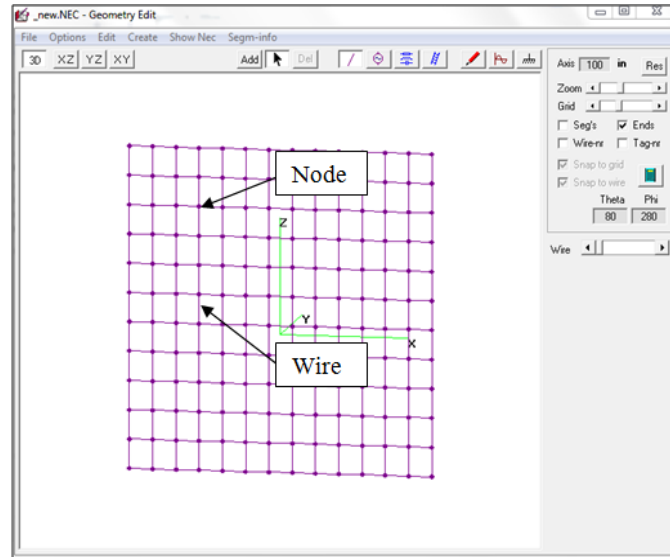
Figure 39: 4nec2 Flat-Rectangular Grid Model. Model was created to simulate the scattering behavior of the solid flat plate used in the ACR measurements.

4.5.1.3 CST Modeling Results

It is clear from Figure 39 that CST provided the superior computer aided design tool. What makes it superior is its ability to move its global coordinate system (XYZ axis or WVU axis) to any position and pose one desires. This ability gives the user the flexibility and ease to build in a three dimensional space. The other modeling programs lacked this ability making it too difficult to manipulate parts of the sphere.
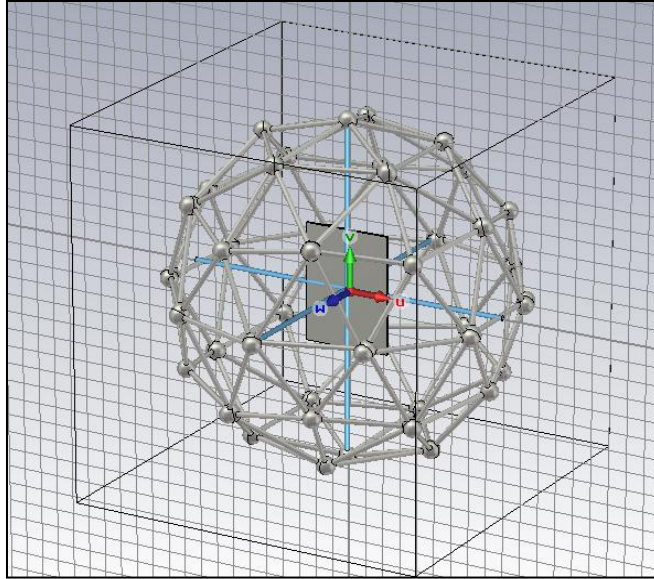
Figure 40: CST Model - Sphere w/Flat Plate, Pentagon Down

CST is the best platform for modeling a geodesic sphere cage. However, CST does not have the proper file format to export its models directly into Mercury MoM. Mercury MoM requires .geo files. Therefore, a .geo file must be created; to do so first require creating a .facet file in ACAD. Once the CST model is completed it can be exported as a .stl file into ACAD, where ACAD can then check the mesh of the object and export the model as a .facet file. The .facet file can then be formatted as a .geo file for use in Mercury MoM.

4.5.2 Predictive Analysis Tool Results

To determine which platform generates the best predictive measurements a comparison of theoretical RCS results from CST, 4nec2, and Mercury MoM were completed and then compared to experimental results obtained from the ACR. Each of the platforms will run a simulation for a flat plate of the same dimensions as the one measured by the ACR (6.5in x

4.75in). The second simulation will be conducted with the sphere (with no inner test item) and the results will be compared to that of the ACR's.

Table 7 contains the results of the different main lobe RCS values from CST, Mercury MoM, and 4nec2. The measurements were taken with horizontal polarization. The results are within ± 1 dB of the ACR measurement indicating good agreement between measured and predictive results. The ± 1 dB can be attributed back to the calibration results in chapter three, section 3.3, where the ACR calibration for horizontal polarization produced an uncertainty in RCS of ± 1 db.

Table 7: RCS Flat Plate/Grid Measurement 6GHz

Tool	RCS (dBsm)	RMSE (dBsm) vs. Pioneer
ACR Measurement (Pioneer)	2.47 [14]	N/A
CST	3.76	0.2973
Mercury MoM	3.55	0.3992
4nec2 (Grid)	3.14	N/A

Figure 40 is a graph showing the results from CST, Mercury MoM, and the ACR for the flat plate measured at 6 GHz using horizontal polarization. CST and Mercury MoM are predicted values and the ACR is the measured value. All measured data obtained from the ACR was processed in Pioneer. Main lobe RCS for CST = 3.76 dBsm, Mercury MoM = 3.55 dBsm and Pioneer = 2.47 dBsm. The main lobe RCS for 4nec2 = 3.14 dBsm. The results for 4nec2 were not included in Figure 40 for reasons that will be discussed later.
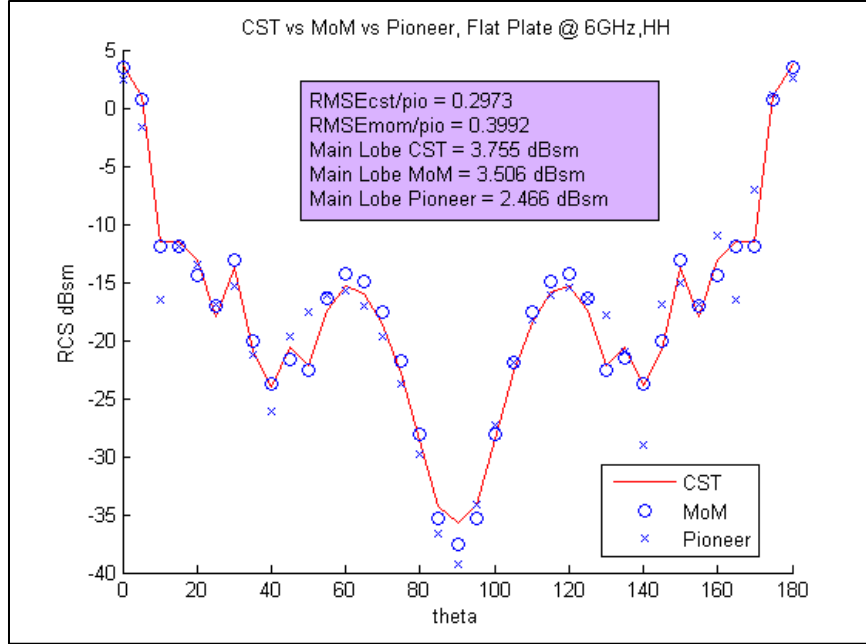
Figure 41: CST vs. MoM vs. Pioneer (measured data), Flat Plate @ 6GHz,

HH, Monostatic, Main Lobe @ 0˚ and 180˚

Utilizing Equation 17 from chapter three, the RMSE was calculated for both CST and Mercury MoM versus the measured value. The RMSE for CST = 0.2973 dBsm and for Mercury MoM = 0.3992 dBsm. To reiterate, the RMSE indicates the degree of spread of the predicted values about the mean of the measured value, which is calculated to be -19.9 dBsm. There is close agreement between the main lobe RCS of the predicted results, obtained from CST and Mercury MoM, to that of the experimental results.

To validate whether or not CST and Mercury MoM are predicting results similar to that of the experimental results, a second simulation was conducted for a flat plate at 1.4 GHz using horizontal polarization. Figure 30 shows the RCS result of a flat plate measured at 1.4 GHz. The main lobe RCS obtained from CST = -6.32 dBsm and Mercury MoM = -6.23 dBsm. The

measured main lobe RCS from Pioneer = -6.83 dBsm. There is close agreement between both prediction models and the ACR's experimental value.

RMSE was also calculated for the second experiment to determine the spread of the predicted data about the mean of the measured data, which is -17.7 dBsm. RMSE for CST = 0.4921 dBsm and for Mercury MoM = 0.6159 dBsm.
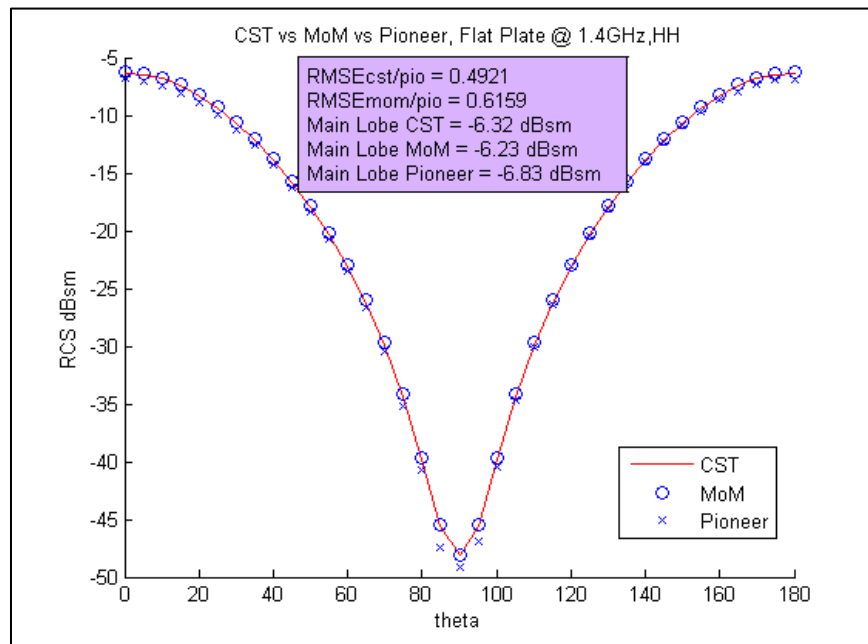
Figure 42: CST vs. MoM vs. Pioneer (measured data), Flat Plate @ 1.4GHz,

HH, Monostatic, main lobe located at 0˚ and 180˚

Figure 41 indicates good agreement of RCS results between the results of the predictive tools and experimental data, which are less than ±1 dB of the ACR's results.

4nec2 was eventually phased out as a viable modeling tool, which is the reason predicted results were not included in second simulation. For the first simulation, the main lobe RCS for the 4nec2 model resulted in a 3.14 dBsm, Table 7. Quantitatively, the 4nec2 result has good

agreement with the results of the other prediction tools and the measured result. However, from a qualitative perspective the modeling aspect was difficult and time consuming for reason already discussed.

The third simulation modeled the scattering behavior of a 2v geodesic sphere, with no test item mounted inside the sphere. In addition, the third simulation was divided into two separate simulations. The first simulation compared the results of CST and the ACR's. The second simulation compared the results of Mercury MoM and the ACR's measured results. Both simulations were carried out at a frequency of 6 GHz and horizontal polarization.

Table 8 shows the RCS results for the geodesic sphere, with no test item mounted inside, for each of the simulation platforms except 4nec2. Mercury MoM produced the best results, with only a 1.3 dBsm difference in RCS magnitude, where CST was within 2.2 dBsm of the ACR's measurement. Each simulation was executed three times, flat plate simulations included, to verify the results. Table 8 also indicates the length of time it took for each simulation to complete. Mercury MoM took 600 seconds to complete its simulation, whereas CST took 6627 seconds to complete it simulation. The reason for the large discrepancies in time is due to the fact that Mercury MoM is more ideally suited for measuring geometries such as the geodesic sphere. From a quantitative standpoint, Mercury MoM makes the most sense for the ideal tool to use for simulating theoretical measurements.

Table 8: RCS Sphere Measurement @ 6GHz

Tool	RCS (dBsm)	Time(sec)
ACR Measurement	-8.8 [14]	N/A
CST	-6.6	6627
Mercury MoM	-7.5	600
4nec4	N/A	N/A

4.6 Uncertainty Analysis

Experimentation is necessary for comparing real world work to mathematical models [18]. When comparing actual data to mathematical models it is necessary to determine how good the models fit the real world, this is where uncertainty plays an important role [18].

4.6.1 XYZ Positional Uncertainty Analysis

For this thesis, XYZ and RPY position uncertainty will be evaluated with a Monte Carlo simulation following Dr. Welsh's 5 steps [15] to determine the uncertainty bounds. The uncertainty bounds will be used to analyze statistical significance of the magnitude and phase of the sphere as it is illuminated by the EM wave.

Table 9: RMSE 1D Results for XYZ

Trials (10,000 RN)	XY ($\pm$) RMSE	Z ($\pm$) RMSE
50	0.55m	0.54m
100	0.55m	0.56m
1000	0.54m	0.54m

Table 9 indicates the calculated root mean squared error RMSE uncertainty bounds calculated for XYZ positions. Trials of 50, 100, and 1000 were conducted (with 10,000 random numbers generated for each trial). The results verify little change occurring in the RMSE based on the number of trials ran for the Monte Carlo simulation.

To determine the impact of the uncertainty in position, the results in Table 9 would be applied to the NRTF radar range model. Using trigonometry ($\tan\theta = 0.5/2590$), a change in position of 0.5 m in any direction would only result in a change in theta of only 0.0111°. Using Equation 11, the magnitude of the electric field (Equation 11) determined is then -1.0131, which results in an equivalent RCS of 0.113 dBsm, Equation 5. Therefore, it can be concluded that the positional uncertainty of ±0.5m in the XYZ plane will result in a minimal change in RCS magnitude.

To validate these results, I used Bell's uncertainty method [16], Appendix D, to calculate RMSE uncertainty for position, generating results of approximately ±1.5 m, which is only a difference of 1 m compared to the Welsh results. This change in position would only result in a new theta equal to 0.033°. Following the same steps used to calculate the RCS magnitude based on theta, the RCS is approximately 0.5 dBsm, which is only a difference of 0.4 dBsm between the two methods.
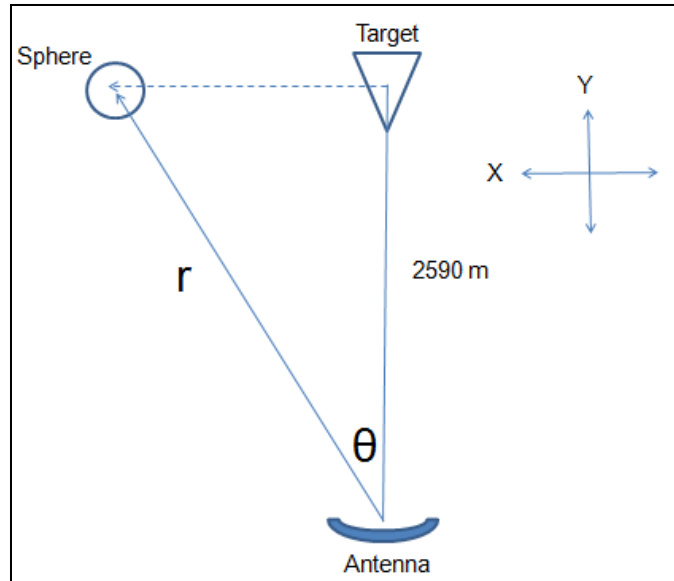
Figure 43: XYZ Representation of NRTF Radar Range

To determine if a change is position, based on the calculated RMSE, will cause a significant change in phase a point scatterer was modeled using Equation 11. The point scatterer was measured with a change in position of 1m in the Y axis and then measured again with a change in position of 2 m in the Y axis. The frequency selected was 6 GHz. Figure 44 illustrates that the change in position in the Y axis of 1(black line) to 2(red line) meters does not have a significant effect on the RCS magnitude. It also indicates that there is a change in phase on the EM wave, which is expected as the object or point scatterer moves forward or backward along the Y axis.
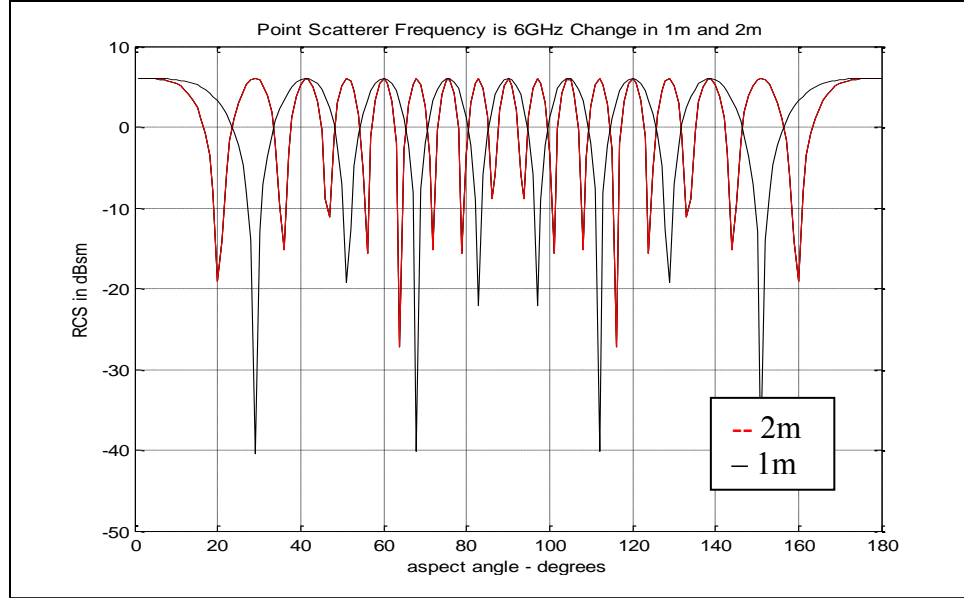
Figure 44: RCS Magnitude and Phase as a Result of a Change in Y Position

4.6.2 RPY Axial Uncertainty Analysis

Table 4 indicates an RMSE of 0°, 0°, and 3° for roll, pitch and yaw respectively. Based on these values, there would minimal to no impact on RCS magnitude and phase. However, combining the results from Table 4 with those calculated using Bell's method, Appendix D, gives an RMSE of $\pm 4^o$ for roll and pitch, and $\pm 23^o$ for yaw.

To determine the impact of a 4° pitch on RCS magnitude, the geodesic sphere was rotated forward on its Y axis in 4° increments, until 36° was reached, which is close to the maximum pitch angle of 35° for the DJI Phantom II, Table 3. Then the RCS response of sphere was taken at each of the 4° increments and plotted. Figure 45 illustrates that there is minimal impact to the RCS magnitude of the sphere as pitch angle is changed. Figure 46 is a polar plot of the RCS response which further shows very little variation in RCS magnitude over each of the incremental changes in pitch.

74
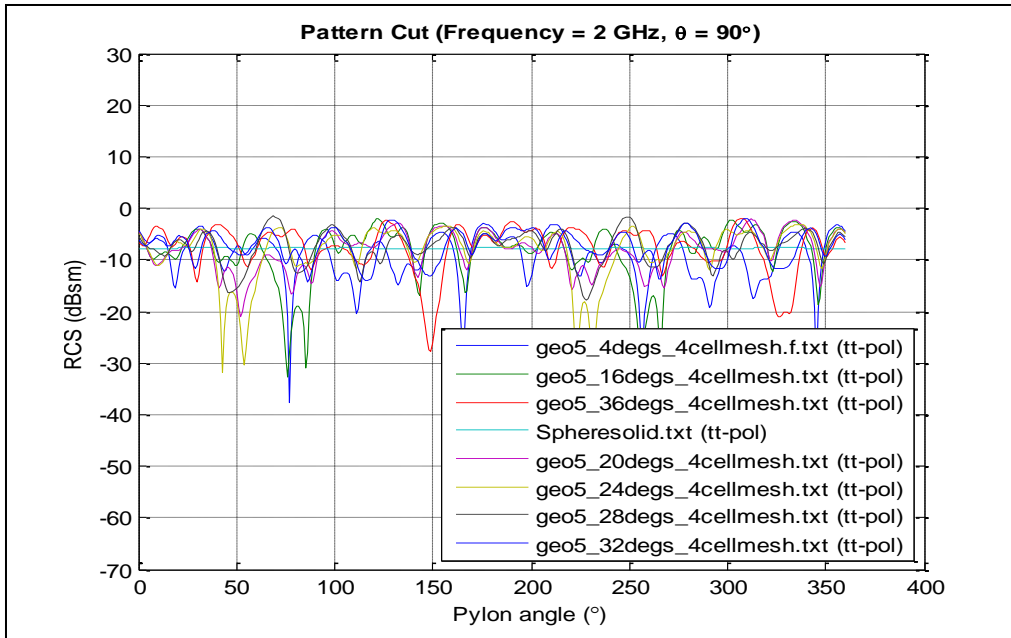
Figure 45: RCS Magnitude vs. Pitch Angle
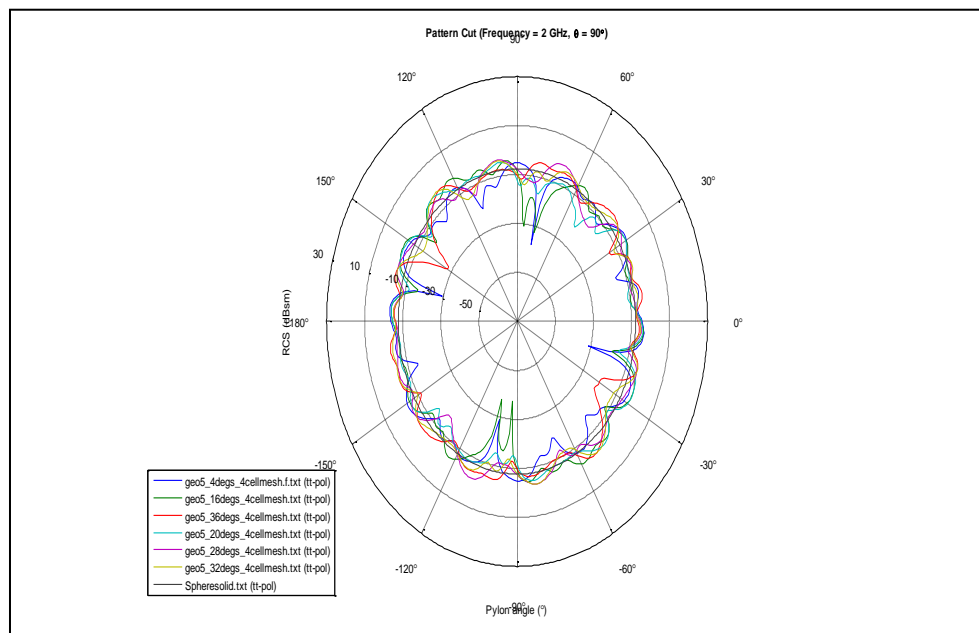
Figure 46: Polar Plot RCS Magnitude vs. Pitch Angle

75

4.6.3 Sector Analysis

Sector statistics were compiled for all the test item configurations. However, only the sector statistics for the sphere, with flat plate mounted in the center, pentagon down, and measured with horizontal polarization were included and can be found in Appendix E. The sectors were created with a 5° window. The window slide was 2° which created 180 sectors. For each sector the expected value and median of the RCS were calculated. Based on the uncertainty bounds calculated earlier for XYZ the RMSE = ± 0.5m, the sphere's aspect angle would change by $\pm 0.0111^{0}$, which according to Table 10 will result in minimal magnitude error. For example, sector 91 possesses a mean RCS of -3.28092 dBsm. An RMSE of 0.5 m would give a bias error of approximately -2.7 or -3.7 dBsm, which is minimal.

Table 10: Abbreviated Sector Statistics Summary, SFpPdHH, Appendix D

Sector ($^{\circ}$)	Frequency	Max RCS (dB)	Mean RCS (arithmetic)	Median RCS (dB)	Std Dev RCS (db)
91 (-0.5 - -5.5)	1- 1.5	-1.06384	-3.28093	-3.41728	-
92 (-2.5 - -7.5)	1-1.5	-1.06384	-3.5424	-3.4656	-
93 (-4.5 - -9.5)	1-1.5	-1.13859	-3.98412	-3.83859	-

4.7 Investigative Questions Answered

The following investigative questions were asked at the beginning of chapter 1 and answered by this thesis:

1. Can the geodesic sphere shield the RCS mechanisms of the quad-rotor?

2. Is there a commercially available tool that can properly predict the RCS of the geodesic sphere?

3. Will positional and axial uncertainties caused by the DGPS system and quad-rotor IMU affect the RCS magnitude and phase measurements taken by the radar?

4.8 Summary

The 2v geodesic sphere proved to be sufficient at shielding the RCS of an internal object. It showed that an ideal frequency band of approximately 1.4-2.5 GHz internal objects were nearly invisible to the radar. More importantly, this frequency band demonstrated that the geodesic sphere can behave as a two-way field probe without interference from the internal object. The ideal frequency for obtaining maximum RCS from sphere, while shielding the internal object, is approximately at 1.4 GHz. A frequency of 2.5 GHz would be the maximum allowable frequency before the internal objects began displaying their unique RCS.

This thesis clearly showed that Mercury MoM, in combination with MATLAB's ALPINE for data processing and CST (and ACAD for file format changes) for modeling provides sufficient tools for modeling and prediction analysis. CST provided good prediction results (generally within 1dBsm of the experimental data); however the time to complete a simulation was approximately 1000 times greater than that of Mercury MoM, Table 8.

Uncertainty analysis revealed that the quad-rotor and DGPS uncertainties will produce errors in position; however, those errors will have little effect on the magnitude and phase of the sphere's RCS. RPY effects on showed that pitch and roll errors would also have little effect on RCS magnitude.

V. Conclusions and Recommendations

5.1 Chapter Overview

This section details the conclusions that can be made from the results and analysis of this research. Additionally, future related follow-on research to this effort is presented.

5.2 Conclusions of Research

Unique to this research was the investigation of the RCS characterization of a 2v geodesic sphere. The results of this research indicate that an electrically conducting geodesic sphere can provide a suitable barrier between the radar antenna and the RCS phenomenology of an internal structure. More importantly, this research indicated that the sphere can behave as a two-way probe while shielding the internal object. The optimal frequency band to realize the two-way probe concept was determined to be between 1.4-2.5 GHz.

Another facet of this research was developing a suitable predictive and modeling tool for future research. It was shown that for the unique geometry of the geodesic sphere, Mercury MoM is best suited to simulate experiments, used in combination with ALPINE for data processing. For modeling, the recommendation of this thesis is to use CST's microwave studio. CST is by far the easiest tool for modeling complex geometries such as the geodesic sphere.

This research also involved the investigation of the positional uncertainties associated with the DGPS used to track the quad-rotor's position in the XYZ plane and the IMU used to control roll, pitch and yaw which are related to the axial uncertainties associated of the quad-rotor. In regards to the positional uncertainty, this research showed that the angular error related to XYZ displacement is minimal and would have little impact on surveying the test volume or quiet zone. In regards to axial uncertainties, changes along the P (pitch) axial lines of the quad-

rotor will have a minimal impact on MP error. However, this thesis was not able to determine quantitatively the impact that roll or yaw would have on MP errors.

5.3 Significance of Research

The significance of this research indicates that the proof of concept of a two-way field probe, utilizing a geodesic sphere and quad-rotor is a real possibility. A quality predictive tool was established and should prove to be a viable option for future research. Uncertainty analysis showed there to be minimal effect of producing significant MP error in the XYZ axis; however, a deeper investigation needs to be accomplished for uncertainties associated with RPY.

5.4 Recommendations for Action

Recommendations for future action will involve integrating a quad-rotor with the geodesic sphere. The integration of the two is paramount to future testing. Another area of focus should be made in helping to alleviate flight restrictions at Wright Patterson AFB, OH. The ability to conduct outdoor experiments will help in any future research endeavor.

5.5 Recommendations for Future Research

As previously stated, integration of the sphere and quad-rotor is paramount to future research. Geodesic spheres can be constructed with varying frequency of strut support. For this research, a 2v strut design was used to construct the sphere. However, geodesic spheres can be designed with higher frequencies than 2v so more research into multiple frequency geodesic spheres and their efficacy as a RCS shield and two-way probe needs to be researched. With this in mind, future research should include a trade-off study in how frequency design affects airlift. However, it is logical to assume that a higher frequency strut design will affect the airlift of the quad-rotor. Thus a balance between strut design, RCS reduction, and airlift needs to be

investigated. A study in strut design should also include strut diameter and material and their affect on RCS reduction and airlift.

Another area for future work is a drift analysis of the quad-rotor DGPS and IMU. Research in this area will help to better understand the uncertainty errors associated with both systems.

5.6 Summary

A spherical cage of geodesic design is a frequency dependent structure that provides adequate RCS shielding of an internal object from a radar antenna. It also will allow the sphere to act as a two-way field probe using its own magnitude and phase illumination to provide structure to the EM wave incident on the sphere, which will allow for characterization and understanding of the EM wave traversing the test volume. Mercury MoM proved to an adequate prediction tool for future research endeavors. Further research into the statistical analysis of the sphere is needed for a better understanding of the magnitude and phase errors that will occur with this probe concept. A minimal analysis was conducted with this research, which indicates that there will be minimal magnitude and phase errors, but a robust study needs to be done.

Appendix A

This appendix contains the measurement log for the RCS measurements taken by the engineers at the ACR [14].

Unclassified

AFRL/RY

Advanced Compact Range

Measurement Log

Customer:	Travis AFIT	2 - 18Ghz Band Information		0.5 - 6Ghz Band Information		26.5 - 40Ghz Band Information	
Project:	AFIT Sphere	Freq Increment:		Freq Increment:	10MHz	Freq Increment:	
Classification:	Unclassified	Feed Antenna:		Feed Antenna:	H-1734	Feed Antenna:	
Target:	AFIT Sphere	Polarization:		Polarization:	VV/HH	Polarization:	
Test Body/Mount:	Foam Columns	Tx Pulse:		Tx Pulse:	15	Tx Pulse:	
Pylon Tip:	6000 lb. Kneeling	Rx Gate:		Rx Gate:	20	Rx Gate:	
Data Folder:	X:\14302_Travis_AFIT\Data	PRI:		PRI:	1000nS	PRI:	
		Transmit Atten:		Transmit Atten:	0	Transmit Atten:	
Radar Operator:	Tom/Shawn	Receive Atten:		Receive Atten:	0	Receive Atten:	
		Phase Code:		Phase Code:	Lintek	Phase Code:	
Comments/Notes:		Integrations:		Integrations:	4096	Integrations:	
		VV Calibration Filename:		Calibration Filename:		Calibration Filename:	
		HH Calibration Filename:		Calibration Filename:		Calibration Filename:	
		Calibration Device:		Calibration Device:	15" Cylinder	Calibration Device:	

Date MM/DD/YYYY	Julian Date	Data Filename	Type	Pol	Frequency Band	Azimuth Increment	Elevation	Description
10/29/2014	14302	AFIT_TARGET_14302_01	TAR	VV	2 to 18/0.01	-30 to 30/1.0	0	Preliminary First Test Article shot. Sitting on Pentagon
10/29/2014	14302	AFIT_TARGET-DIHEDRAL_14302_01	TAR	VV	2 to 18/0.01	-30 to 30/0.5	0	Preliminary First Test Article + dihedral shot. Sitting on Pentagon
10/29/2014	14302	1800CYL_14302_01.cal	CAL	VV	0.5 to 6/0.01	0	0	18" cylinder on 21" foam column
10/29/2014	14302	1800CYL_14302_02.cal	CAL	VV	0.5 to 6/0.01	0	0	18" cylinder on 21" foam column
10/29/2014	14302	1800CYL_14302_01.cbk	CBK	VV	0.5 to 6/0.01	0	0	18" cylinder background
10/29/2014	14302	1800CYL_14302_02.cbk	CBK	VV	0.5 to 6/0.01	0	0	18" cylinder background
10/29/2014	14302	1500CYL_14302_01.bkg	BKG	VV	0.5 to 6/0.01	0	0	15" cylinder background
10/29/2014	14302	1500CYL_14302_02.bkg	BKG	VV	0.5 to 6/0.01	0	0	15" cylinder background
10/29/2014	14302	1500CYL_14302_01.tar	TAR	VV	0.5 to 6/0.01	0	0	15" cylinder on 21" foam column
10/29/2014	14302	1500CYL_14302_02.tar	TAR	VV	0.5 to 6/0.01	0	0	15" cylinder on 21" foam column
10/30/2014	14303	A1_MF_VV_14303_01.tar	TAR	VV	0.5 to 6/0.01	-180 to 180/1.0	0	Sphere (solo) with internal foam mount on 21" foam column. Pentagon down.
10/30/2014	14303	B1_MF_VV_14303_01.tar	TAR	VV	0.5 to 6/0.01	-180 to 180/1.0	0	Sphere, pentagon down. Dihedral on internal foam mount.
10/30/2014	14303	C1_MF_VV_14303_01.tar	TAR	VV	0.5 to 6/0.01	-180 to 180/1.0	0	Sphere, pentagon down. Flat plate on internal foam mount. Length along vertical axis.
10/30/2014	14303	A2_MF_VV_14303_01.tar	TAR	VV	0.5 to 6/0.01	-180 to 180/1.0	0	Sphere (solo) with internal foam mount on 21" foam column. Hexagon down.
10/30/2014	14303	B2_MF_VV_14303_01.tar	TAR	VV	0.5 to 6/0.01	-180 to 180/1.0	0	Sphere, hexagon down. Dihedral on internal foam mount.
10/30/2014	14303	C2_MF_VV_14303_01.tar	TAR	VV	0.5 to 6/0.01	-180 to 180/1.0	0	Sphere, hexagon down. Flat plate on internal foam mount. Length along vertical axis.
10/30/2014	14303	D_MF_VV_14303_01.tar	TAR	VV	0.5 to 6/0.01	-180 to 180/1.0	0	Dihedral on foam mount, no sphere.
10/30/2014	14303	E_MF_VV_14303_01.tar	TAR	VV	0.5 to 6/0.01	-180 to 180/1.0	0	Flat plate on foam mount, no sphere. Length along vertical axis.
10/30/2014	14303	F_MF_VV_14304_01.tar	TAR	VV	0.5 to 6/0.01	-180 to 180/1.0	0	Solo foam pedistal. Background to Dihedral and flat plate.
10/31/2014	14304	1800CYL_14304_01.cal	CAL	HH	0.5 to 6/0.01	0	0	18" cylinder on 21" foam column
10/31/2014	14304	1800CYL_14304_02.cal	CAL	HH	0.5 to 6/0.01	0	0	18" cylinder on 21" foam column
10/31/2014	14304	1800CYL_14304_01.cbk	CBK	HH	0.5 to 6/0.01	0	0	18" cylinder background
10/31/2014	14304	1800CYL_14304_02.cbk	CBK	HH	0.5 to 6/0.01	0	0	18" cylinder background
10/31/2014	14304	1500CYL_14304_01.bkg	BKG	HH	0.5 to 6/0.01	0	0	15" cylinder background
10/31/2014	14304	1500CYL_14304_02.bkg	BKG	HH	0.5 to 6/0.01	0	0	15" cylinder background
10/31/2014	14304	1500CYL_14304_01.tar	TAR	HH	0.5 to 6/0.01	0	0	15" cylinder on 21" foam column
10/31/2014	14304	1500CYL_14304_02.tar	TAR	HH	0.5 to 6/0.01	0	0	15" cylinder on 21" foam column
10/31/2014	14304	D_MF_HH_14304_01.tar	TAR	HH	0.5 to 6/0.01	-180 to 180/1.0	0	Dihedral on foam mount, no sphere.
10/31/2014	14304	E_MF_HH_14304_01.tar	TAR	HH	0.5 to 6/0.01	-180 to 180/1.0	0	Flat plate on foam mount, no sphere. Length along vertical axis.
10/31/2014	14304	F_MF_HH_14304_01.tar	TAR	HH	0.5 to 6/0.01	-180 to 180/1.0	0	Solo foam pedistal. Background to Dihedral and flat plate.
10/31/2014	14304	A1_MF_HH_14303_01.tar	TAR	HH	0.5 to 6/0.01	-180 to 180/1.0	0	Sphere (solo) with internal foam mount on 21" foam column. Pentagon down.
10/31/2014	14304	B1_MF_HH_14303_01.tar	TAR	HH	0.5 to 6/0.01	-180 to 180/1.0	0	Sphere, pentagon down. Dihedral on internal foam mount.
10/31/2014	14304	C1_MF_HH_14303_01.tar	TAR	HH	0.5 to 6/0.01	-180 to 180/1.0	0	Sphere, pentagon down. Flat plate on internal foam mount. Length along vertical axis.
10/31/2014	14304	A2_MF_HH_14303_01.tar	TAR	HH	0.5 to 6/0.01	-180 to 180/1.0	0	Sphere (solo) with internal foam mount on 21" foam column. Hexagon down.
10/31/2014	14304	B2_MF_HH_14303_01.tar	TAR	HH	0.5 to 6/0.01	-180 to 180/1.0	0	Sphere, hexagon down. Dihedral on internal foam mount.
10/31/2014	14304	C2_MF_HH_14303_01.tar	TAR	HH	0.5 to 6/0.01	-180 to 180/1.0	0	Sphere, hexagon down. Flat plate on internal foam mount. Length along vertical axis.

Unclassified

Figure A.1: ACR Measurement Log

Appendix B

Appendix B contains the results from the calibration and background subtractions conducted by the engineers at the ACR [14]. Figures B.1, B.2, B.3, B.4, and B.5 depict the results of the calibration.
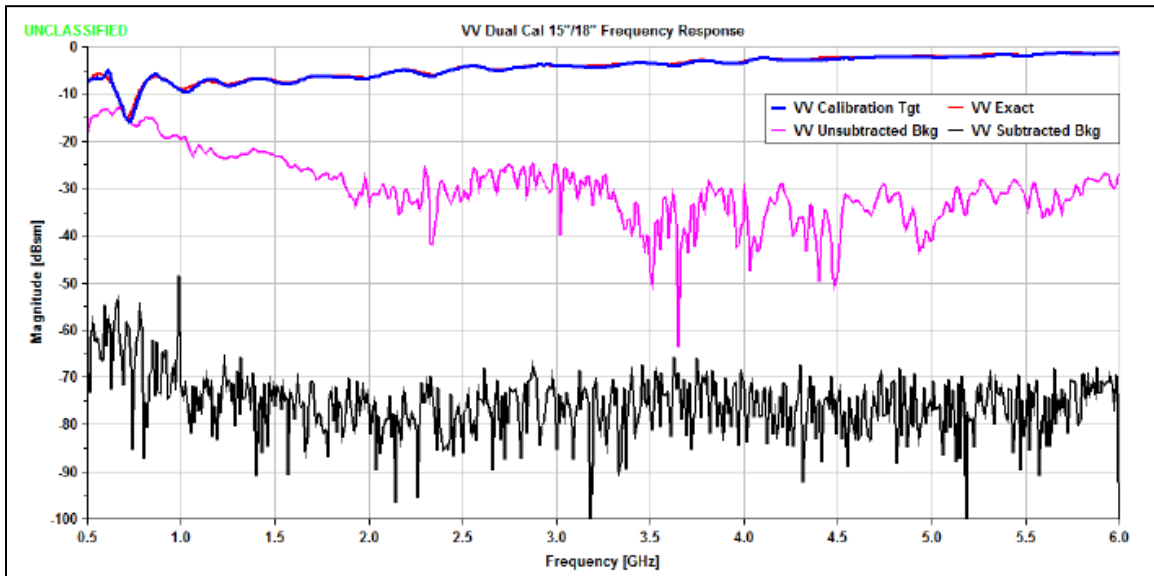
Figure B.1: VV Dual Calibration Results
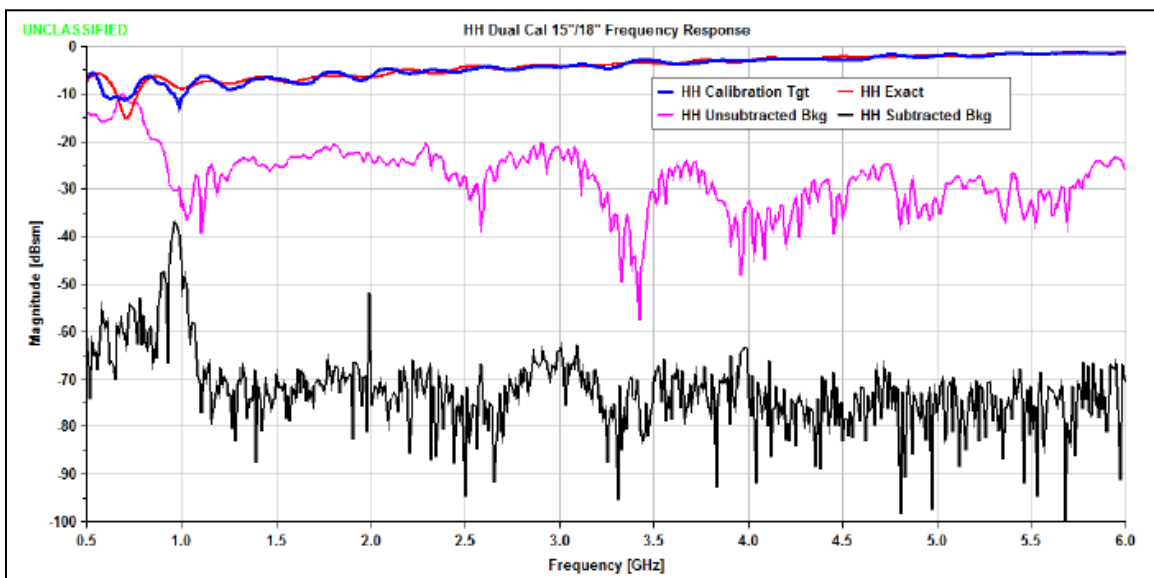
Figure B.2: HH Dual Calibration Results
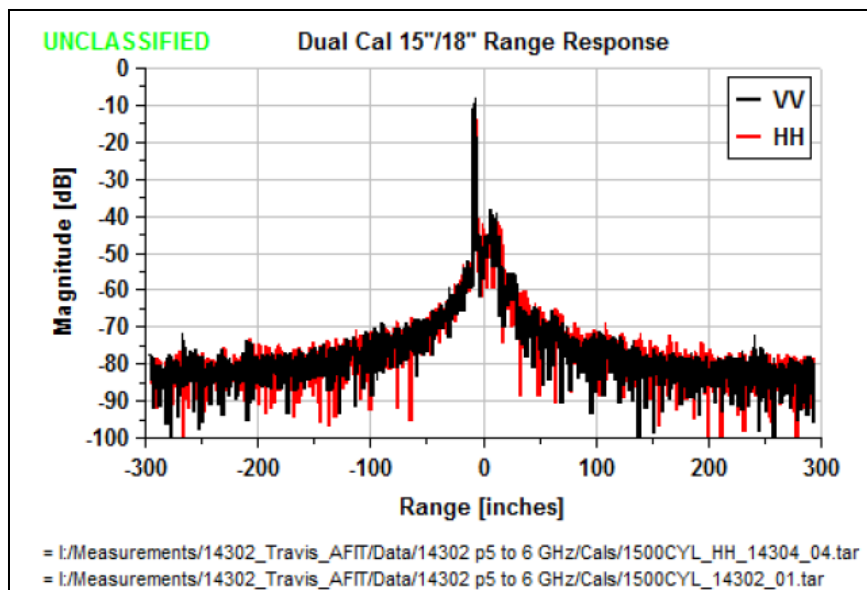
Figure B.3: Dual Calibration 15"/18" Range Response
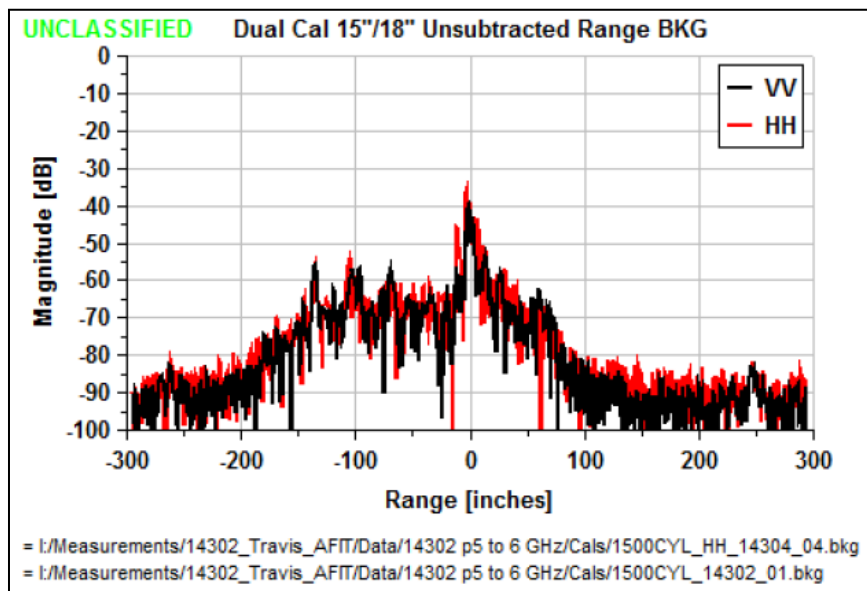
Figure B.4: Dual Calibration 15"/18" Range Response
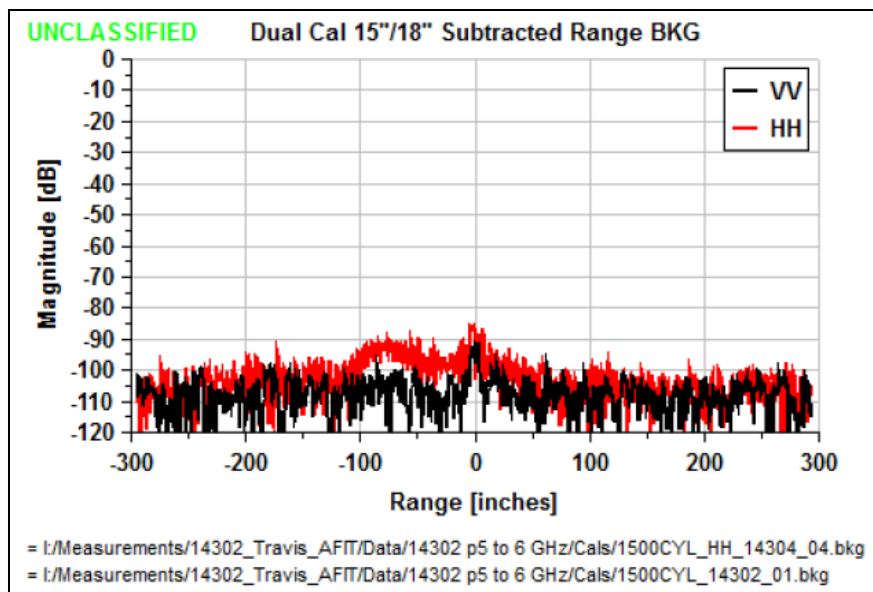
Figure B.5: Dual Calibration 15"/18" Subtracted BKG [13]

Appendix C

Appendix C contains the results from the ACR report [14]. ACR data was processed in Pioneer. Figure C.1, C.2, C.3, C.4, and C.5 are global frequency plots of the experimental measurements obtained from the ACR.
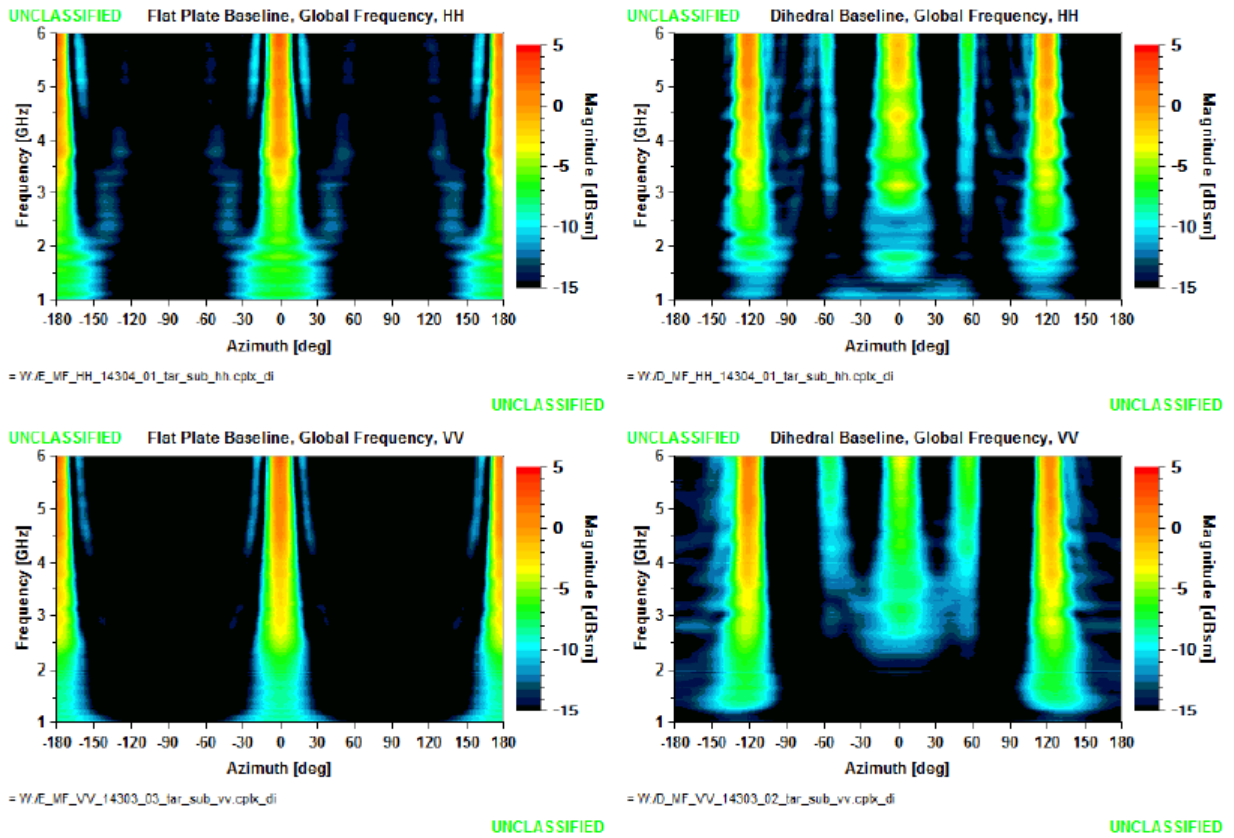
Figure C1: GFP Flat Plate and Dihedral Baseline Results
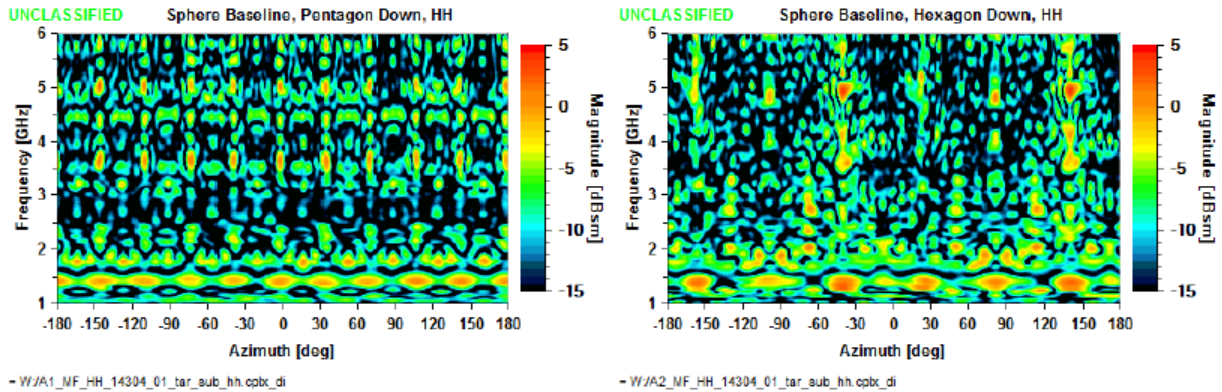
Figure C2: GFP Sphere Baseline Results, HH
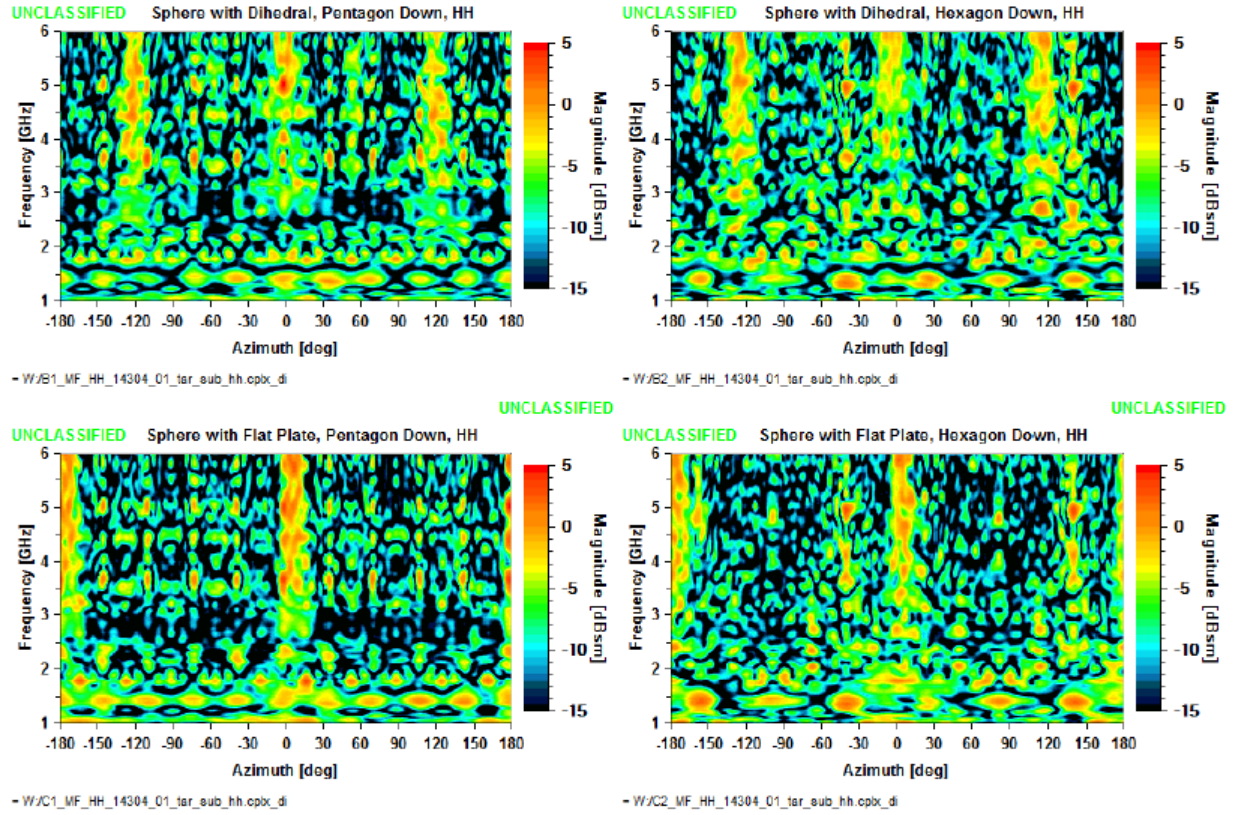
Figure C3: GFP Sphere with Flat Plate & Dihedral, HH
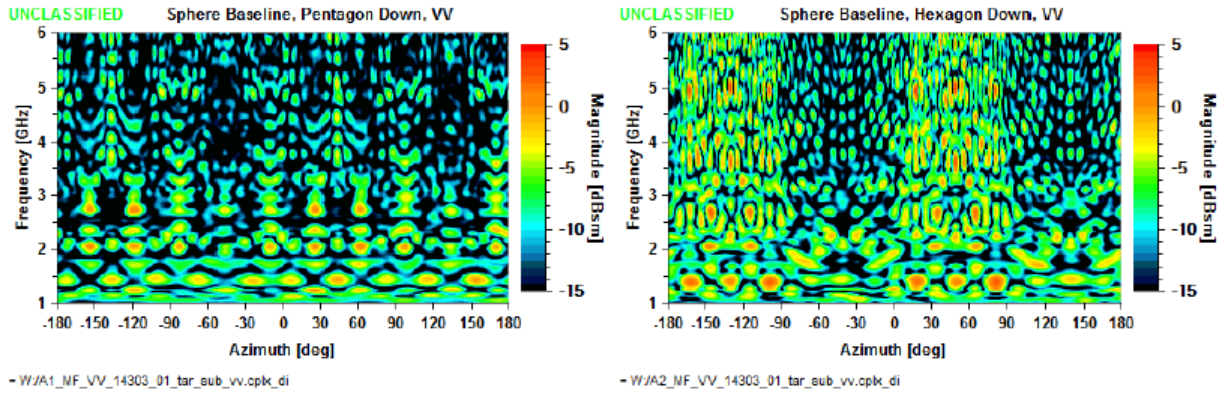
Figure C4: GFP Sphere Baseline Results, VV
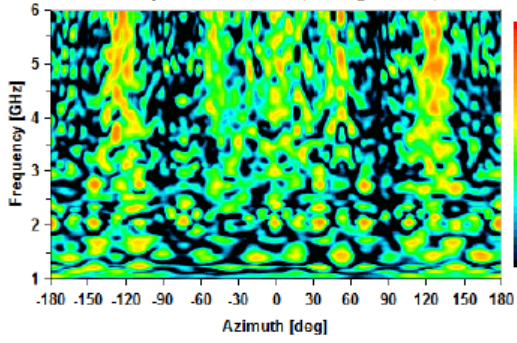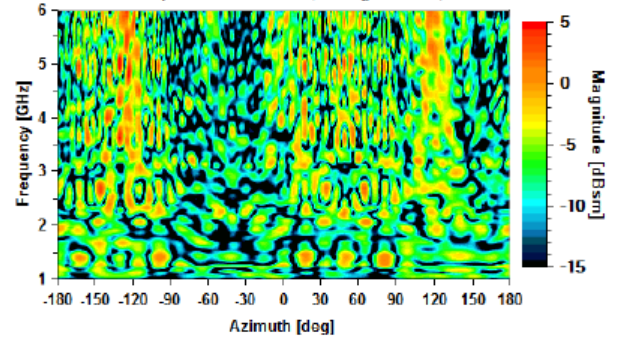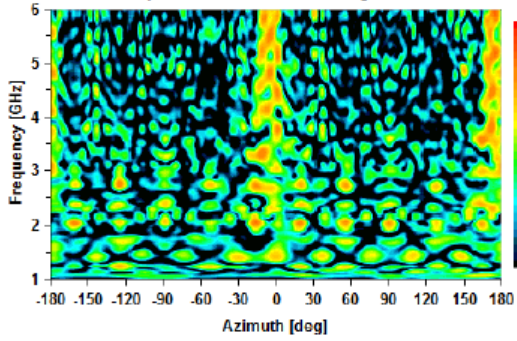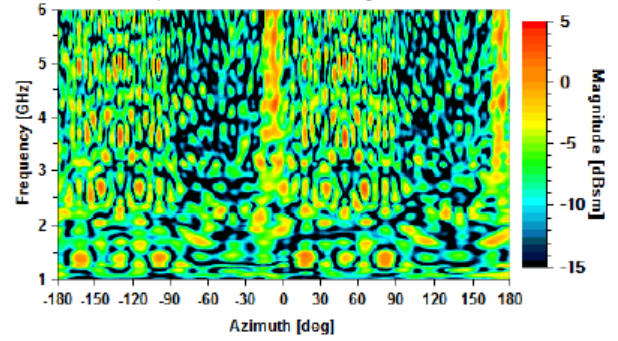
Figure C5: GFP Sphere w/Flat Plate & Dihedral, VV

Appendix D

Appendix D contains the uncertainty analysis method as prescribed by Stephanie Bell, Table D.1, [16]. This method was used as an alternative to Dr. Welsh's method. However, Dr. Welsh's method is the primary method used. Bell's method will act as validation tool for results obtained through Dr. Welsh.

According to Table 3, the horizontal accuracy for the DJI Phantom II is given as 2.5m. Horizontal is defined as in the X and Y direction in terms of the horizontal plane to the earth. Z direction is defined as the elevation to the horizon, or the up and down direction. However, for this uncertainty analysis the uncertainty for standard DGPS is 5 meters in either the X or Y direction. This uncertainty represents the worst case scenario and will be the value used to conduct the analysis.

Table D.1 shows the results from the uncertainty analysis conducted for the XYZ positional uncertainty. Once the XYZ uncertainties were established, the uncertainty for position and theta were calculated.

The first step in the uncertainty analysis was to identify possible components or causes of uncertainty. From Table D.1, the first uncertainty was identified to be the uncertainty in the measurements taken (U_m). The level of uncertainty was calculated to be 0.28m and was calculated from the following Equation D.1, [16]. The measurement uncertainty, U_m, is assumed to be a uniform distribution, which is the origin for the divisor$\sqrt{3}$, which means that this error is equally likely to locate in a uniform distribution [16].

Table D.1: Uncertainty in XYZ, Position (r), & Theta (θ)

Source of Uncertainty	Value ±	PDF	Divisor	Standard U_x	Standard U_y	Standard U_z	Standard U_r	Standard U_θ
U_m	.28m	U	$\sqrt{3}$	0.288	0.288	0.288	0.288	0.288
U_{est}	2.5m	U	$\sqrt{3}$	0.721	0.721	0.721	0.721	0.721
U_σ N = 100	0.2m	N	1	0.201	0.224	0.126	0.037	0.000756
Combined Standard Uncertainty		N		0.803	0.808	0.787	0.778	0.777
Expanded Uncertainty		N (k=2)		1.606	1.617	1.575	0.155	1.554

$$U_m = \frac{0.5}{\sqrt{3}} \qquad (D.1)$$

The second component of uncertainty is based on the manufacturer's stated uncertainties in Table 3 for the DJI Phantom II. The assumption made is that DJI underestimated their positional uncertainties. DJI's stated claims of accuracy from Table 3 are twice as good as the standard DGPS value of 5m from Table 2. Thus, Equation D.2 from Bell's method [16] was used to determine this value. A uniform distribution was assumed and the value calculated is 0.721m. Although in Table 4 it was expressed that the uncertainty associated with Z = 0.8m, for simplicity, it was assumed that the manufacture underestimated by the same margins as in the XY directions (5m).

$$U_{est} = \frac{0.5 * 2.5}{\sqrt{3}} \qquad (D.2)$$

The next uncertainty determined is called the *standard of the mean uncertainty for N readings*. The Monte Carlo used for this analysis took 100 readings for each of the six degrees of freedom. Where N = 100, σ = standard deviation, and assuming a normal distribution, Equation D.3 was used to determine the value for this uncertainty [16].

$$U_\sigma = \frac{\sigma}{\sqrt{N}} \tag{D.3}$$

Once all the uncertainties were determined, it was necessary to find the magnitude of their *combined* uncertainty. Assuming Normal distribution for this uncertainty, Equation D.4 was used to calculate this uncertainty [16].

$$U_{combined} = \sqrt{U_m{}^2 + U_{est}{}^2 + U_\sigma^2} \tag{D.4}$$

The final step is to scale the uncertainty according to the level of confidence that is desired, in this case 95%, and based on the distribution assumed, in this case a normal distribution. This type of uncertainty is called *expanded uncertainty* and uses a method called *coverage factor*, which is determined by taking the combined uncertainty and scaling it by the coverage factor, which is k = 2 for a desired 95% confidence [16]. For a normal distribution there are three other coverage factors (k = 1 ≈68%, k = 2.58 ≈ 99%, and k = 3 ≈99.7%) [16]. Equation D.5 was used to calculate the expanded uncertainty.

$$U_{expanded} = U_{conbined} * k \tag{D.5}$$

The expanded uncertainty is the uncertainty that exists in the random variable. For instance, in Table D.1, the expanded uncertainty for X = ±1.606m, meaning that for any given position of X, there will be an uncertainty bound of ±1.606m in either the X or Y directions.

Table D.2 contains uncertainty analysis conducted for RPY. The same methods used for developing the uncertainties for XYZ were also used for developing the uncertainties for RPY. However, for uncertainty in measurement, U_m, a value of 0.5° was used. And for uncertainty of estimate, U_{est}, a value of 3.5° was used.

Furthermore, it is assumed that any magnitude and phase errors associated with RPY uncertainty, is independent of uncertainties in XYZ and vice versa.

Table D.2: Uncertainty in Roll, Pitch, & Yaw (RPY)

Source of Uncertainty	Value ±	PDF	Divisor	Standard U_p	Standard U_r	Standard U_y
U_m	0.28°	U	$\sqrt{3}$	0.288	0.288	0.288
U_{est}	3.5°	U	$\sqrt{3}$	2.02	2.02	11.55
U_σ N = 100	0.2°	N	1	0.947	0.627	5.882
Combined Standard Uncertainty		N		2.250	2.135	12.962
Expanded Uncertainty		N (k=2)		4.500	4.271	25.924

The XYZ positional uncertainties are very small in magnitude especially when taken into the context of the NRTF range. At 2590m [3], Figure D.1, a change in position, XY or Z, of less than 2m will only result in a small change in theta of ≈1.5°, Table D.1. Basic trigonometry is used to calculate theta.
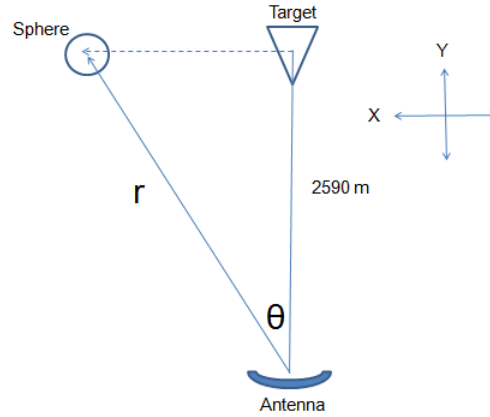
Figure D.1: XYZ NRTF Range Model

To determine the effect that a change in theta of $\approx \pm 1.5°$ has on the magnitude of RCS, three test configurations were randomly chosen from the measurements conducted by the ACR. The three test configurations randomly chosen were SSHdHH = Solo Sphere/Hexagon Down/HH, SSPdHH = Solo Sphere/Pentagon Down/HH, SFpPdVV = Sphere/Flat Plate/Pentagon Down/VV. The measurement frequency chosen observe the RCS at was 1.4GHz. The ACR measurements were taken between -179.5˚ to 179.5˚ at 1˚ increments so instead of looking at theta $\approx \pm 1.5°$, a theta $\approx \pm 2°$ will be evaluated, which will effectively increase the margin of error in the RCS magnitude.

Five random samples were chosen from each of the test configurations, for a total of 15 samples. Each sample consisted of three individual measurands within 2˚ of each other. The five samples were randomly chosen to be -179.5˚ to -177.5, -151.5˚ to -149.5˚, -102.5˚ to -100.5˚, -69.5˚ to -67.5˚, -28.5˚ to -26.5, and 0.5054˚ to 2.5054˚. Their corresponding RCS values at 1.4GHz were taken from the ACR measurements, and then the average difference in RCS was determined for each of the five samples, for each test configuration. Then a total average RCS was calculated for each test configuration. The average change in RCS, based on a theta $\approx \pm 2°$,

is as follows: SSHdHH ≈ 0.509 dBsm, SSPdHH ≈ 0.252 dBsm, and SFpPdVV ≈ 0.093 dBsm. It is apparent from these results that a theta ≈ ±2° produces a minimum change in RCS < 1 dBsm. Therefore, a positional uncertainty of less than 2m in the X, Y, or Z directions will result in a non-impactful change in RCS magnitude. Table D.3, in Appendix D, shows the complete results of this analysis.

Table D.2 shows the uncertainty bounds associated with RPY. For roll and pitch, it appears at approximately ±4˚ in angle can be expected with 95% confidence. A 4˚ change in angle will have minimal impact on the magnitude and phase of the sphere's RCS. The yaw, or rotational uncertainty, shows a ±25˚ uncertainty. It must be remembered that yaw is generally knows to be a rate of rotation about the z-axis of the quad-rotor. So if the quad-rotor and sphere are set to rotate at a desired rate, assuming there is no roll or pitch, it can be assumed that the sphere will present a consistent face to the radar; therefore there should not be a MP effect caused by yaw.

To generate pseudo-random measurements, a normal distribution was assumed for the random number generator. 100 random numbers were generated for each RV. Then, following Welsh's steps the mean and standard deviations were calculated for these random numbers. Once the mean and standard deviations were calculated, the process was repeated again. A total of three trials were run for each component. The means and standard deviations for all three trials for each component random variable were then used to develop the uncertainty bounds recorded in Tables D.1 and D.2, Bell's method of uncertainty analysis was followed [16].

Table D.3 contains the measured RCS values for a specified theta value, at 1.4 GHz. The measurements were obtained from three different test configurations as indicated: SSHdHH =

Solo Sphere/Hexagon Down/HH, SSPdHH = Solo Sphere/Pentagon Down/HH, SFpPdVV = Sphere/Flat Plate/Pentagon Down/VV.

Table D.3: RCS Values for $\Delta\theta = \pm2°$

Theta/1.4GHz	SSHdHH RCS dBsm	Mu Difference in RCS	SSPdHH RCS dBsm	Mu Difference in RCS	SFpPdVV RCS dBsm	Mu Difference in RCS
-179.5	-5.600366	0.770661	0.281983	-0.13086	-4.996995	-0.0285735
-178.5	-6.330287		0.137087		-4.913905	
-177.5	-7.141688		0.020263		-4.939848	
-151.5	0.949127	-0.377305	-1.340032	-0.2924575	-7.910589	-1.058385
-150.5	0.426604		-1.064216		-6.796479	
-149.5	-0.194517		-0.755117		-5.793819	
-102.5	-1.483359	-0.0301165	-2.067547	0.444446	-7.642926	0.6875855
-101.5	-1.463619		-2.503372		-8.217873	
-100.5	-1.423126		-2.956439		-9.018097	
-69.5	-12.653506	1.556233	-3.267888	0.3442975	-5.705282	0.526325
-68.5	-14.146196		-3.529746		-6.129692	
-67.5	-15.765972		-3.956483		-6.757932	
-28.5	-2.705827	0.7854535	-5.254973	0.8831675	-1.869973	0.263611
-27.5	-3.484386		-6.130242		-2.103107	
-26.5	-4.276734		-7.021308		-2.397195	
0.5054	-3.844115	0.350277	-0.320232	0.266375	-1.548323	0.1652395
1.5054	-4.151567		-0.564831		-1.708577	
2.5054	-4.544669		-0.852982		-1.878802	
AVG RCS		0.5092005		0.25249475		0.09263375

Appendix E

Appendix E contains the sector statistics for the sphere, oriented pentagon down, with the flat plate mounted in the center, HH-pol. Analysis was conducted between 1-1.5 GHz, -180-180 degrees.

STATISTICS SUMMARY - SPdFpHH						
Sector x-axis y-axis	Minimum RCS (dB)	Maximum RCS (dB)	Arithmetic Mean (dB)	Geometric Mean (dB)	Median RCS (dB)	PCUM 95
1 1 - 1.5 179.5 - 174.5	-8.86244	-0.58678	-3.31149	-3.84885	-4.14092	-0.74411
2 1 - 1.5 177.5 - 172.5	-10.348	-0.73508	-3.76638	-4.36653	-4.41459	-0.985236
3 1 - 1.5 175.5 - 170.5	-12.579	-1.14721	-4.42894	-5.16676	-4.81136	-1.50043
4 1 - 1.5 173.5 - 168.5	-16.1584	-1.64649	-5.22823	-6.29742	-5.60946	-2.10675
5 1 - 1.5 171.5 - 166.5	-23.5975	-1.14543	-6.03153	-7.888	-6.83649	-2.10675
6 1 - 1.5 169.5 - 164.5	-38.8922	-0.774842	-6.69817	-10.1484	-8.39151	-1.53785
7 1 - 1.5 167.5 - 162.5	-38.8922	-0.534352	-7.1295	-11.8572	-9.7166	-1.16906
8 1 - 1.5 165.5 - 160.5	-38.8922	-0.49821	-7.3594	-12.7208	-10.7365	-0.878581
9 1 - 1.5 163.5 - 158.5	-30.8853	-0.49821	-7.52334	-12.485	-10.9537	-0.880974
10 1 - 1.5	-25.799	-0.49821	-7.67489	-12.1265	-10.9748	-1.16444

161.5 - 156.5					
11 1 - 1.5 159.5 - 154.5	-23.1225	-0.723757	-7.74191	-11.5018	-10.4654	-1.70268
12 1 - 1.5 157.5 - 152.5	-22.9884	-1.11669	-7.50965	-10.3428	-9.23388	-2.44133
13 1 - 1.5 155.5 - 150.5	-22.6405	-1.87823	-6.876	-8.84479	-7.68937	-2.88282
14 1 - 1.5 153.5 - 148.5	-19.5467	-1.16143	-5.96108	-7.38709	-6.89253	-2.07622
15 1 - 1.5 151.5 - 146.5	-14.3611	-0.161551	-5.02296	-6.33804	-6.94643	-0.982907
16 1 - 1.5 149.5 - 144.5	-17.6561	0.410267	-4.25969	-5.7412	-6.97837	-0.201409
17 1 - 1.5 147.5 - 142.5	-21.2307	0.732466	-3.76018	-5.5362	-7.0919	0.149882
18 1 - 1.5 145.5 - 140.5	-24.194	0.732466	-3.56376	-5.69175	-7.11762	0.410267
19 1 - 1.5 143.5 - 138.5	-24.2077	0.732466	-3.68718	-6.1882	-7.55819	0.46978
20 1 - 1.5 141.5 - 136.5	-24.2077	0.725617	-4.10954	-6.99206	-8.50212	0.23923
21 1 - 1.5 139.5 - 134.5	-25.0553	0.506405	-4.8005	-8.01784	-8.65408	-0.178137
22 1 - 1.5 137.5 - 132.5	-34.782	-0.0241119	-5.70004	-9.00521	-8.62211	-0.875498
23 1 - 1.5 135.5 - 130.5	-34.782	-0.875498	-6.69146	-9.64599	-8.64232	-1.79351
24 1 - 1.5	-34.782	-2.08985	-7.6332	-10.0161	-8.83172	-3.15159

133.5 - 128.5					
25 1 - 1.5 131.5 - 126.5	-27.9006	-3.43241	-8.33955	-10.3334	-8.85588	-4.5101
26 1 - 1.5 129.5 - 124.5	-32.1016	-4.93361	-8.79702	-10.8083	-8.84108	-5.59659
27 1 - 1.5 127.5 - 122.5	-37.896	-5.09424	-8.98826	-11.2117	-8.92828	-5.71095
28 1 - 1.5 125.5 - 120.5	-37.896	-4.84616	-8.91229	-11.2336	-9.30742	-5.36076
29 1 - 1.5 123.5 - 118.5	-37.896	-3.48662	-8.4999	-10.8907	-9.35717	-4.61915
30 1 - 1.5 121.5 - 116.5	-44.9561	-2.14576	-7.73926	-10.394	-9.17527	-3.24919
31 1 - 1.5 119.5 - 114.5	-44.9561	-1.04047	-6.73685	-9.93619	-8.623	-1.98385
32 1 - 1.5 117.5 - 112.5	-44.9561	-0.127509	-5.70079	-9.11685	-7.81591	-1.0072
33 1 - 1.5 115.5 - 110.5	-38.7317	0.46772	-4.79678	-7.9969	-7.56224	-0.129841
34 1 - 1.5 113.5 - 108.5	-28.8569	0.813131	-4.13173	-6.85438	-7.415	0.375786
35 1 - 1.5 111.5 - 106.5	-18.6411	0.903241	-3.74675	-6.26	-7.57566	0.672261
36 1 - 1.5 109.5 - 104.5	-15.3307	0.903241	-3.65685	-6.22439	-7.70843	0.732589
37 1 - 1.5 107.5 - 102.5	-17.9104	0.903241	-3.86211	-6.68787	-8.15248	0.672291
38 1 - 1.5	-23.3836	0.838805	-4.35155	-7.65103	-8.91448	0.440297

105.5 - 100.5					
39 1 - 1.5 103.5 - 98.5	-27.4183	0.52273	-5.09148	-9.00091	-9.51862	-0.0816034
40 1 - 1.5 101.5 - 96.5	-27.4183	-0.0816034	-6.03213	-10.1295	-10.2435	-0.820645
41 1 - 1.5 99.5 - 94.5	-27.4183	-0.925241	-7.06572	-10.6826	-10.7674	-1.75381
42 1 - 1.5 97.5 - 92.5	-25.8683	-1.9878	-8.01232	-10.6122	-10.4172	-2.97435
43 1 - 1.5 95.5 - 90.5	-25.8683	-3.37359	-8.66067	-10.3913	-9.85887	-4.48961
44 1 - 1.5 93.5 - 88.5	-25.1239	-4.76838	-8.98078	-10.2468	-9.4556	-5.3741
45 1 - 1.5 91.5 - 86.5	-22.3719	-4.72152	-9.12175	-10.1811	-9.39761	-5.41696
46 1 - 1.5 89.5 - 84.5	-20.0353	-4.72152	-9.25095	-10.1797	-9.67782	-5.34432
47 1 - 1.5 87.5 - 82.5	-17.6891	-4.72152	-9.35335	-10.1886	-9.94982	-5.74554
48 1 - 1.5 85.5 - 80.5	-20.3432	-4.91392	-9.24336	-10.162	-9.78586	-5.81851
49 1 - 1.5 83.5 - 78.5	-25.4997	-3.96298	-8.72136	-10.0843	-9.3637	-5.14725
50 1 - 1.5 81.5 - 76.5	-29.6833	-2.92595	-7.81733	-9.76558	-8.47224	-3.96298
51 1 - 1.5 79.5 - 74.5	-29.6833	-2.12329	-6.78668	-9.0398	-7.58518	-2.89421
52 1 - 1.5	-29.6833	-1.56896	-5.85383	-8.13176	-6.33623	-2.04795

77.5 - 72.5					
53 1 - 1.5 75.5 - 70.5	-30.3188	-1.05446	-5.17998	-7.4497	-5.5111	-1.44883
54 1 - 1.5 73.5 - 68.5	-30.3188	-0.679686	-4.77124	-7.24961	-5.49396	-1.11258
55 1 - 1.5 71.5 - 66.5	-30.3188	-0.617516	-4.65973	-7.39201	-5.96282	-0.945771
56 1 - 1.5 69.5 - 64.5	-28.4821	-0.617516	-4.76498	-7.75419	-6.96556	-0.885473
57 1 - 1.5 67.5 - 62.5	-29.0847	-0.617516	-5.08472	-8.43592	-8.00341	-0.935215
58 1 - 1.5 65.5 - 60.5	-35.2777	-0.642754	-5.51331	-9.12131	-8.83632	-1.24369
59 1 - 1.5 63.5 - 58.5	-35.2777	-0.96584	-6.00214	-9.38115	-8.61463	-1.66145
60 1 - 1.5 61.5 - 56.5	-35.2777	-1.55848	-6.44152	-9.1083	-7.63513	-2.36559
61 1 - 1.5 59.5 - 54.5	-33.4131	-2.42311	-6.7759	-8.65018	-6.97053	-3.30926
62 1 - 1.5 57.5 - 52.5	-24.9675	-3.00097	-7.00987	-8.47427	-7.09121	-3.82899
63 1 - 1.5 55.5 - 50.5	-27.253	-2.74465	-7.17173	-8.58614	-7.38219	-3.55517
64 1 - 1.5 53.5 - 48.5	-32.408	-2.71946	-7.3023	-8.86937	-7.68945	-3.16365
65 1 - 1.5 51.5 - 46.5	-32.408	-2.71946	-7.36205	-9.13061	-7.68945	-3.16365
66 1 - 1.5	-32.408	-2.71946	-7.26909	-9.28485	-7.42014	-3.49828

49.5 - 44.5					
67 1 - 1.5 47.5 - 42.5	-29.0466	-2.98853	-6.93129	-8.93868	-6.85874	-3.70807
68 1 - 1.5 45.5 - 40.5	-27.973	-2.29978	-6.38649	-8.09335	-6.43814	-3.27802
69 1 - 1.5 43.5 - 38.5	-27.236	-1.45367	-5.73497	-6.96266	-6.02665	-2.40883
70 1 - 1.5 41.5 - 36.5	-16.296	-0.867519	-5.12406	-6.06023	-5.79337	-1.74113
71 1 - 1.5 39.5 - 34.5	-16.296	-0.557922	-4.62968	-5.52963	-5.73213	-1.23069
72 1 - 1.5 37.5 - 32.5	-16.296	-0.473986	-4.33055	-5.25445	-5.54369	-0.867519
73 1 - 1.5 35.5 - 30.5	-16.1351	-0.473986	-4.2536	-5.16974	-5.6094	-0.720402
74 1 - 1.5 33.5 - 28.5	-14.5632	-0.473986	-4.35868	-5.21987	-5.6906	-0.865671
75 1 - 1.5 31.5 - 26.5	-12.0086	-0.572951	-4.62354	-5.44528	-5.6633	-1.23102
76 1 - 1.5 29.5 - 24.5	-12.7169	-0.813623	-4.9562	-5.88179	-5.36	-1.87287
77 1 - 1.5 27.5 - 22.5	-17.5445	-1.29742	-5.26617	-6.60092	-4.94639	-1.95879
78 1 - 1.5 25.5 - 20.5	-33.8005	-0.451787	-5.43242	-7.68861	-5.12254	-1.53211
79 1 - 1.5 23.5 - 18.5	-34.2635	0.0268593	-5.43089	-8.59407	-5.57524	-0.840043
80 1 - 1.5	-34.2635	0.21972	-5.36008	-8.88662	-5.80093	-0.379364

21.5 - 16.5						
81 1 - 1.5 19.5 - 14.5	-34.2635	0.275694	-5.30775	-8.60011	-6.19074	-0.167912
82 1 - 1.5 17.5 - 12.5	-21.5445	0.275694	-5.34672	-8.32662	-6.58556	-0.0374831
83 1 - 1.5 15.5 - 10.5	-33.777	0.275694	-5.44897	-8.43268	-6.61788	-0.263271
84 1 - 1.5 13.5 - 8.5	-33.777	0.11994	-5.4999	-8.29788	-6.51682	-0.591658
85 1 - 1.5 11.5 - 6.5	-33.777	-0.180766	-5.35187	-7.58056	-5.81123	-1.09713
86 1 - 1.5 9.5 - 4.5	-29.583	-0.591658	-4.94657	-6.37019	-5.11685	-1.56343
87 1 - 1.5 7.5 - 2.5	-16.5366	-1.10934	-4.38993	-5.18514	-4.37513	-1.82894
88 1 - 1.5 5.5 - 0.5	-11.8309	-1.32097	-3.84175	-4.34654	-3.88067	-1.67514
89 1 - 1.5 3.5 - -1.5	-9.17152	-1.1907	-3.43287	-3.8427	-3.50444	-1.42139
90 1 - 1.5 1.5 - -3.5	-9.10978	-1.06384	-3.23736	-3.66544	-3.39354	-1.29058
91 1 - 1.5 -0.5 - -5.5	-11.647	-1.06384	-3.28093	-3.80619	-3.41728	-1.26506
92 1 - 1.5 -2.5 - -7.5	-15.3166	-1.06384	-3.5424	-4.23597	-3.4656	-1.32146
93 1 - 1.5 -4.5 - -9.5	-18.9059	-1.13859	-3.98412	-4.89037	-3.83859	-1.64725
94 1 - 1.5	-19.3889	-1.50523	-4.54835	-5.60296	-4.44846	-2.18008

-6.5 - -11.5						
95 1 - 1.5 -8.5 - -13.5	-19.3889	-1.98399	-5.19477	-6.26831	-5.19857	-2.45874
96 1 - 1.5 -10.5 - -15.5	-19.3889	-1.87212	-5.81354	-6.83487	-6.05558	-2.34678
97 1 - 1.5 -12.5 - -17.5	-17.7645	-1.87212	-6.34126	-7.41723	-7.48786	-2.16044
98 1 - 1.5 -14.5 - -19.5	-16.0607	-1.87212	-6.72022	-8.04907	-8.44116	-2.13184
99 1 - 1.5 -16.5 - -21.5	-19.4193	-1.88593	-6.99338	-8.73799	-9.41283	-2.15128
100 1 - 1.5 -18.5 - -23.5	-24.1955	-1.99666	-7.15987	-9.46655	-9.62958	-2.24517
101 1 - 1.5 -20.5 - -25.5	-34.4658	-1.91978	-7.16714	-10.2881	-9.58209	-2.22341
102 1 - 1.5 -22.5 - -27.5	-43.4111	-1.86737	-6.97746	-10.9027	-8.85932	-2.13705
103 1 - 1.5 -24.5 - -29.5	-43.4111	-1.84735	-6.56032	-10.4254	-7.5105	-2.1047
104 1 - 1.5 -26.5 - -31.5	-43.4111	-1.84735	-6.01697	-9.16711	-6.31123	-2.16065
105 1 - 1.5 -28.5 - -33.5	-26.5888	-1.84735	-5.45872	-7.62473	-5.12032	-2.25418
106 1 - 1.5 -30.5 - -35.5	-22.7626	-1.40247	-4.99168	-6.78983	-4.94225	-1.87043
107 1 - 1.5 -32.5 - -37.5	-21.6255	-1.10213	-4.68498	-6.42553	-4.99545	-1.41105
108 1 - 1.5	-21.9968	-1.01114	-4.56592	-6.43622	-5.21926	-1.2583

-34.5 - -39.5					
109 1 - 1.5 -36.5 - -41.5	-23.9213	-1.01114	-4.63643	-6.74315	-5.59144	-1.24282
110 1 - 1.5 -38.5 - -43.5	-25.0594	-1.01114	-4.87979	-7.22706	-6.15813	-1.3153
111 1 - 1.5 -40.5 - -45.5	-25.2943	-1.1481	-5.29265	-7.76784	-6.3173	-1.59212
112 1 - 1.5 -42.5 - -47.5	-25.2943	-1.49483	-5.8433	-8.27343	-6.46348	-2.14159
113 1 - 1.5 -44.5 - -49.5	-25.2943	-2.14159	-6.50478	-8.75174	-7.14108	-2.97688
114 1 - 1.5 -46.5 - -51.5	-23.5214	-2.9344	-7.19359	-9.23092	-8.16039	-3.38357
115 1 - 1.5 -48.5 - -53.5	-20.3207	-2.96508	-7.83279	-9.73209	-8.86381	-3.43331
116 1 - 1.5 -50.5 - -55.5	-20.717	-2.96508	-8.34028	-10.2226	-9.76419	-3.43331
117 1 - 1.5 -52.5 - -57.5	-25.5701	-2.96508	-8.68774	-10.6403	-10.2902	-3.52291
118 1 - 1.5 -54.5 - -59.5	-30.4809	-3.04872	-8.89949	-10.9184	-10.2851	-3.82639
119 1 - 1.5 -56.5 - -61.5	-30.6863	-3.24523	-8.96926	-10.9989	-10.0969	-4.26683
120 1 - 1.5 -58.5 - -63.5	-30.6863	-3.6054	-8.85504	-10.9234	-9.84355	-4.84068
121 1 - 1.5 -60.5 - -65.5	-30.6863	-3.65781	-8.45298	-10.7448	-9.17899	-4.69984
122 1 - 1.5	-26.137	-2.68825	-7.78233	-10.4752	-8.62446	-3.76325

-62.5 - -67.5					
123 1 - 1.5 -64.5 - -69.5	-27.647	-1.90581	-6.95738	-9.93294	-7.80706	-2.97734
124 1 - 1.5 -66.5 - -71.5	-27.647	-1.40606	-6.16017	-8.98299	-7.10342	-2.31087
125 1 - 1.5 -68.5 - -73.5	-27.647	-1.08977	-5.53735	-7.92025	-6.62497	-1.86972
126 1 - 1.5 -70.5 - -75.5	-22.1684	-1.08977	-5.17929	-7.16222	-6.07722	-1.49705
127 1 - 1.5 -72.5 - -77.5	-20.8334	-1.08977	-5.13217	-7.08653	-5.85248	-1.43974
128 1 - 1.5 -74.5 - -79.5	-43.6186	-1.08995	-5.40465	-7.84771	-5.9773	-1.59837
129 1 - 1.5 -76.5 - -81.5	-43.6186	-1.17105	-5.97259	-8.91397	-6.48801	-2.04084
130 1 - 1.5 -78.5 - -83.5	-43.6186	-1.57741	-6.7486	-9.68891	-7.05863	-2.67095
131 1 - 1.5 -80.5 - -85.5	-33.877	-2.2501	-7.55366	-9.84619	-7.95123	-3.43568
132 1 - 1.5 -82.5 - -87.5	-25.2832	-3.10043	-8.18699	-9.74809	-8.43393	-4.33319
133 1 - 1.5 -84.5 - -89.5	-20.0845	-4.16579	-8.55373	-9.7747	-8.79085	-5.47006
134 1 - 1.5 -86.5 - -91.5	-19.0297	-5.33637	-8.73861	-9.86412	-8.78374	-5.69535
135 1 - 1.5 -88.5 - -93.5	-19.0297	-5.38394	-8.87622	-9.97346	-8.81002	-5.93494
136 1 - 1.5	-19.2798	-5.38394	-9.01182	-10.1017	-9.08937	-6.20676

-90.5 - -95.5					
137 1 - 1.5 -92.5 - -97.5	-23.5683	-5.0278	-9.02721	-10.3002	-9.35817	-5.75805
138 1 - 1.5 -94.5 - -99.5	-39.9328	-3.74416	-8.69896	-10.6868	-9.57015	-4.61007
139 1 - 1.5 -96.5 - -101.5	-39.9328	-2.63547	-7.9817	-10.7221	-9.24496	-3.55745
140 1 - 1.5 -98.5 - -103.5	-39.9328	-1.72446	-7.03337	-10.0836	-8.64244	-2.58933
141 1 - 1.5 -100.5 - -105.5	-39.3955	-1.17199	-6.12219	-8.88143	-8.24534	-1.83274
142 1 - 1.5 -102.5 - -107.5	-39.3955	-0.853854	-5.39103	-7.68176	-7.71457	-1.36633
143 1 - 1.5 -104.5 - -109.5	-39.3955	-0.725374	-4.91331	-6.94759	-7.35285	-1.07232
144 1 - 1.5 -106.5 - -111.5	-23.059	-0.725374	-4.69938	-6.59069	-7.5377	-0.976769
145 1 - 1.5 -108.5 - -113.5	-18.5838	-0.725374	-4.74494	-6.71354	-7.82934	-1.02538
146 1 - 1.5 -110.5 - -115.5	-20.5834	-0.778206	-5.03921	-7.29112	-7.95373	-1.08357
147 1 - 1.5 -112.5 - -117.5	-36.7421	-1.03579	-5.54104	-8.43307	-8.14508	-1.3108
148 1 - 1.5 -114.5 - -119.5	-36.7421	-1.3178	-6.17481	-9.87288	-8.30316	-1.81031
149 1 - 1.5 -116.5 - -121.5	-36.7421	-1.81031	-6.81094	-10.9663	-8.30316	-2.45277
150 1 - 1.5	-37.4813	-2.45277	-7.30877	-11.1739	-8.19503	-3.28095

-118.5 - -123.5					
151 1 - 1.5 -120.5 - -125.5	-37.4813	-3.29141	-7.59942	-10.6038	-8.03925	-3.98528
152 1 - 1.5 -122.5 - -127.5	-37.4813	-3.87772	-7.73093	-9.94419	-8.08152	-4.30972
153 1 - 1.5 -124.5 - -129.5	-25.7511	-3.84559	-7.77038	-9.61092	-8.20359	-4.23113
154 1 - 1.5 -126.5 - -131.5	-25.3039	-3.84559	-7.81925	-9.86131	-8.2179	-4.23113
155 1 - 1.5 -128.5 - -133.5	-37.1971	-3.84559	-7.79682	-10.4725	-8.2179	-4.1912
156 1 - 1.5 -130.5 - -135.5	-37.1971	-3.27552	-7.5924	-10.6031	-8.2179	-3.83754
157 1 - 1.5 -132.5 - -137.5	-37.1971	-2.53039	-7.06614	-9.8279	-8.08662	-2.99924
158 1 - 1.5 -134.5 - -139.5	-22.2683	-1.84368	-6.28687	-8.28725	-7.32696	-2.29434
159 1 - 1.5 -136.5 - -141.5	-16.0589	-1.28565	-5.40821	-6.80206	-6.12699	-1.70108
160 1 - 1.5 -138.5 - -143.5	-13.6813	-0.975128	-4.63113	-5.6993	-5.05647	-1.3218
161 1 - 1.5 -140.5 - -145.5	-12.9612	-0.911644	-4.06745	-4.96039	-4.38057	-1.0862
162 1 - 1.5 -142.5 - -147.5	-12.3926	-0.911644	-3.76561	-4.55938	-3.85707	-1.06492
163 1 - 1.5 -144.5 - -149.5	-11.4286	-0.911644	-3.74115	-4.49166	-3.63459	-1.07263
164 1 - 1.5	-10.6731	-0.932277	-3.94595	-4.73963	-3.74998	-1.21808

-146.5 - -151.5					
165 1 - 1.5 -148.5 - -153.5	-15.612	-1.27503	-4.35965	-5.3654	-4.03958	-1.62073
166 1 - 1.5 -150.5 - -155.5	-29.6812	-1.60606	-4.85423	-6.4243	-4.56125	-1.98916
167 1 - 1.5 -152.5 - -157.5	-29.7894	-1.26516	-5.35292	-7.61656	-5.2445	-1.93592
168 1 - 1.5 -154.5 - -159.5	-29.7894	-0.888379	-5.69815	-8.30779	-6.08999	-1.60606
169 1 - 1.5 -156.5 - -161.5	-29.7894	-0.677853	-5.87973	-8.39725	-6.73238	-1.26516
170 1 - 1.5 -158.5 - -163.5	-22.9601	-0.418218	-5.88432	-8.12224	-7.11125	-0.944629
171 1 - 1.5 -160.5 - -165.5	-25.1511	-0.353116	-5.84325	-8.04852	-7.21577	-0.710333
172 1 - 1.5 -162.5 - -167.5	-38.7519	-0.353116	-5.75558	-8.12746	-7.14773	-0.670335
173 1 - 1.5 -164.5 - -169.5	-38.7519	-0.353116	-5.59833	-8.05329	-6.72265	-0.710333
174 1 - 1.5 -166.5 - -171.5	-38.7519	-0.411695	-5.31185	-7.52924	-6.03816	-0.89517
175 1 - 1.5 -168.5 - -173.5	-30.8759	-0.526916	-4.87252	-6.53229	-5.22703	-1.22057
176 1 - 1.5 -170.5 - -175.5	-19.219	-0.799232	-4.38192	-5.46084	-4.55978	-1.56686
177 1 - 1.5 -172.5 - -177.5	-13.135	-0.963628	-3.87141	-4.59227	-4.1605	-1.27958
178 1 - 1.5	-10.1214	-0.639353	-3.4566	-4.01045	-4.10139	-0.963628

-174.5 - -179.5						
Composite Statistics	-44.9561	0.903241	-5.80771	-8.23972		

Bibliography

[1]   M. Kanda, "Standard Probes for Electromagnetic Field Measurements," *IEEE Transactions on Antennas and Propagation,* vol. 41, no. 10, pp. 1349-1364, 1993.

[2]   W. A. Holm, M. A. Richards and J. A. Scheer, Principles of Modern Radar: Basic Principles, Raleigh, NC: SciTech Publishing, 2010.

[3]   E. F. Knott, J. F. Shaeffer and M. T. Tuley, Radar Cross Section, 2nd ed., Raleigh, NC: SciTech Publishing, 2004.

[4]   B. York, "Electromagnetic Fields and Waves," [Online]. Available: http://my.ece.ucsb.edu/Plane_Waves.pdf. [Accessed 2 February 2015].

[5]   J. Johansson and U. Lundgren, "Introduction to Electromagnetics," [Online]. Available: http://www.dannex.se/theory/1.html. [Accessed 5 February 2015].

[6]   J. Malherbe, D. A. McNamara and C. W. Pistorius, Introduction to The Uniform Geometrical Theory of Diffraction, Norwood, MA: Artec House, 1990.

[7]   "Domearama," [Online]. Available: http://www.domerama.com/fabricating/making-geodesic-models/make-a-geodesic-model-dome-from-straws/. [Accessed 10 February 2015].

[8]   "Dome Basics," [Online]. Available: http://homepages.ihug.co.nz/~jw.rich/about.htm. [Accessed 8 February 2015].

[9]   J. Clinton and J. Salsburg, "Geodesic Math," [Online]. Available: http://www.salsburg.com/geod/geodesicmath.pdf. [Accessed 10 February 2015].

[10] "Math Is Fun: Euler's Formula," [Online]. Available: http://www.mathsisfun.com/geometry/eulers- formula.html. Accessed 10 Feb 15.

[Accessed 10 February 2015].

[11] "GPS Basics," [Online]. Available: http://www.gps-basics.com/faq/q0116.shtml. [Accessed 10 February 2015].

[12] J. R. Clynch, "GPS Accuracy Levels: Major Accuracy Divisions," Naval post Graduate School, [Online]. Available: http://www.oc.nps.edu/oc2902w/gps/gpsacc.html. [Accessed 2 February 2015].

[13] "DJI Phantom II Specs Page," [Online]. Available: http://www.dji.com/product/phantom-2/spec. [Accessed 10 February 2015].

[14] S. Goodman, "AFIT Sphere Characterization," Advanced Compact Range AFRL/RYS, Wright Patterson AFB, 2014.

[15] B. Welsh, "RCS Measurement Uncertainty Analysis," Boulder, 2007.

[16] S. Bell, "A Beginner's Guide to Uncertainty of Measurement," Crown, Teddington, 1999.

[17] S. Holmes, "RMS Error," 28 November 2000. [Online]. Available: http://statweb.stanford.edu/~susan/courses/s60/split/node60.html. [Accessed 23 February 2015].

[18] H. W. Coleman and G. W. J. Steele, Experimentation and Uncertainty Analysis For Engineers, Toronto: John Wiley & Sons Inc, 1989.